RE-PARAMETERIZATION OF A QUASI ANALYTICAL ALGORITHM AND PHYCOCYANIN ESTIMATION IN A TROPICAL RESERVOIR

Igor Ogashawara

Master Thesis at Post Graduation Course in Remote Sensing, guided by Drs. José Luiz Stech, and José Galizia Tundisi, approved in March 10, 2014.

URL of the original document:
<http://urlib.net/8JMKD3MGP5W34M/3FNS6NE>

INPE

São José dos Campos

2014

sid.inpe.br/mtc-m21b/2014/02.13.12.56-TDI

RE-PARAMETERIZATION OF A QUASI ANALYTICAL ALGORITHM AND PHYCOCYANIN ESTIMATION IN A TROPICAL RESERVOIR

Igor Ogashawara

Master Thesis at Post Graduation Course in Remote Sensing, guided by Drs. José Luiz Stech, and José Galizia Tundisi, approved in March 10, 2014.

URL of the original document:
<http://urlib.net/8JMKD3MGP5W34M/3FNS6NE>

Aprovado (a) pela Banca Examinadora em cumprimento ao requisito exigido para obtenção do Título de **Mestre** em

Sensoriamento Remoto

Dr.   **Milton Kampel**
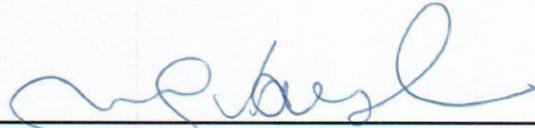
Presidente / INPE / SJCampos - SP

Dr.   **José Luiz Stech**

Orientador(a) / INPE / SJCampos - SP

Dr.   **José Galizia Tundisi**

Orientador(a) / Inst Int de Ecologia / São Carlos - SP

Dr.   **Deepak Ranjan Mishra**
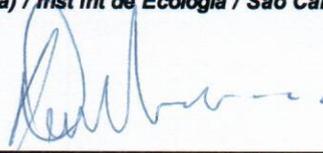
Convidado(a) / Univ. of Georgia / Estados Unidos - USA

Este trabalho foi aprovado por:

( ) maioria simples

( ) unanimidade

Aluno (a): *Igor Ogashawara*

São José dos Campos, 10 de Março de 2014

"Dicebat Bernardus Carnotensis nos esse quasi nanos, gigantium humeris insidentes, ut possimus plura eis et remotiora videre, non utique proprii visus acumine, aut eminentia corporis, sed quia in altum subvenimur et extollimur magnitudine gigantea".

<p align="right">*John Salisbury*</p>

To my parents, who supported me at all steps of my education.

To my grandfather, for always reminding me to pursue the Middle Path and to never let pride take the best of me.

ACKNOWLEDGEMENTS

ABSTRACT

The eutrophication of aquatic systems is a worldwide environmental problem. One of its main outcome is the algal bloom, including the potentially toxic algal which can affect human health. Because of the toxicity of the harmful algal blooms, environmental monitoring is needed, mainly in aquatic systems near to urban centers. The use of remote sensing for monitoring the algal blooms uses bio-optical modeling, which is based on the spectral behavior of the optically active components in the water to estimate their concentrations as well as their inherent optical properties (IOPs). The detection of cyanobacteria, one of the main phylum of harmful algal, occurs by the identification of a unique pigment in inland waters cyanobacteria, the phycocyanin (PC). Remote sensing techniques, such as the quasi-analytical algorithms (QAA) - a type of bio-optical model - have been used to the estimation of IOPs in aquatic systems using in situ hyperspectral data and satellite multispectral data. However there is not any QAA developed or evaluated in tropical inland waters. Therefore the goal of this research was to evaluate the need for the re-parameterization of a QAA and to re-parameterize one for tropical eutrophic inland waters. Radiometric, limnological and IOPs data were collected in the Funil Hydroeletric Reservoir, located between São Paulo and Rio de Janeiro States, Brazil. Results of the Normalized Root Mean Square Error (NRMSE) showed that for the application of QAA in tropical inland waters a re-parameterization is needed. Thus, the results of the re-parameterization showed an average NRMSE of 36% for the retrieval of the total absorption coefficients. The colored detrital matter (CDM) absorption coefficients were retrieved with an average NRMSE of 49%. Phytoplankton absorption coefficients were retrieved with an average NRMSE of 74%. PC concentration estimation from the estimated IOPs showed good results (NRMSE of 24.94%) for the in situ hyperspectral dataset. Uncertainties in the estimations are mainly due to the lack of in situ data of PC absorption coefficients to calibrate the model. The re-parameterization was also applied for a synthetic dataset of the future Ocean & Land Color Imager (OLCI) sensor which will be part of Sentinel 3 satellite. The simulation of OLCI data was conducted using its spectral response function and it is enhanced because of its potentially use of environmental monitoring since its temporal resolution will be improved by the launch of 2 satellites working as a constellation. Overall results were encouraging since it is one of the first works to explore the estimation of IOPs in tropical inland waters through remote sensing. However, results also indicated the need for further fine tuning of the model, mainly in the estimation of total absorption coefficients. Therefore, the development of a QAA and the estimation of PC concentration in tropical inland waters are an important step for the development of a robust tool for improving water quality monitoring.

RE-PARAMETRIZAÇÃO DE UM ALGORITMO QUASI ANALÍTICO E ESTIMAÇÃO DE FICOCIANINA PARA UM RESERVATÓRIO TROPICAL

RESUMO

A eutrofização de sistemas aquáticos é um problema recorrente em diversas parte do mundo. Uma de suas principais consequências é o florescimento de algas, e entre elas, as algas potencialmente tóxicas que podem ser prejudiciais para a saúde humana. Devido a essa toxicidade, é necessário um monitoramento constante dessas florações em ambientes aquáticos, principalmente próximos aos centros urbanos. A utilização de sensoriamento remoto para o monitoramento de florescimento de algas ocorre por meio da modelagem bio-óptica, que utiliza a resposta espectral dos componentes opticamente ativos na água para estimar a sua concentração assim como as propriedades ópticas inerentes (POIs). A identificação de cianobactéria, um das principais classes de algas tóxicas, é então realizada por meio de um pigmento único em cianobactérias de águas interiores que é a ficocianina (PC). Técnicas de sensoriamento remoto, como os algoritmos quasi-analíticos (QAAs), um tipo de modelo bio-óptico, tem sido utilizados para a obtenção das POIs em sistemas aquáticos por meio de dados hiperespectrais coletados in situ e dados multiespectrais provenientes de satélites. Entretanto, nenhum QAA foi desenvolvido ou avaliado para águas interiores tropicais. Portanto o objetivo do presente estudo foi avaliar a necessidade de reparametrizar um QAA e realizar a reparametrização do mesmo para águas interiores eutrofizadas em uma região tropical. Dados radiométricos, limnológicos e POIs foram coletados no Reservatório Hidrelétrico de Funil, localizado entre os estados de São Paulo e Rio de Janeiro. Resultados mostram que para a aplicação de QAA em águas interiores tropicais é necessária uma reparametrização, que foi avaliada por meio da Raiz do Erro Médio Quadrático Normalizada (NRMSE). Dessa forma resultados da reparametrização mostram um NRMSE de 36% para a média dos coeficientes de absorção total. Os coeficientes de absorção da matéria residual colorida (CDM) foram estimados com a média do NRMSE de 49% já os coeficientes de absorção do fitoplâncton foram estimados com a média do NRMSE de 74%. A estimação da concentração de PC por meio das POIs estimadas mostram bons resultados (NRMSE de 24.94%) para o conjunto de dados hiperespectrais in situ. Incertezas das estimações ocorreram principalmente pela falta de dados empíricos dos coeficientes de absorção de PC para a calibração do modelo. A reparametrização também foi aplicada para um conjunto sintético de dados do futuro sensor Ocean & Land Color Imager (OLCI) que fará parte do satélite Sentinel 3. A simulação dos dados do sensor OLCI foi realizada por sua função de resposta espectral e se destaca pela sua possível utilização para o monitorando ambiental devido a sua resolução temporal que será ampliada pelo lançamento de 2 satélites atuando em formato de constelação. Os resultados das etapas do trabalho foram estimulantes por ser um dos primeiros trabalhos a explorar a estimação de IOPs em águas

interiores tropicais por meio de sensoriamento remoto. Entretanto os resultados também indicam a necessidade de um aprimoramento, principalmente na estimação do coeficiente de absorção total, que é essencial para a estimação dos demais coeficientes de absorção. Portanto, o desenvolvimento de um QAA e a estimação da concentração de PC em águas interiores tropicais são um importante passo para o desenvolvimento de uma ferramenta robusta para o monitoramento da qualidade da água.

LIST OF FIGURES

LIST OF TABLES

xx

LIST OF ACRONYMS AND ABBREVIATIONS

a	Absorption coefficient
ADEOS	Advanced Earth Observing Satellite
AISA Eagle	Airborne Imaging Spectrometer for Applications Eagle
AOPs	Apparent Optical Properties
ARIES	Australian Resource Information and Environmental Satellite
ASD	Analytical Spectral Devices
b	Scattering coefficient
CASI-2	Compact Airborne Spectrographic Imager-2
CDM	Colored Detrital Matter
CDOM	Colored Dissolved Organic Matter
CEBIMar	*Centro de Biologia Marinha da Universidade de São Paulo*
CHABs	Cyanobacterial Harmful Algal Blooms
Chl-*a*	Chlorophyll-a
CHRIS	Compact High Resolution Imaging Spectrometer
CI	Cyanobacteria Index
CZCS	Coastal Zone Color Scanner
ELISA	Enzyme-Linked ImmunoSorbent Assay
EnMAP	Environmental Mapping and Analysis Program
ERTS-1	Earth Resources Technology Satellite
ESA	European Space Agency
ESALQ	*Escola Superior de Agricultura "Luiz de Queiroz"*
ETM+	Enhanced Thematic Mapper Plus
FOV	Field Of View
GA-PLS	Genetic Algorithm and Partial Least Squares
HABs	Harmful Algal Blooms
HICO	Hyperspectral Imager for the Coastal Ocean
HyspIRI	Hyperspectral Infra-red Imager
IIE	International Institute of Ecology

INEA	*Instituto Estadual do Ambiente do Estado do Rio de Janeiro*
IOPs	Inherent Optical Properties
LED	Light-Emitting Diode
MAE	Mean Absolute Error
MERIS	Medium Resolution Imaging Spectrometer
MODIS	Moderate Resolution Imaging Spectroradiometer
MSE	Mean Square Error
NaClO	Sodium Hypochlorite
NAP	Non-Algal Particles
NASA	National Aeronautics and Space Administration
NDPCI	Normalized Difference Phycocyanin Index
NH_3	Ammonia
NH_4^+	Ammonium cation
NIR	Near Infrared
NRMSE	Normalized Root Mean Square Error
OACs	Optically Active Components
OBM	Optimal Band ratio Modeling
OCM	Ocean Color Monitor
OLCI	Ocean & Land Color Imager
PC	Phycocyanin
pQAA	Proposed Quasi-Analytical Algorithm
PRISMA	PRecursore IperSpettrale della Missione Applicativa
QAA	Quasi-Analytical Algorithm
R	Irradiance Reflectance Ratio
RMSE	Root Mean Square Error
R_{rs}	Remote Sensing Reflectance from above surface
r_{rs}	Remote Sensing Reflectance from subsurface
SeaWIFS	Sea-viewing Wide Field-of-view Sensor
SLSTR	Sea and Land Surface Temperature Radiometer
SWIR	Short Wave Infrared
TM	Thematic Mapper

TSS	Total Suspension Solids
USP	*Universidade de São Paulo*
UV	Ultra-Violet
UV-A	Ultra-Violet A
VNIR	Visible and Near Infrared

INDEX

1 INTRODUCTION

The eutrophication process in aquatic systems is becoming a significant water quality problem, affecting inland water bodies all over the world (UNEP, 1999). It has been a concern for environmental and public health managers since one of its main consequences is the onset of harmful algal blooms (HABs) (SIVONEN; JONES, 1999). One of the most common phylum of HABs is the cyanophyta, which has some species of cyanobacteria (also known as blue-green algae) capable of producing toxins. These species have been occurring in aquatic systems worldwide during the past decade (FALCONER; HUMPAGE, 2006). Thus, there is an increasing need for water governance systems, mainly in places with lack of potable water and environmental management. Seven key challenges to practice a good management were described by the National Research Council (NRC) in their document "*The Drama of the Commons*" (NRC, 2002). The first one is the monitoring of resources, and the second, a low cost enforcement of rules. To face these challenges, Ostrom et al. (2003) believes the use of current research in collaboration with management strategies could solve particular challenges.

The monitoring of Cyanobacterial Harmful Algal Bloom (CHAB) is an important task for aquatic systems, mainly in water bodies used for water supply. Its importance is justified because cyanobacteria have been considered the largest and most diverse group of prokaryotes with very fast growth rates, especially in warm summer, when temperature, light and nutrients from agriculture fertilizers and other sources increase (MISHRA et al., 2009). They usually dominate the phytoplankton in inland and coastal areas because of their capacity of buoyancy regulation, elementary nitrogen fixing capability, and efficient use of yellow-orange light for photosynthesis (REYNOLDS, 2006). All these capabilities make cyanobacteria one of the main phylum present in inland eutrophic waters. Furthermore, aquatic environments with CHABs develop thick surface scums, and they also have a distinct taste and odor (CODD et al., 1999; RANDOLPH et al., 2008; MISHRA et al., 2009). However, the main problem of CHABs are their

capacity to produce toxins also known as "cyanotoxins", which are a major concern for human health. Some species of cyanobacteria produce toxins which cause hepatotoxic, neurotoxic and dermatotoxic effects and general inhibition of protein synthesis in animals and humans (SIVONEN; JONES, 1999).

The first scientific report of animals' contaminations by cyanotoxins occurred in 1878, in an Australian lake which had an unusual warmth causing a "thick scum like green oil" on its surface. As cattle drank water from the lake, the animals were rapidly poisoned, provoking their death (FRANCIS, G., 1878). The author even observed the time that cyanotoxins took to cause death in different animals: in sheep, from six to eight hours; in horses, from eight to twenty-four hours; in dogs, from four to five hours, and in pigs, from three to four hours. One of the first reported cases of human casualty associated with cyanobacteria and their toxins came about in 1996, in the city of Caruaru, PE, Brazil, where exposure through kidney dialysis led to the death of approximately fifty patients (AZEVEDO et al., 2002). This disaster raised the awareness of water quality managers, environmental agencies, policy makers and the general public to the problem of CHABs which also increases the cost of water treatment. Thus reliable and constant monitoring of CHABs is essential for environmental and public health.

Traditional CHAB's monitoring methods consist of collection of field samples, laboratory analysis, and manual cell counts. These methods are time-consuming, labor intensive, and costly (LE et al., 2011). Additionally, spatial and temporal heterogeneity of water bodies often result in inadequate monitoring and characterization of CHABs, since they must rely on sampling methods and interpolation and extrapolation between sample points (KHORRAM et al., 1991). Another problem of the traditional methods of monitoring CHABs is related to their regulation of buoyancy which allow them to move in the water column. This characteristic affects the collection of water since a floating ship could disturb the natural spatial distribution of a bloom (KUTSER, 2004). Besides, planning field trips to monitor CHABs is extremely difficult, because

algal blooms may be ephemeral and vary according to weather conditions, capable of changing the dynamics of the water column in few days through mixing and stratification processes (TUNDISI et al., 2004; 2010; OGASHAWARA et al., 2014).

Efficient alternative methods should be developed to improve the monitoring of CHABs, combining spatial and temporal approaches with low cost analysis. These characteristics enhance remote sensing as a valuable tool for a potentially effective solution to monitoring inland water quality. This idea is supported by Kutser (2004), who emphasized that the use of remote sensing to provide information about the extent of CHABs is more reliable if compared to traditional monitoring methods, because it does not break (or interfere with) the CHABs to collect data. Metsamaa et al. (2006) also highlighted the use of remote sensing by describing it as the only technique to map the spatial distribution of CHABs. The authors also stressed that remote sensing is an alternative to estimate the amount of cyanobacteria just below the surface, however it could not be used to estimate it in the water column.

Remote sensing of aquatic environments can be classified as either Case 1 or Case 2 waters (MOREL; PRIEUR, 1977). This classification was previously based on the ratio of chlorophyll-*a* (chl-*a*) concentration (in mg m^{-3}) to the scattering coefficient at 550 nm (in m^{-1}). The ratio for Case 1 waters should be greater than 1, and in Case 2, should be less than 1. Nevertheless, Gordon and Morel (1983) proposed new definitions for Case 1 and Case 2. They classify as Case 1 waters whose optical properties are determined mainly by phytoplankton and the other derivative compounds, such as colored dissolved organic matter (CDOM) and detritus were related to phytoplankton. They as so classified Case 2 waters as waters whose optical properties are significantly influenced by other constituents, such as mineral particles and CDOM, and their concentrations do not covary with the phytoplankton concentration. This classification – in only two different water types – showed several problems (MOBLEY et al., 2004) such as the misinterpretation that inland waters belong

3

to Case 2, when it is possible that a continental aquatic system can be dominated only by the phytoplankton (Case 1). However this classification is still used since their definitions give a synoptic view of the study site.

The use of remote sensing for water quality monitoring in Case 2 waters has been far less successful if compared to Case 1 waters. This fact is explainable by the complex interactions of the four main optically active components (OACs) present in Case 2 waters (or complex waters): phytoplankton, non-algal particles, CDOM and pure water. These complex interactions were intensified by anthropogenic actions, which introduced external inputs to the aquatic system. This complexity of mixed componets, associated to an inadequate atmospheric correction, will increase the uncertainties of the use of orbital remote sensing to monitor water quality. Another source of uncertainty are sensor's spatial and temporal resolution which are essential to the better estimation on water quality parameters in inland waters. Kutser (2004) showed that, although hyperspectral orbital sensors could be used to map CHABs, they would not be useful for monitoring water quality because of their temporal resolution which is inadequate for the speed of environmental responses. In spite of the lack of orbital optical sensors for aquatic studies, remote sensing techniques are potential tools for monitoring water quality. Bukata (2005) described that, with the increase of governmental sponsoring of satellites for monitoring Earth's ecosystems, remote sensing could easily be made available as a technology for monitoring water quality.

Thus, for the identification of CHABs with remote sensing techniques, scientists initially tried to estimate their biomass mostly from chl-*a* concentration, since it is the primary and dominant photosynthetic pigment in cyanobacteria (REINART; KUTSER, 2006). However, recent studies have documented that chl-*a* is not an accurate estimator of cyanobacterial biomass, since it is common phytoplankton groups (HUNTER et al., 2009). Therefore, recent studies try to analyze the spectral characteristics of phycocyanin (PC), a characteristic accessory pigment of inland cyanobacteria species (REYNOLDS, 2006).

Therefore, PC has been used as a proxy, because of its two distinct spectral characteristics: the absorption peak around 620 nm and the fluorescence around 650 nm (DEKKER, 1993; SIMIS et al, 2005; RUIZ-VERDU, et al., 2008). Thus, the development of bio-optical algorithms that include PC absorption peak spectral bands have been used to estimate PC concentrations (VINCENT et al., 2004) or PC's Inherent Optical Properties (IOPs) (MISHRA et al., 2013).

1.1. Hypothesis

To enhance the knowledge on bio-optical modeling in tropical aquatic systems, the following hypothesis was elaborated:

- Is it possible and needed to re-parameterize a quasi-analytical algorithm (QAA) to estimate the absorption coefficient of phycocyanin at 620 nm in a tropical region?

1.2. Objectives

The main objective of this work is the re-parameterization of a QAA for the quantification of the coefficient of absorption of PC in order to estimate its concentration.

To achieve the main goal, other specific objectives were:

1. To analyze the uncertainties and errors from the estimated IOPs and PC concentration from the re-parameterized algorithm;

2. To simulate the algorithm using the spectral bands from the European Space Agency future sensor Ocean & Land Color Imager (OLCI);

2 BACKGROUND

2.1. Remote Sensing of Aquatic Environments

Earth Observations from space began in August, 1972, with the launch by National Aeronautics and Space Administration (NASA) of the Earth Resources Technology Satellite (ERTS-1) (JENSEN, 2007). The use of this technology to monitor aquatic environments was initiated by oceanographers, who were aware that chl-*a* and temperature could be monitored remotely (BUKATA, 2013). However, for inland waters, limnologists only in the last two decades started to extensively use remote sensing techniques to monitor water quality parameters.

This monitoring occurs through the use of optical remote sensing which enables spatiotemporally comprehensive assessment of optical properties of the aquatic system. Absorption, scattering and attenuation properties of a water body are thereby retrieved from proximal, aerial or orbital measurements datasets of the visible domain of the solar reflective spectrum. Such optical properties allow the estimation of primary production, turbidity, eutrophication, particulate and dissolved carbon contents, or the assessment of currents and algal blooms (PLATT et al., 2008).

Oceanographers developed the theory, field procedures and equipment for marine optics. All these achievements are the base for the modeling of downwelling spectral solar and sky radiation with the air-water interface and the subsurface aquatic absorption and scattering centers. Studies from Cox and Munk (1954), Petzold (1972), Jerlov (1968, 1976), Preisendorfer (1976), among numerous others, established the main theory of marine optics before or around the launch of ERTS-1.

Among these works on marine optics, an important work made by Gordon et al. (1975) became the first operational bio-optical ocean model. They used a Monte Carlo simulation of the radiative transfer equation to relate the apparent

optical properties (AOPs) to the IOPs in oceanic waters containing OACs, molecular water and chl-*a*. For inland waters, the first bio-optical model that related the AOPs to its IOPs was developed for Lake Ontario, Canada, by a Monte Carlo simulation of the radiative transfer equation and non-linear multivariate optimization analyses (BUKATA, 1979). Bukata et al. (1981a,b) used a multispectral radiance data recorded by the Nimbus-7 Coastal Zone Color Scanner (CZCS) to establish relationships between AOPs, IOPs and OAC that enabled the simultaneous extraction of concentrations of chl-*a*, total suspended solids (TSS), and CDOM from a single full spectrum satellite, aircraft, or ship-borne satellite-mimic determination of lake water color.

2.2. Optical Properties of Water

The optical properties of water are grouped into IOPs and AOPs. The first group is related to those properties that depend only upon the environment, thus, they are independent of the environment light field. The two most essential IOPs are the total absorption coefficient (*a)* and the total scattering coefficient (*b)* since the sum of both coefficient is the attenuation coefficient. AOPs, on the other hand, are those properties that depend on the environment (and on IOPs) and also on the directional structure of the environment light field. AOPs are also used as descriptors of a water body due to their regular features and stability. The most common AOPs are the irradiance reflectance (*R*), the remote-sensing reflectance (R_{rs}), and various diffuse attenuation functions (MOBLEY, 2001).

IOPs are easily explained schematically with the help of Figure 2.1, in which it is possible to see an imaginary, infinitesimally thin, plane parallel layer of medium, illuminated at right angles by a parallel beam of monochromatic light. Figure 2.1A shows an incident radiant flux (Φ_0) – measured in energy or quanta per time unit – in the plane parallel layer of medium and also a transmitted radiant flux (Φ_t). If $\Phi_0 = \Phi_t$, the energy that enters the system is totally transmitted into the medium. If $\Phi_0 > \Phi_t$, it means there is an attenuation of the energy when it achieves the medium. This attenuation can occur through three different

processes shown on Figures 2.1B, C and D. Figure 2.1B shows the medium can absorb (Φ_a) part of the Φ_0, attenuating the Φ_t. Figure 2.1C shows the medium may scatter (Φ_b) forward and backward Φ_0, instead of absorbing it. Figure 2.1D shows a combination of absorption and scattering processes, most resembling processes in a natural environment.
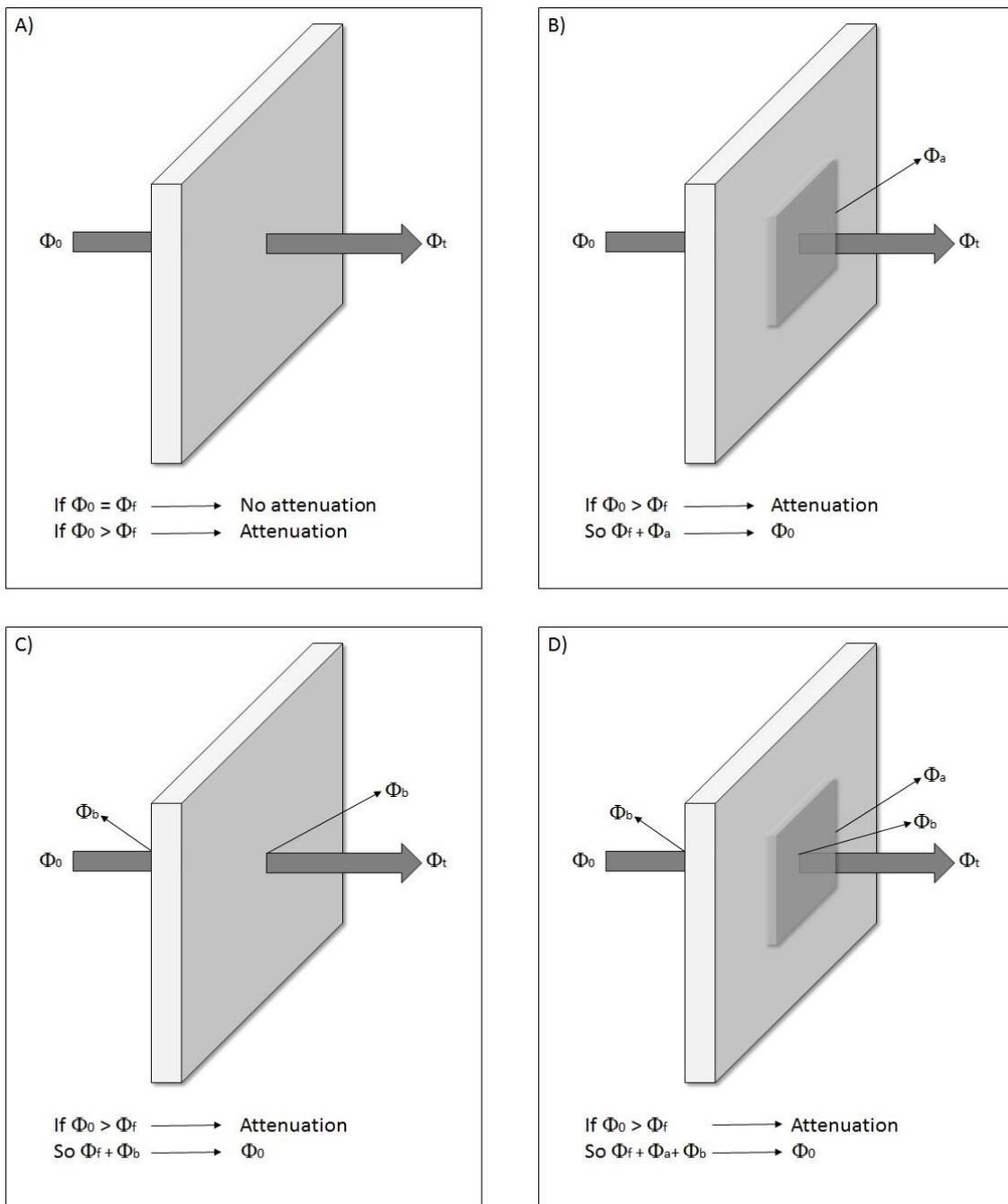
Figure 2.1 – Different types of interactions between a light beam and a thin layer of aquatic medium

Thus it is possible to conclude that attenuation is a sum of scattering and absorption processes, as written in equation 2.1.

$$c = a + b \qquad \qquad (2.1)$$

Where: c is the attenuation, a and b are the absorption and scattering processes, respectively.

AOP is a ratio of two radiometric quantities which are the basic properties of light measured by optical sensors. This rationing removes effects of the magnitude of the incident sky radiance onto the aquatic surface. One example of this occurs when the sun goes behind a cloud, the downwelling and upwelling irradiances within water may change by an order of magnitude within a few seconds, but their ratio will be nearly constant. This is why AOPs cannot be measured in laboratory or in water sample; they must be measured *in situ*. A list of the main IOPs, AOPs and radiometric quantities are shown on Table 2.1.

Table 2.1 – IOPs, AOPs and Radiometric Quantities commonly used in optical hydrology

Quantity	Units (SI)	Simbology
Inherent optical properties		
Absorption coefficient	m^{-1}	a
Volume scattering function	$m^{-1} sr^{-1}$	β
Scattering phase function	m^{-1}	$\beta\sim$
Scattering coefficent	m^{-1}	b
Backscatter coefficient	m^{-1}	b_b
Beam attenuation coefficient	m^{-1}	c
Single-scattering albedo	-	ϖ_0
Apparent optical properties		
Irradiance reflectance (ratio)	-	R
Remote sensing reflectance	sr^{-1}	R_{rs}
Remote sensing reflectance (sub)	sr^{-1}	r_{rs}
Attenuation coefficients:		
of radiance L(z, θ, φ)	m^{-1}	$K(\theta, \varphi)$
of downwelling irradiance $E_d(z)$	m^{-1}	K_d
of upwelling irradiance $E_u(z)$	m^{-1}	K_u
of PAR	m^{-1}	$KPAR$
Radiometric Quantities		
Quantity of radiant energy	$J\ nm^{-1}$	Q
Power	$W\ nm^{-1}$	Φ
Intensity	$W\ sr^{-1}\ nm^{-1}$	I
Radiance	$Wm^{-2}\ sr^{-1}\ nm^{-1}$	L
Upwelling radiance	$Wm^{-2}\ sr^{-1}\ nm^{-1}$	L_u
Sky radiance	$Wm^{-2}\ sr^{-1}\ nm^{-1}$	L_s
Water leaving radiance	$Wm^{-2}\ sr^{-1}\ nm^{-1}$	L_w
Downwelling plane irradiance	$Wm^{-2}\ nm^{-1}$	E_d
Upwelling plane irradiance	$Wm^{-2}\ nm^{-1}$	E_u
Net irradiance	$Wm^{-2}\ nm^{-1}$	E
Scalar irradiance	$Wm^{-2}\ nm^{-1}$	E_0
Downwelling scalar irradiance	$Wm^{-2}\ nm^{-1}$	E_{0d}
Upwelling scalar irradiance	$Wm^{-2}\ nm^{-1}$	E_{0u}
Incident spectral irradiance	$Wm^{-2}\ nm^{-1}$	E_s
Photosynthetic available radiation	$Photons\ s^{-1}m^{-2}$	PAR

Source: adapted from Mobley (2001)

2.3. Bio-optical modeling

The expression "bio-optical" was first used in a report of the Scripps Institute of Oceanography by Smith and Baker (1977) to describe a "state of ocean waters". The "state" that the authors referred in this definition is the fact that in many oceanic waters, the optical properties of water are essentially subordinated to the biological activity, mainly to the phytoplankton and its derivatives. However, nowadays this expression has been followed by nouns like model or algorithms.

A bio-optical model or algorithm can have at least 2 different meanings and objectives. The first and most used meaning refers to various ways of describing and forecasting the "bio-optical state" of the aquatic system. It means that the optical properties are just a function of the biological activity (MOREL, 2001) in the water body. The goal of this first meaning is to derive the biological activity by establishing a statistically significant relationship. These models are essentially empirical and descriptive (MOREL, 2001). The second meaning refers to a tool which is used to analyze, and then to predict, the optical properties of biological materials. The goal, different from the first one, aims to derive optical properties, mainly IOPs from the aquatic systems. To achieve this, they focus on the various ways of quantifying the optical properties and the light within the water are described by fundamental theories of optics and in the radiative transfer theory (MOBLEY, 2001).

In the literature it is possible to find many types of bio-optical models such as: empirical, semi-empirical, semi-analytical and quasi-analytical. Based on the two described meanings we can classify empirical and semi-empirical in the class of algorithms that aim to estimate the biological activity. They are develop from a statistical regression between *in-situ* measurements of limnological parameters and radiometric data from satellite or proximal remote sensing devices. The difference between empirical and semi-empirical relies on the physical explanation for the algorithm development. As we could observe, both

13

of them are statistically correlated to a biological activity, however the physics behind them are different. While in an empirical algorithm the choice of the wavelength is based on the best correlation result, like in neural networks algorithms which uses computer based statistics to find the best correlated wavelengths; in the semi-empirical algorithm the wavelengths choices are made by physical assumptions based on the spectral behavior of the target (MOREL; GORDON, 1980), for example, the "Red-Edge" used in the vegetation indices. The results of these models were then related to the biological activity by the use of regression analysis.

Semi and quasi-analytical models can be classified in the class of algorithms that aim to estimate the optical properties of the aquatic system. They rely on the inversion of mathematical relationships among AOPs to estimate IOPs based in analytical and empirical approaches. The derivation is commonly based on the reflectance model proposed by Gordon et al. (1975, 1988) which describes the relationship between remote sensing reflectance and IOPs (Equation 2.2).

$$r_{rs}(\lambda) = \frac{L_u(0^-,\lambda)}{E_d(0^-,\lambda)} = g_1\left(\frac{b_b(\lambda)}{a(\lambda)+b_b(\lambda)}\right) + g_2\left(\frac{b_b(\lambda)}{a(\lambda)+b_b(\lambda)}\right)^2 \qquad (2.2)$$

Where: $r_{rs}(\lambda)$ is the remote sensing reflectance just below water surface, $a(\lambda)$ is the spectral total absorption coefficient, $b_b(\lambda)$ is the spectral total backscattering coefficient, $L_u(0^-,\lambda)$ and $E_d(0^-,\lambda)$ are upwelling radiance and downwelling irradiance, respectively, and g_1 and g_2 are geometrical factors.

However several studies have been simplified the reflectance model (Equation 2.2) by omitting the quadratic term, using equation 2.3.

$$r_{rs}(\lambda) = \frac{f}{Q}\left(\frac{b_b}{a+b_b}\right) \qquad (2.3)$$

Where: f is the anisotropic factor of the downwelling light field (KIRK, 1994) and Q is the geometrical factor (GONS, 1999).

The *f* value is a function of the solar elevation angle (KIRK, 1994) and can be reasonably well expressed as a linear function of μ_0 – the mean cosine of the zenith angle – and can be determined as in equation 2.4:

$$f = 0.975 - 0.629\,\mu_0 \tag{2.4}$$

The value of μ_0 is calculated according to the sampling time, locations (latitude and longitude) and solar zenith angle (MARTIN; McCUTCHEON, 1999; REES, 2001). For the *Q* value it was proposed (GONS, 1999) an empirical equation for turbid inland waters under different solar elevation angles, as expressed in equation 2.5:

$$Q = \frac{2.38}{\mu_0} \tag{2.5}$$

A factor of 0.544 was proposed by Austin (1980) to relate the radiance just above the surface to radiance just beneath the surface. Therefore, remote sensing reflectance just above the water surface (R_{rs}) can be determined as in equation 2.6:

$$R_{rs}(\lambda) = 0.544\,\frac{f}{Q}\left(\frac{b_b}{a + b_b}\right) \tag{2.6}$$

Where: $R_{rs}(\lambda)$ is the remote sensing reflectance just above the water surface.

There are some studies that instead of R_{rs} or r_{rs} prefer to use the Irradiance Reflectance Ratio (*R*), then its relation to the POIs follows equation 2.7.

$$R(0^-) = \frac{E_u(0^-)}{E_d(0^-)} = f\left(\frac{b_b}{a + b_b}\right) \tag{2.7}$$

Where: $R(0^-)$ is the irradiance reflectance ratio just beneath the water surface, E_u and E_d *are* upwelling and downwelling irradiance, respectively.

From these simplifications of Equation 2.2, several semi-analytical and QAA have been proposed for deriving the IOPs in Case 1 waters (MARITORENA et al., 2002; LEE et al., 2002). For Case 2 waters semi-analytical and QAA have been proposed just recently by Li et al. (2012), Mishra et al. (2014) and Li, et al. (2013). The main difference between semi and QAA is based on the estimation of the *a(λ)* and *b$_b$(λ)*. In the QAA the estimation of the total absorption coefficient does not depend on others IOPs estimations such as the absorption coefficients of phytoplankton, Non algal particles (NAP) and Colored Detrital Matter (CDM) like in semi-analytical algorithms. Instead of it, QAA estimates total absorption coefficient directly from R$_{rs}$ and the it is further decomposed spectrally into others absorption coefficients when necessary.

Thus, the *a(λ)* in semi-empirical algorithms is usually described as the sum of all other absorptions coefficients equation 2.8.

$$a(\lambda) = a_w(\lambda) + [chl-a]a^*_{phy}(\lambda) + [NAP]a^*_{nap}(\lambda) + [CDOM]a^*_{cdom}(\lambda)$$

(2.8)

Where: *[chl-a]* and *[NAP]* denote concentrations of chl-*a* and NAP, respectively; *[CDOM]* denotes the absorption of CDOM at 440 nm; *a$_w$(λ)* is the spectral absorption coefficient of pure water; and a*$_{phy}$*(λ)*, a*$_{NAP}$*(λ)* and a*$_{CDOM}$*(λ)* are spectral specific absorption coefficients for phytoplankton, NAP and CDOM, respectively.

Instead of it, for QAA, the *a(λ)* is calculated in QAA version 5 (QAAv5) (LEE et al., 2009), according to the equation 2.9.

$$a(\lambda) = \frac{\left(1 - u(\lambda)\right)\left(b_{b,w}(\lambda) + b_{b,p}(\lambda)\right)}{u(\lambda)}$$

(2.9)

Where: *u* is calculated from a relation among back scattering coefficient (*b$_b$(λ)*), to the sum of total absorption coefficients and *b$_b$(λ)*; *b$_{b,w}$(λ)* is the spectral backscattering coefficient of pure water; and *b$_{b,p}$(λ)* is the spectral backscattering coefficient of particulate matter.

The $b_b(\lambda)$ is also usually expressed as the sum of the backscattering coefficients for each constituent in water except for CDOM, as in equation 2.10:

$$b_b(\lambda) = b_{b,w}(\lambda) + [chl - a]b_{b,phy}(\lambda) + [NAP]b_{b,NAP}(\lambda) \tag{2.10}$$

Where: $b_{b,phy}(\lambda)$ and $b_{b,NAP}(\lambda)$ are spectral backscattering coefficients for phytoplankton and NAP.

Once again in QAA the $b_b(\lambda)$ is calculated differently (LEE et al., 2009), according to the equation 2.11.

$$b_b(\lambda) = b_{b,w}(\lambda) + b_{b,p}(\lambda_0)\left(\frac{\lambda_0}{\lambda}\right)^\eta \tag{2.11}$$

Where: λ_0 is the target wavelength, $b_{b,p}$ is backscattering coefficients of suspended particles and η is calculated from equation 2.12.

$$\eta = 2\left(1 - 1.2exp\left(-0.9\frac{r_{rs}(443)}{r_{rs}(\lambda_0)}\right)\right) \tag{2.12}$$

To summarize the classification of bio-optical algorithms, Figure 2.2 presents a flowchart which shows the division of the bio-optical algorithms in two types : the ones that estimate biological activity and the ones that estimate the optical properties. Each type has a different goal and its own procedures to achieve its products.
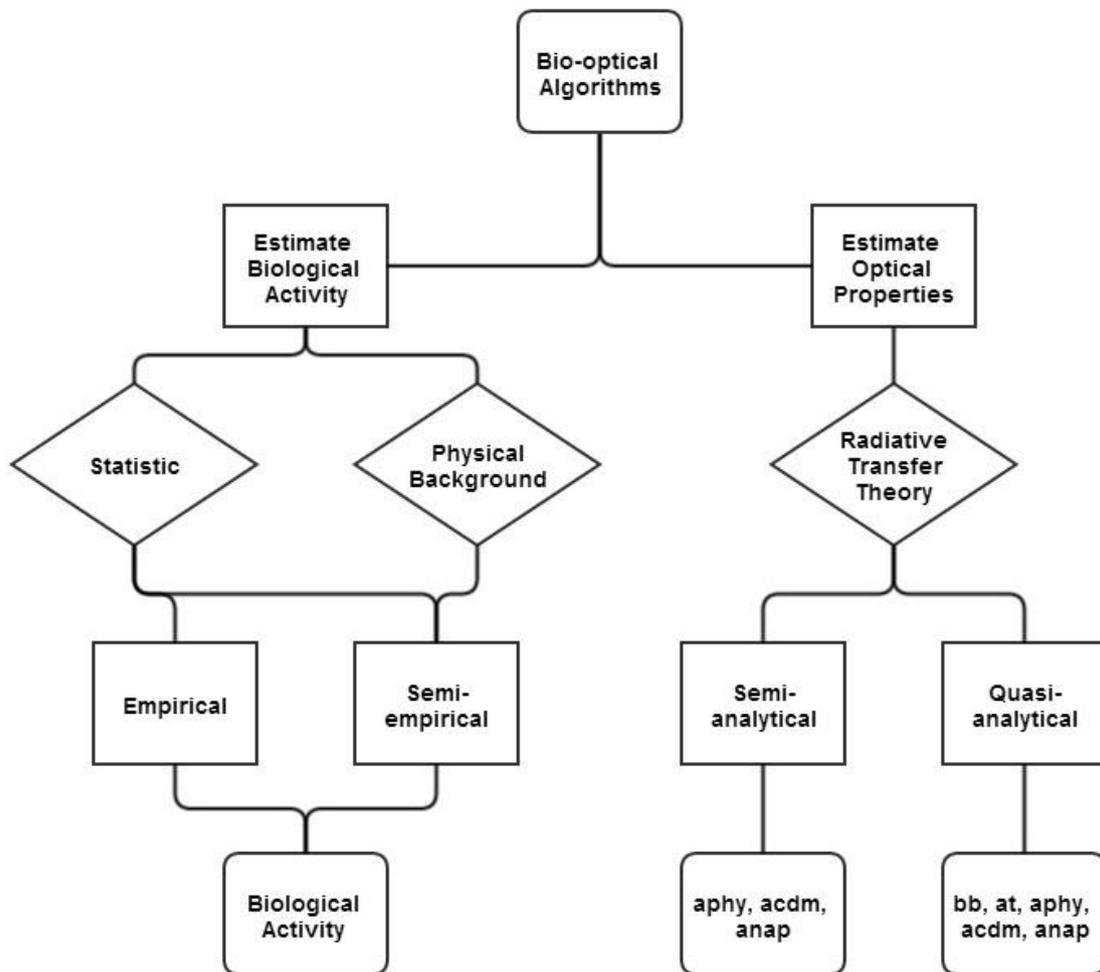
Figure 2.2 - Flowchart of bio-optical models classification and goals

2.3.1. Bio-optical models for predicting PC

Three methods have been used to develop empirical models for PC concentration estimation. A regression procedure was used by Vincent et al. (2004) in a study developed at Lake Erie, one of the Laurentian Great Lakes, and used Thematic Mapper (TM) and Enhanced Thematic Mapper Plus (ETM+) sensors from Landsat 5 and 7 respectively to acquire the radiometric data. As described in the methodology of the study, there was no preconceived notions of which were the best bands or spectral bands to be used in the modeling. The

authors entered all TM and ETM+ spectral bands and let the multiple regression method sort the best ones out. Thus they elaborate two empirical models one for the combinations of single bands and another one for the combinations of spectral band ratios (VINCENT et al., 2004). Despite the fact that the authors tried to achieve the best coefficient of correlation, this study enhanced that the use of band ratios suppress the interference of the specular reflection from water under wavy conditions. Another technique to choose empirically the spectral bands to be used in an empirical algorithm is the genetic algorithm and partial least squares (GA–PLS) method (SONG, et al., 2012). In this study, GA–PLS was used as a combination of GA with PLS regression for spectroscopic analysis from proximal and airborne hyperspectral data. GA method was used for selection of the spectral variables and PLS was used to evaluate the relation among selected spectral variables and the biological activity, in this case the PC. In a recent study, Song et al. (2013a) used an optimal band ratio modeling (OBM) approach to generate several band ratios in order to estimate PC concentration. Although they used bands that could be explained physically and are very similar to some semi-empirical models, the use of OBM which is an empirical method that makes the choice of spectral bands more dependent of the correlogram. Sun et al. (2013) also used a correlogram analysis to estimate the best correlations among band ratios for PC detection. They classified waters in three different types and then related each water type to several band-ratios.

Several semi-empirical algorithms have been developed to quantify PC in inland waters. As they are classified as semi-empirical, spectral bands selection relies on PC specific spectral patterns such as its absorption peak around 620nm and its fluorescence peak around 650nm. The first semi-empirical bio-optical model was the developed by Dekker (1993) and is known as the baseline algorithm and uses two wavelengths (600 and 648 nm) to draw a reference baseline, and relates PC concentration to the distance from the midpoint of the baseline to the reflectance at 624 nm which is related to the PC absorption peak for the author measures. Another semi-empirical algorithm was proposed by Schalles and

Yacobi (2000) and it is known as the single reflectance ratio, which uses PC fluorescence peak reflectance at 650 nm as reference, and then targets the PC absorption at 625 nm. One of the most cited PC semi-empirical algorithm is the nested band ratio which was developed for the spaceborn Medium Resolution Imaging Spectrometer (MERIS) sensor band settings from the European Space Agency (ESA). It relates PC to its absorption peak at 620nm which is also the center of band 6 of MERIS. The PC is retrieved from the ratio of the 620 nm band and a near infra-red (NIR) band, centered at 709 nm, as reference. The algorithm also has a second band ratio (709/665nm bands) which is used to infer a correction for the absorption of chl-*a* at the 620 nm spectral band. Another band (centered at 779 nm) is used to calculate the backscattering coefficient that is introduced in the two band ratios, to retrieve the absorption coefficients through inversion of a reflectance model (SIMIS et al., 2005). Wynne et al. (2008) developed a spectral shape (SS) algorithm using the water leaving radiance (L_w) from MERIS at 681, 709 and 665 nm. This algorithm allowed the authors to distinguish bloom and non-bloom conditions on Bear Lake, Michigan, USA. However, this algorithm does not retrieve PC concentration, it just retrieve two classes: a positive value or a negative value of radiance. Wynne et al. (2010) proposed a cyanobacteria index (CI) using the SS algorithm in order to classify the occurrence or not of CHABs. A positive CI is indicative of elevated densities of cyanobacteria while the negative CI is indicative of no CHABs. Hunter et al. (2008) adapted the three band model proposed by Gitelson et al. (2008) used for the retrieval of chl-*a* from MERIS data to propose a PC three band model. They applied their algorithm using an Analytical Spectral Devices (ASD) FieldSpec® HandHeld Spectroradiometer (ASD Inc., Boulder, CO, USA) spectrophotometer to experimental cultures of cyanobacteria. The model was achieved by setting reflectance from 630, 660 and 750 nm as the reference wavelengths for the PC retrieval model. Hunter et al. (2010) proposed an update on their previous three band algorithm for two airborne hyperspectral sensors - Compact Airborne Spectrographic Imager-2 (CASI-2) (ITRES Research Ltd., Calgary, AB, Canada) and Airborne Imaging

Spectrometer for Applications Eagle (AISA Eagle) (SPECIM, Oulu, NO, Finland) - changing the spectral bands to 600, 615 and 725 nm. The new single reflectance ratio (MISHRA et al., 2009) used a proximal remote sensing sensor USB 4000 radiometer (Ocean Optics, Inc., Dunedin, FL, USA). The algorithm uses the reflectance at 700 nm as reference and targets PC absorption at 600 nm in order to minimize the chl-*a* interference. Le et al. (2011) based on a four-band algorithm for chl-*a* estimation (LE et al., 2009) developed a four-band algorithm for PC concentration estimation. The spectral bands for this algorithm were chosen according to the same characteristics used in the chl-*a* four bands model. Thus the first band should be the most sensitive for PC, which the authors chose 630nm. The second spectral band should have less interference of PC absorption and should have a difference on the absorption coefficients of NAP and CDOM, then it was chosen the 645 nm. Third and fourth bands were chosen to minimize the effect of backscattering from TSS, then 730 and 695 nm were chosen as the wavelengths for the third and fourth bands respectively. Dash et al. (2011) used the Ocean Color Monitor (OCM) sensor to develop a spectral reflectance slope algorithm in order to map cyanobacteria in a small freshwater lake. The slope algorithm proposed by the authors OCM uses OCM bands 4 and 5, located at 510.6 and 556.4nm respectively. This spectral range was use to identify PC even without the absorption peak at 620nm. Thus, due to OCM spectral resolution the slope between bands 4 and 5 was used to identify the low PC absorption coefficient values. Domínguez et al. (2011) proposed a Normalized Difference Phycocyanin Index (NDPCI) for MERIS and Compact High Resolution Imaging Spectrometer (CHRIS) spectral bands. The authors used for the index bands around 705 which is the near the fluorescence of chl-*a* (MERIS band 9 and CHRIS band 14) and the absorption peak of PC, centered at 620 nm (MERIS band 6 and CHRIS band 9). Wheeler et al. (2012) also applied the concept of Red/NIR algorithms, from chl-*a* bio-optical models for case 2 waters, for estimating PC on Quickbird and MERIS images at Missisquoi Bay, USA.

2.3.2. Bio-optical models for predicting IOPs (including a_{PC})

Two algorithms have been developed to estimate IOPs from case 2 waters which include the a_{PC}. Li et al. (2012) developed an algorithm to estimate the a_{PC} based on two steps which consisted of the use of three-band semi-empirical algorithms to estimate pigments absorption coefficients, and the calculation of $a_{PC}(624)$ by removing the interference from the absorption of other constituents. In this algorithm the authors used Hunter et al. (2010) semi-empirical algorithm structure to generate two relations among estimated absorptions coefficients of different wavelengths. They used the R_{rs} at 725nm to correct for the backscattering effect, the R_{rs} at 624nm due to its sensitiveness to PC concentration caused by its maximal absorption at around 620nm, and bands 600 nm and 648 nm could correct the effects of CDM and backscattering since both of them are close to band 624 nm. Then the R_{rs} from the semi-empirical algorithms were replaced for relation proposed by Gordon et al. (1975, 1988), resulting on equations 2.13 and 2.14.

$$R31 = \cfrac{b_b(725)}{\begin{array}{l} a_w(725) + a_{cdm}(725) + a_{phy}(725) + b_b(725) \\ \times \cfrac{a_w(624) + a_{cdm}(624) + a_{phy}(624) + b_b(624)}{b_b(624)} \\ - \cfrac{a_w(600) + a_{cdm}(600) + a_{phy}(600) + b_b(600)}{b_b(600)} \end{array}} \qquad (2.13)$$

Where: R31 is the first three band model structure used.

$$R32 = \cfrac{b_b(725)}{\begin{array}{l} a_w(725) + a_{cdm}(725) + a_{phy}(725) + b_b(725) \\ \times \cfrac{a_w(624) + a_{cdm}(624) + a_{phy}(624) + b_b(624)}{b_b(624)} \\ - \cfrac{a_w(648) + a_{cdm}(648) + a_{phy}(648) + b_b(648)}{b_b(648)} \end{array}} \qquad (2.14)$$

Where: R32 is the second three band model structure used.

Based on the assumptions that $b_b(\lambda)$ at 600, 624 and 648 nm is not significantly different and $a_{cdm}(725)=a_{phy}(725)\approx0$ (SIMIS et al., 2005, 2007); the a_{PC} can be estimated by equation 2.15.

$$a_{pc}(624) = a_{ph}(624) - 0.5 \times \left[a_{ph}(600) + a_{ph}(648)\right] \qquad (2.15)$$

Mishra et al. (2013, 2014) developed a QAA in order to estimate the $a_{phy}(\lambda)$ from proximal R_{rs} collected in highly turbid catfish ponds. They also developed a technique to further decompose the $a_{phy}(\lambda)$ in order to obtain a_{PC}, at 620 nm – the peak of PC absorption spectrum. $a_{phy}(\lambda)$ was estimated through the QAA (LEE et al., 2002) which is a multi-band inversion algorithm that inverts absorption coefficients. a_{PC} estimation was based on the assumption that $a_{phy}(\lambda)$ provides information about the absorption by all intracellular phytoplankton pigments (MISHRA et al., 2013). The decomposition was based on equation 2.16 and 2.17 which were based on Simis et al. (2005) relation among chl-*a* and PC contributions to the absorption at 620nm.

$$a_{phy}(665) \approx a_{chl}(665) + a_{PC}(665) \qquad (2.16)$$

Where: a_{chl} is the absorption coefficient of chl-*a*.

$$a_{phy}(620) \approx a_{chl}(620) + a_{PC}(620) \qquad (2.17)$$

a_{PC} was finally defined through the solution of these two equations by equation 2.8

$$a_{PC}(620) = \frac{\varphi_1 a_{phy}(620) - a_{phy}(665)}{\varphi_1 - \varphi_2} \qquad (2.18)$$

Where: φ_1 is the ratio between $a_{chl}(665)$ and $a_{chl}(620)$ and φ_2 is the ratio between $a_{PC}(665)$ and $a_{PC}(620)$.

2.3.3. Estimation of PC concentration

To estimate PC concentration from the a_{PC}, Simis et al. 2005; Li, et al. (2012) and Mishra et al. (2013) used the specific absorption coefficient of PC (a^*_{PC}).

The PC concentration is estimated by a ratio between the a_{PC} and a^*_{PC} at 620nm, expressed in equation 2.19.

$$[PC] = \frac{a_{PC}(620)}{a^*_{PC}(620)}$$
(2.19)

2.3.4. Summary of PC bio-optical models

A summary with visual geographic location of all PC bio-optical models exemplified here is shown on Figure 2.3. It is important to notice that Figure 2.3 only enhance the studies that develop algorithms not the studies that applied the bio-optical models. It was observed that there is no PC bio-optical model developed on the Southern Hemisphere or in the tropical region of the planet. This fact enhances the need for a re-parameterization of a bio-optical algorithm for tropical regions. It is also important to highlight that the development of semi and quasi-analytical bio-optical algorithms have been produced just in recent years while empirical and semi-empirical algorithms were older. This difference could be explained by the technology and labor intensity required from each of these two groups of bio-optical models. Semi and quasi-analytical bio-optical models depend on several measures of r_{rs}, absorption and backscattering coefficients which could not be measured years ago due to the lack of equipment. On the other hand, empirical and semi-empirical algorithms just depend on the reflectance or radiance measures and the limnological parameters to be developed. A list of all model referenced above is shown on Appendix A in the end of this Master Thesis.
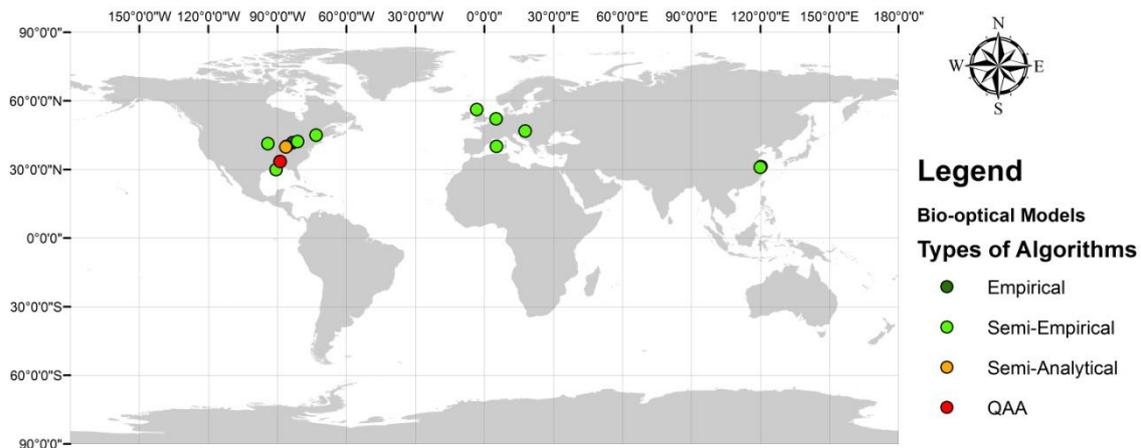
Figure 2.3 - Location of PC bio-optical algorithms developed in the literature

2.4. Sensor applicability

The first sensor dedicated to aquatic environments was the Coastal Zone Color Scanner (CZCS) aboard Nimbus-7 launched in 1978. Therefore, by the launch of satellites and earth observing sensors such as ERTS-1/Landsat-1 and Nimbus-7, the basis of marine optics were successfully improved enabling remote multispectral sensors to monitor water color and, by inference, water quality. Several others satellite sensors which could be use for water monitoring were launch after the CZCS such as the Landsat family (2 to 8), Sea-viewing Wide Field-of-view Sensor (SeaWiFS), Advanced Earth Observing Satellite (ADEOS), Hyperion, Australian Resource Information and Environmental Satellite (ARIES), Moderate Resolution Imaging Spectroradiometer (MODIS), and MERIS.

Although the great number of Earth Observing sensors we still have a lot of limitations for the use of satellite sensors in order to monitor water quality. These limitations can be divided in two groups: the sensor limitation and the environmental conditions limitations. Sensor limitations are related to their resolutions (radiometric, spatial, spectral and temporal) and to signal-to-noise ratio. Radiometric resolution is the one which refers to the absolute amounts of

reflectance that can be measured by the sensor while the spatial resolution limits the finest spatial detail measureable (the pixel size) which is important according to the size of the aquatic system. Spectral resolution is the most important for the accuracy of bio-optical models, since it determines how detailed the spectral reflectance can be measured. The temporal resolution represents the nominal frequency with which images of the same area are acquired. For monitoring capability, the temporal and spatial resolutions are the most important resolutions in a sensor.

Environmental limitations are the ones that is not caused by the sensor, but by environmental factors. Weather dependency is one of the most important factors, since the image acquisition may be compromised by adverse atmospheric conditions, which are dependent on season and geographical location. Other atmospheric compounds like cloud, haze, fog, smoke or dust can also compromise the frequency of earth observations over a target area. It is important to enhance that the detection of water quality variables is restricted to variables that have a direct influence on water optical conditions. It is also important to enhance that these few variables that influence bio-optical models were located in the top one or two meters of inland, since most of the optical remote sensing signal cannot be derived from deeper zones. In the marine optics the sea state is also an important environmental limitation for its successfulness.

However for PC estimation, due to the small peak of PC absorption around 620 nm, the spectral resolution is an important characteristic of the sensor that interferers on the performance of the model. Then, few sensors have the appropriated spectral bands for the estimation of PC. Hyperspectral orbital sensors such as CHRIS, Hyperion and Hyperspectral Imager for the Coastal Ocean (HICO) could be used to map PC in a reservoir due to their high spectral resolution. However, their use for monitoring programs is compromised by their temporal resolution. The use of multi-spectral orbital sensors is reduced due to the lack of spectral bands on the absorption peak of PC. MERIS was the only

multispectral sensor with a spectral band around 620 nm, however as ENVISAT stopped communicating with ground stations in the middle of 2012, the use of MERIS for aquatic studies is compromised.

New hyperspectral sensors such as Environmental Mapping and Analysis Program (EnMAP), Hyperspectral Infra-red Imager (HyspIRI) and PRecursore IperSpettrale della Missione Applicativa (PRISMA) have been developed to improve hyperspectral measures from the space. EnMAP is a German hyperspectral satellite mission providing high quality hyperspectral image data on a timely and frequent basis. It will provide over 240 continuous spectral bands in the range between 420 and 2450 nm with a spatial resolution of 30 m. The sensor will work in a push broom configuration. and will provide global coverage in quasi nadir mode (±5°) from a sun-synchronous orbit (STUFFLER et al., 2009). HyspIRI is a global mapping mission that was recommended by the National Research Council's Earth Sciences Decadal Survey (NRC, 2007). It will include two sensors: a visible, near−infrared and shortwave infrared (VSWIR) imaging spectrometer and multispectral thermal infrared (TIR) instrument. The VSWIR instrument will have 213 spectral channels between 380 and 2500 nm on 10 nm centers. Its spatial resolution for both instruments will be 60 m at nadir (ROBERTS et al. 2012). PRISMA is a remote sensing space mission under development by the Italian Space Agency (ASI). It will provide hyperspectral images of the Earth with a spatial resolution of 30m, and 250 spectral bands with a spectral resolution better than 10 nm. The spectral ranges covered by the sensor are visible and near infrared (VNIR) and short wave infrared (SWIR) bands. It will also have a panchromatic band with 5m of spatial resolution which will be co-registered to the hyperspectral bands in order to allow the fusion techniques on PRISMA's images (LABATE et al., 2009). Although these improvements, the revisit times at the equator for each of these sensors will be: on demand, 19 days and 25 days for EnMAP, HyspIRI and PRISMA respectively (DEKKER; HESTIR, 2012).

To substitute ENVISAT, ESA has proposed the Sentinel constellation in which there will be on board of its third satellite, Sentinel-3, the Ocean and Land Colour Instrument (OLCI). This sensor has similar specifications as the MERIS because of this, it will provide data continuity of MERIS on ENVISAT (DONLON et al., 2012). However, OLCI will have 21 spectral bands which are few more bands than in the MERIS which will be use mainly for a more accurate atmospheric correction. Table 2.2 shows all OLCI bands and on the shaded areas are the new bands. The sensor will have a swath width of 1270 km (FOV of 68°, but slightly tilted) and a spatial resolution of 300 m. It is tilted 12.6° westwards to avoid sun-glint over water, which may have some effects over land too (CLEVERS; GITELSON, 2013). Due to the satellites constellation strategy it has been planned two Sentinel-3 satellites. The revisit time at the equator for OLCI (sun glint free) using one satellite is 3.8 days, however using the two planned satellites this time will reduce to 1.9 days (ESA, 2012). For more details of OLCI sensor, a table with key characteristics is shown on Annex A. Another multispectral mission that will be develop is the SABIA-MAR mission which will have two sensors to image earth in a global and regional scale. The mission was conceived to provide information and products to studies of ocean ecosystems, carbon cycling, marine habitats mapping, coastal hazards, and coastal land cover/land use (CHAMON. 2013).

Table 2.2 - Specifications of the OLCI on the Sentinel-3 satellite system; shaded areas are the ones that were included from MERIS specifications.

Spectral band	Center wavelength (nm)	Band width (nm)
O1	400	15
O2	412.5	10
O3	443	10
O4	490	10
O5	510	10
O6	560	10
O7	620	10
O8	665	10
O9	673.75	7.5
O10	681	7.5
O11	709	10
O12	754	7.5
O13	761	2.5
O14	764.375	3.75
O15	767.5	2.5
O16	779	15
O17	865	20
O18	885	10
O19	900	10
O20	940	20
O21	1020	40

Source: ESA, 2012.

These characteristics show that OLCI is a potential sensor for CHABs monitoring since it has a spectral band on the PC absorption peak and it will be freely available with a high temporal resolution and the adequate spectral bands for water quality monitoring, mainly PC and chl-*a*. As well as other satellites from the Sentinel family, Sentinel 3 will have a global coverage once the second system will be acquiring images. Dekker and Hestir (2012) attributed MERIS as the most suitable satellite sensor system with sufficient temporal frequency for inland and near-coastal water quality. As OLCI is the successor of MERIS and because of the number of spectral bands (MERIS=15, OLCI=21), OLCI has

been treated as a potential tool for remote sensing of water quality researches (DEKKER; HESTIR, 2012; SONG et al. 2013b).

3 STUDY AREA, MATERIALS AND METHODS

3.1. Study Area

The study area (Figure 3.1) of this research was a hydroelectric reservoir - the Funil Reservoir (22º32' S and 44º45' W). The reservoir has a 16800 km^2 catchment area, surface of 40 km^2, mean depth of 22 m, maximum depth of 70 m and total volume of 8.9 x 10^9 m^3. The retention time varies from 10 to 50 days according to the season of the year (ROCHA et al., 2002). It drains water from the hydrographic basin of Paraíba do Sul river, in Southeast Brazil, and it is located between the cities of Itatiaia and Resende in the state of Rio de Janeiro. This hydrographic basin connects three economically important Brazilian states including Minas Gerais, Rio de Janeiro, and São Paulo.
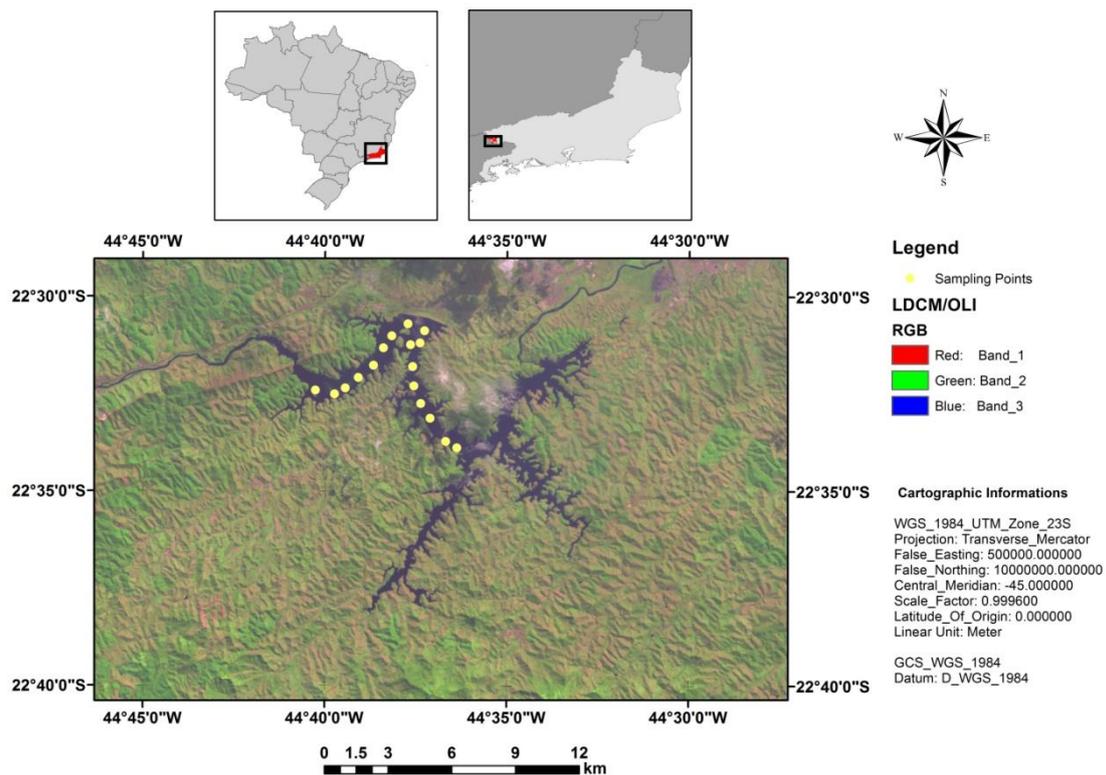
Figure 3.1 - Location of Funil Reservoir and sampling points in the State of Rio de Janeiro, Brazil

Funil Reservoir was constructed during the late 1960s with the purpose of being an important hydroelectric power generation source. However, Branco et al. (2002) also computed that the Funil reservoir also serves as the primary source of drinking water for domestic supply, irrigation, industrial self-supply systems and aquaculture. However, the reservoir receives waste from one of the main Brazilian industrial areas with a large range of industries: 19 chemical, 26 siderurgical and metallurgical, 5 electric and eletronic, 1 petrochemical, 3 paper and cellulose and few others food and textile industries (PRIMO, 2006).

As consequence of the draining of all these industrial waste the income of nutrients has been increasing. Because of this, it has been observed the enhance of the eutrophication process in recent decades (BRANCO et al., 2002). Thus, the Funil Reservoir showed to be a favorable environement for the development of CHABs. Ferrão-Filho et al. (2009) analyzed Funil Reservoir from June, 2002 to March, 2006 and concluded that Funil is a cyanobacterial dominated reservoir. The authors found three main species of cyanobacterias which are potentially producers of microcystins (a hepatotoxin) and saxitoxins (a neurotoxin): *Anabaena circinalis*, *Cylindrospermopsis raciborskii* and *Microcystis spp.* Ferrão-Filho et al. (2009) also found that the concentration of these cyanotoxins were also found on zooplankton cells (*Daphnia pulex*) showing that they had been contaminated. A study of phytoplankton community of Funil Reservoir conducted by the Rio de Janeiro State Environmental Institute (INEA) showed that from all cells of phytoplankton (8,324,750 cells) cyanobacteria represents aproximatelly 94.30% (7,850,166 cells) (ARAUJO et al., 2010). Figure 3.2 shows a phytoplankton bloom at Funil Reservoir during a field campaing on May of 2012. Figure 3.2A shows a view of the water surface with algae blooms and Figure 3.2B shows a closer look on the algal bloom. It is possible to notice the development of thick surface scums on the reservoir.
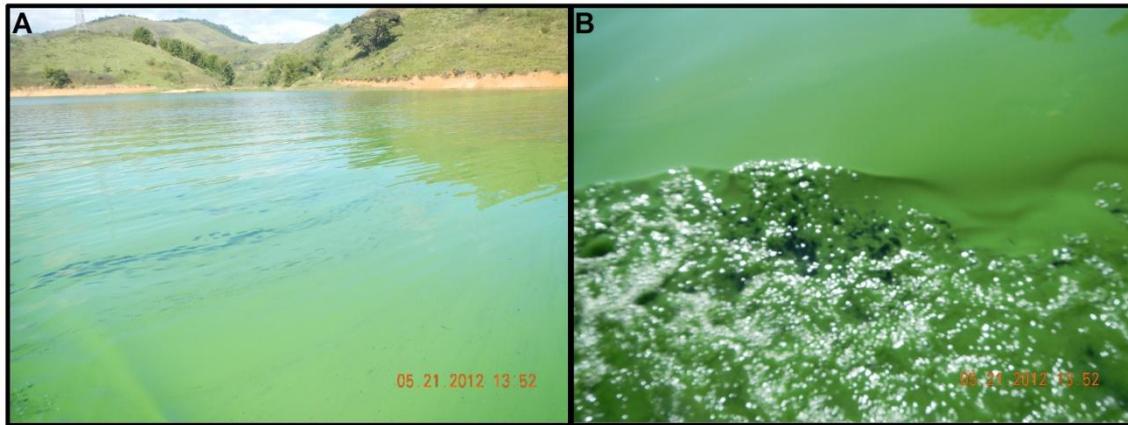
Figure 3.2 - Phytoplankton bloom at Funil Reservoir on May, 2012 (Hydrosphere Processes Research Group/INPE)

Sampling points were distributed along the entrance of Paraíba do Sul River (Figure 3.1) due to be the area of the reservoir with highest levels of eutrophication, because of the input of nutrients and other pollutants in the reservoir through this river.

3.2. Equipment

Several fluorometric, radiometric and spectrometric equipments were used to collect data on the water column and above the surface of the Funil Reservoir. In this section the main equipments are quickly described by their main characteristics.

3.2.1. FluoroProbe

FluoroProbe (bbe-Moldaenke, Kiel, Germany) is an *in situ* fluorometer that uses the spectral fluorescence approach to quantify phytoplankton biomass and to discriminate among 4 different phytoplankton groups (1) 'green' algae (Chlorophyta and Euglenophyta) rich in chl-*a* and *b*, (2) 'brown' xanthophylls containing algae (Bacillariophyta, Chrysophyta and Dinophyta), (3) 'blue' PC-rich algae (Cyanophyta) and (4) 'red' phycoerythrin-rich algae (Cryptophyta) (HOULIEZ, et al., 2012).

For the discrimination of phytoplankton groups, it uses five light emitting diodes (470, 525, 570, 590 and 610 nm) for sequential light excitation of accessory pigments. It also measured the relative fluorescence intensity of chl-*a* between 690 and 710 nm. To quantify the concentration of each phytoplankton group it compares the excitation spectrum to a library of four fingerprints stored in the probe and the relative concentration of each algal group expressed in terms of the equivalent amount of chl-*a* per liter (µg/L) (BEUTLER et al., 2002). The general idea of this procedure is to perform linear regression to estimate the weighting factor to be applied to each estimated spectra, which allows the calculation of the amount of chl-*a* corresponding to each group.

3.2.2. Fluorometer Turner 10-AU

The 10-AU-005-CE Field Fluorometer (Turner Designs, Sunnyvale, CA, USA) is a rugged, field-portable instrument that can be set up for continuous-flow monitoring or discrete sample analysis. The instrument features a watertight case, internal data logging, automatic range changing, and watertight quick-change filter paddles (TURNER DESIGNS, 2009). The 10-AU fluorometer was equipped with a PC Optical Kit (P/N: 10-305) including a cool-white mercury vapor lamp, a 630 nm excitation filter, and a 660-nm emission filter. This optical kit permits the measurement of *in vivo* PC, using the procedure of continuous-flow through a 12V self priming pump which has a flow rate of approximately 23.8 liters per minute (L min^{-1}). The hose for water uptake was set at 30 cm from the surface to minimize the entry of air bubbles in the system (FERREIRA et al. 2012).

3.2.3. RAMSES hyperspectral radiometers

Radiance and irradiance measurements were carried out using the RAMSES hyperspectral radiometers (TriOS GmbH, Oldenburg, Germany). These radiometers take measures in the visible and near-infrared range of the spectrum (320–950 nm) with 3.3 nm spectral resolution (0.3 nm accuracy); and can be used in air or in water. RAMSES radiometers can be classified in ACC-

UV, ACC-VIS, ASC-VIS and ARC (TRIOS, 2013). The RAMSES ACC-UV is an integrated Ultra-Violet (UV) hyperspectral radiometer; and the RAMSES-ACC-VIS is a Ultra-Violet A (UV-A) and visible spectral region hyperspectral radiometer, both equipped with a cosine collector. RAMSES-ASC-VIS is equipped with a spherical collector shielded to measure radiation from one hemisphere. It can measure scalar irradiance through the use of two of these sensors pointed in opposite directions. RAMSES-ARC is a highly integrated hyperspectral radiometer for the UV and visible spectral range. All these radiometers are calibrated for underwater and air measurements using two different calibrations. They capture the signal through some power consumption and portable terminal (laptop) with the MSDA_XE software which is used to record the radiance signal and export the data from the database for further processing. The use of RAMSES sensors is enhanced due to the work of Ohde and Siegel (2003) which used the sensors to calculate its immersion factors of sample radiance and irradiance.

3.2.4. Hydroscatt 6P

HydroScat-6P (Hydro-Optics, Biology, & Instrumentation Laboratories - HOBI Labs, Tucson, AZ, USA) is an instrument for measuring optical backscattering at six different wavelengths (420, 442, 470, 510, 590, and 700 nm) in natural waters. It can also provide measurements of fluorescence at 700 nm excited by 442 nm and at 510 nm excited by 420 nm (HOBI LABS, 2013). The six independent channels are sensitive to different narrow ranges of optical wavelengths. Thus, each channel has a unique source and receiver optics. The source will produce a beam from a light-emitting diode (LED) - selected to match the desired measurement wavelength - which will be emit through a lens to adjust its divergence, then through a prism that bends the beam before it goes to the water. The receiver will collect a portion of the light that is scattered out of that beam through a band-pass interference filter which will determine the exact wavelength range of the measurement from the source beam (HOBI LABS, 2010). The geometry of the position of the source beam, the receiver

field of view, the angles of the prisms, and the distance between the source and receiver windows results in a measurement centered on a scattering angle of 140º MAFFIONE; DANA, 1997). HydroScat-6P also includes a depth transducer, rechargeable batteries, a data logger with real-time clock, and an external switch for controlling logging.

3.2.5. Spectrophotometer

A Perkin Elmer lambda 35 UV/Vis Systems spectrophotometer (Perkin Elmer Inc, Waltham, MA, USA) with an integrating sphere was used to measure absorbance of the samples with 10 cm quartz cells and a spectral range from 190 - 1100 nm.

3.3. Limnological Analysis

3.3.1. Chl-*a* Analysis

Water samples for chl-*a* analysis were collected from the subsurface, approximately 10 cm below the water surface, and were kept at cool temperatures until the inland filtering procedure. This procedure consisted of filtering the collected samples using GF/F filters (Whatman, 0.7 μm pore size) and then extracting the samples from the filters using 90% acetone and measuring the absorbance in a Varian Cary 50 Conc UV-VIS spectrophotometer (Agilent Technologies, Santa Clara, CA, USA) (NUSH, 1980). Concentration of chl-*a* from the spectrophotometric absorbance data was calculated using the equation from Lorenzen (1967).

3.3.2. TSS Analysis

TSS concentrations were determined based on Wetzel and Likens (1991) from water samples filtered through pre-ashed Whatman GF/F glass-fibre filters, dried at 105°C, and weighed to determine the TSS. Filters were dried and weighed and TSS calculated by the difference in weight between the pre and post filtered filters.

3.3.3. PC Analysis

PC concentration was estimated through the use of an *in situ* fluorometer called FluoroProbe (bbe Moldeanke, GmbH) and a fluorometer (Turner Designs, model 10-AU-005) with an *in vivo* PC optical kit which uses the excitation and emission wavelengths at 600 nm and 640 nm, respectively. The fluoroprobe measures temperature and phytoplankton concentrations of four groups: (1) Chlorophyta, (2) PC-rich Cyanobacteria, (3) Diatoms, and (4) Cryptophyta. All data were time stamped and archived on a field handheld personal computer. PC concentration were then estimated by a intercalibration among fluorescence values measure by the fluorometer and concentrations values measure by the Fluoroprobe.

3.3.4. Phytoplankton identification and cell counts

The sample was preserved with Lugol's solution and settled until the delivery in the laboratory at International Institute of Ecology (IIE). The Lugol's solution is recommended for the preservation of the samples since it helps to discharge any gas which could be held in the vacuoles of the organisms; and it is also good since it kills, stains and weighs the algae (LUND et al., 1958). It was used the Utermöhl method since it allows the identification of phytoplankton composition and biomass in an ecosystem (WILLEN, 1976). For the Utermöhl method it was used a chamber, in which a 2 ml sub-sample is placed and left to settle onto a coverslip for two hours to decant the biological material. After this procedure phytoplankton were counted using an inverted microscope (Axiovert 100, Zeiss, Thornwood, NY, USA). Cell counts were given in cells per milliliter (cell/mL).

3.3.5. Microcystins Analysis

Several researches used the enzyme-linked immunosorbent assay (ELISA) for analyze the toxicity of cyanobacterias (CARMICHAEL et al. 2001, AZEVEDO et al. 2002, WANG et al. 2013). Water samples were collected and conserved in

coolers with dry ice packs and transported to the cyanobacteria laboratory at Escola Superior de Agricultura "Luiz de Queiroz" (ESALQ) from the University of São Paulo (USP). Microcystins from the water samples were extracted from the cells by ultrasonicating the samples to release the intracellular toxins. The total of Microcystins concentrations (extracellular and intracellular) were measured using a polyclonal ELISA with a commercial commercial microcystin-LR Beacon kit (Beacon Analytical Systems Inc., USA). The assays of standards or samples were performed following the kit instructions. For each assay, the negative control, calibrators and samples were tested at least in duplicate and the standard calibration curves were drawn using the kit.

3.3.6. Nitrogen and Phosphorus

Total Nitrogen and Total Phosphorus were estimated in laboratory from the water samples from the subsurface. Total nitrogen was estimated by the standard Kjeldahl technique. The Kjeldahl procedure yields a total nitrogen which includes most organic-N compounds and ammonia, but neither nitrate nor nitrite (SMART et al., 1981). The procedure can be broken down into three main steps: digestion, distillation and titration. The first step is used to decompose the nitrogen in organic samples utilizing a concentrated acid solution. It is usually accomplished by boiling a homogeneous sample in concentrated sulfuric acid resulting in an ammonium sulfate solution. The distillation step adds base to the acid digestion mixture to convert ammonium cation (NH_4^+) to ammonia (NH_3), followed by boiling and condensation of the NH_3 gas in a receiving solution. The titration step is used to quantify the amount of ammonia in the receiving solution. The amount of nitrogen in a sample can be calculated from the quantified amount of ammonia ions in the receiving solution (EPA, 1983).

Total Phosphorus quantification requires the conversion of the phosphorus to dissolved orthophosphate. After this conversion it is possible to measure the orthophosphate by colorimetric determination. The most common technique to determine the color of orthophosphate is the ascorbic acid method. In this

method ammonium molybdate and antimony potassium tartrate react in an acid medium with dilute solutions of orthophosphate-phosphorus. This reaction forms an intensely colored antimony-phospho-molybdate complex. Through the addition of ascorbic acid, this complex is reduced to an intensely blue-colored complex which the color intensity is proportional to the phosphorus concentration (EPA, 1983).

3.4. Radiometric Analysis

Six RAMSES sensors were used, two ACC and four ARC sensors, acquiring data simultaneously (Figure 3.3). The two irradiance sensors centered at nominal (excluding effects of wave motion) viewing zenith angle (θ_v) of 90° pointed upward (E_d) and downward (E_u) directions. A radiance sensor was also pointed downward to measure (L_u). These three measures were collected above and below (below the air-water interface, 1m, 2m and 3m) the water surface. On the top of the boat, a radiometer with an optical fiber and cosine diffuser (yielding a hemispherical field of view, FOV), pointed upward to acquire the E_s. The other two radiometers with a 7° FOV were also on the top of the boat and were centered at nominal θ_v of 40° in two different directions: upward for the L_s and downward direction for the radiance L_w.
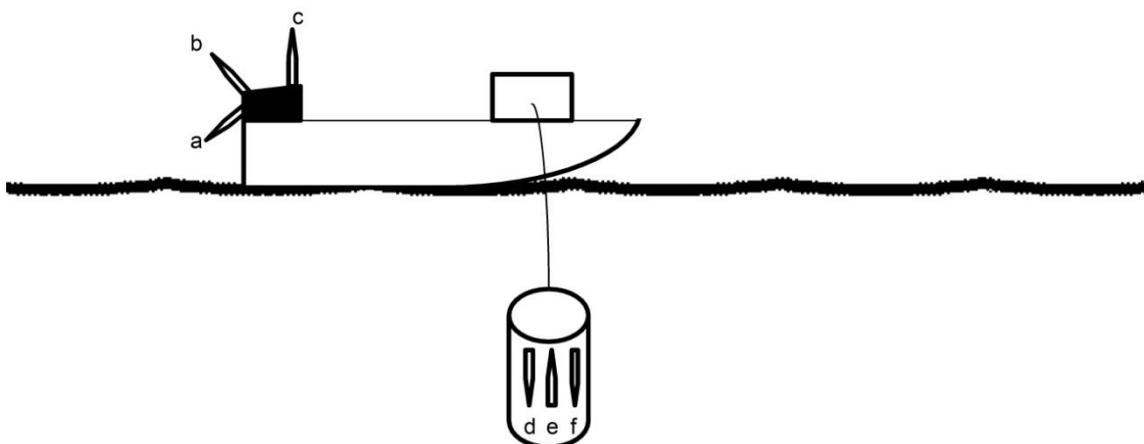
Figure 3.3 - Radiometric scheme for data acquisition; a) L_w; b) L_s; c) E_s; d) E_u; e) E_d; and f) L_u.

R_{rs} was calculated according equation 3.1 (MOBLEY, 1999):

$$R_{rs}(\lambda) = \frac{tL_u(\lambda)}{n^2 E_d(\lambda)} F_i(\lambda) \qquad (3.1)$$

Where, t is the transmittance at the air-water interface (0.98); n is the refractive index of water (1.34); and $F_i(\lambda)$ is the spectral immersion coefficient (OHDE; SIEGEL, 2003). The spectral immersion coefficient for each sensor was derived by following Equation 3.2

$$F_i(\lambda) = \frac{n_w(\lambda)(n_w(\lambda) + n_g(\lambda))^2}{(1 - n_g(\lambda))^2} \qquad (3.2)$$

where, n_w is the wavelength-dependent refractive index of freshwater and can be estimated using Equation 3.3 (AUSTIN; HALIKAS, 1976). n_g is the corresponding index of the glass window of the radiance sensor.

$$n_w(\lambda) = 1.325147 + \frac{6.6096}{\lambda - 137.1924} \qquad (3.3)$$

The r_{rs} was calculated according to equation 3.4 (MOBLEY, 1999; KIRK, 2011).

$$r_{rs}(\lambda) = \frac{L_u(\theta, \phi, \lambda)}{E_d(\lambda)} \qquad (3.4)$$

where θ and ϕ are the specify the polar and azimuthal directions respectively.

As described by Mishra et al. (2005), changes in sun illumination condition may cause variations in E_s. Thus, in order to normalize the radiometric measurements we adapt Mueller (2000) method to quantify the variation in the obtained E_d spectra using simultaneously acquired E_s measures as showed on Figure 3.3. The methodology calculates a normalization factor which can be estimated by equation 3.5.

$$NF = \frac{E_s(t(z_1), \lambda)}{E_s(t(z_m), \lambda)} \qquad (3.5)$$

where, $E_s(t(z_m),\lambda)$ is the E_s measured at time $t(z_1)$ on the top of the boat at the first scan, and $t(z_m)$ the E_s measured the top of the boat at the m scan.

Absorption coefficients such as a_p, a_{phy}, a_{nap} and a_{CDOM} were measured at Aquarela Laboratory from the Center of Marine Biology of University of São Paulo (CEBIMar/USP). For the a_{cdom}, the water samples from the field campaign were temporarily stored in a cooled chamber and filtered through 0.2 µm pore size nylon filters. To retrieve the CDOM absorption coefficient of the water samples, the beam attenuation of the filtered water was measured with a Lambda 35 UV/Vis Systems equipment in a transparent cuvette with Millipore Milli-Q water in the reference cell. As the data from the equipment are noisy the exponential shape of the a_{CDOM} was fitted based on the 250–800 nm wavelength range.

The specific absorption spectra of non-algae particles and phytoplankton were measured using the filter pad method using Perkin Elmer integrating sphere attached to an Perkin Elmer Lambda 35 UV/Vis Systems spectrophotometer following the methods described by Tassan and Ferrari (1995). Briefly the method consisted on the determination of a_p from water samples that were filtered under low pressure through a 25 mm GF/F Whatman filter. a_p in the range 390 - 800 nm was determined in the spectrophotometer. Samples were then de-pigmented by soaking the filters in a 1% solution of sodium hypochlorite (NaClO). The values of a_{nap} were then measured as described above and a_{phy} values were calculated from equation 3.6.

$$a_{phy} = a_p - a_{nap} \qquad\qquad (3.6)$$

3.5. PC estimation validation

PC concentrations from the fluorescence excitation methods were compared to a PC analytical method proposed by Mishra et al. (2013). This comparison was realized using the mix dataset proposed by Ogashawara et al. (2013) and two PC band ratio algorithms. This comparison is based on the fact that the

specular reflection from water under wavy conditions that generally gets suppressed in a band ratio algorithms (VINCENT et al., 2004). Thus, the band ratio values would be comparable for different geographical regions.

It was chosen the nested band ratio algorithm (SIMIS et al., 2005) and the new single reflectance ratio (MISHRA et al., 2009) for the comparison between fluorescence excitation and analytical methods. Derived values from these two band ratio algorithms were compared to PC estimations. This approach will analyze de number of trends in these values. If the PC estimations were compatible it will only show one trend, otherwise it will not be compatible.

3.6.   Semi-empirical bio-optical models comparison

Three sets of calibration and validations were performed including one on Funil Reservoir's data, one on Catfish Pond's data, and the third on a mixed dataset Figure 3.4. As the Funil Reservoir and Catfish pond datasets have significantly different concentration range (Table 3.1), a third dataset was created by mixing the two and then randomly dividing into two datasets, one to be used for calibration (60%) and the other for validation (40%). Models were calibrated using the hyperspectral R_{rs} (Figure 3.4) and the formulas listed in Table 3.2. For each model and each dataset, a linear calibration curve was set between the model values and the PC concentration. We did not use the best fit function, which were mainly non-linear functions, to avoid an out of range calibration/validation problem because the range of PC concentration in both datasets was extreme without any overlap (Table 3.1).

Table 3.1 - Summary statistics for chl-a and PC pigment concentrations at study sites

		Funil Reservoir	Catfish Ponds
Surface Area (km^2)		40	0.004-0.03
Mean depth (m)		20	1.1
Time frame of field campaigns (years)		2013	2010-2011
Total samples		16	23
Chl-a (µg/L)	Maximum	52.78	831.35
	Minimum	4.92	59.79
	Range	47.86	771.56
	Average	19.49	230.2
	Standard Deviation	14.79	176.16
PC (µg/L)	Maximum	35.95	857.08
	Minimum	9.16	68.13
	Range	26.79	788.95
	Average	14.52	241.51
	Standard Deviation	7.70	215.72
Total Nitrogen (µg/L)	Maximum	1620	8000 (Mishra, 2012)
	Minimum	100	4000 (Mishra, 2012)
Total Phosphorus (µg/L)	Maximum	37.77	500 (Mishra, 2012)
	Minimum	16.46	800 (Mishra, 2012)
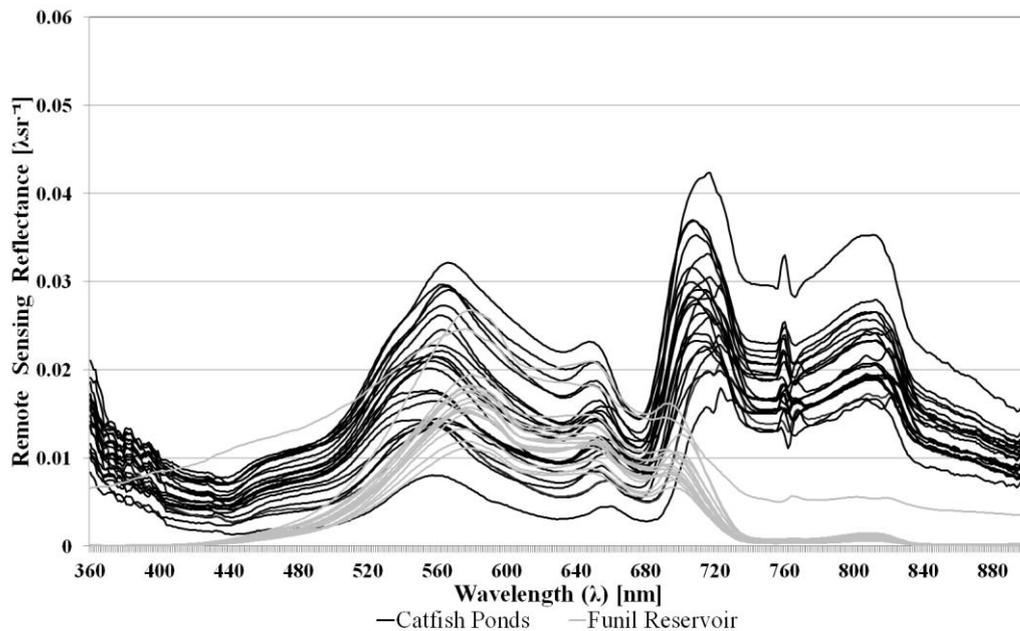
Figure 3.4 - Remote sensing reflectance for both study sites

Table 3.2 - Summary of R_{rs} based bio-optical models used in our study for predicting PC concentration.

Name	Reference	Model
DE93	Dekker (1993)	$PC \propto \left[\left(R_{rs}(600) + R_{rs}(648) \right) - R_{rs}(624) \right]$
SC00	Schalles & Yacobi (2000)	$PC \propto R_{rs}(650)/R_{rs}(625)$
SI05	Simis et al. (2005)*	$PC \propto R_{rs}(709)/R_{rs}(620)$
MI09	Mishra et al. (2009)	$PC \propto R_{rs}(700)/R_{rs}(600)$
SM12	Mishra (2012)	$PC \propto R_{rs}(709)/R_{rs}(600)$
MM09	Modified Mishra et al. (2009)**	$PC \propto R_{rs}(724)/R_{rs}(600)$
HU10	Hunter et al. (2010)	$PC \propto \left[\left(R_{rs}^{-1}(615) - R_{rs}^{-1}(600) \right) \cdot R_{rs}(725) \right]$

Notes:* Ratio has been adopted from Simis et al. (2005) in their nested semi-analytical algorithm.** MM09 is the slightly modified version of MI09

A cross-validation procedure was adopted, if any, by developing linear calibration using one dataset and validating with the two remaining datasets. (Table 3.3). Validations were analyzed by plotting PC Measured versus PC Predicted.

Table 3.3 - Summary of calibration and validation datasets used in the study

Calibration	Validation
Mixed dataset (n=23)	Catfish Ponds
	Funil Reservoir
	Mixed dataset (n=16)
Funil Reservoir	Catfish Ponds
	Mixed dataset (n=16)
Catfish Ponds	Funil Reservoir
	Mixed dataset (n=16)

Error analysis was performed by comparing measured and predicted PC concentrations. Bias, Mean Square Error (MSE), Mean Absolute Error (MAE), Root Mean Square Error (RMSE), and Normalized Root Mean Square Error (NRMSE) were used to evaluate model performance and were calculated according to Table 3.4.

Table 3.4 - Summary of error estimators used in our study

Estimator	Formulas
Bias	$Bias = \dfrac{1}{n}\sum_{i=1}^{n}(y_i - x_i)$
MAE	$MAE = \dfrac{1}{n}\sum_{i=1}^{n}|y_i - x_i|$
MSE	$MSE = \dfrac{1}{n}\sum_{i=1}^{n}(y_i - x_i)^2$
RMSE	$RMSE = \sqrt{MSE}$
NRMSE	$NRMSE = \dfrac{RMSE}{y_{i,max} - y_{i,min}}$

Note: where, y_i and x_i are the measured and predicted parameter concentration in i^{th} sample; $y_{i,max}$ and $y_{i,min}$ are the maximum and minimum measure parameter concentration.

Sensitivity analysis was carried out for the models with the lowest errors and the best validation plots for the hyperspectral dataset. This analysis was performed to study chl-*a* interference on the aforementioned PC detection algorithms. The sensitivity analysis was conducted using the values derived from PC detection algorithms (Table 3.2), chl-*a*, and PC concentrations. Surface plots were generated using these three parameters (model values, PC and chl-*a* concentration). They were analyzed according to the slope in each axes and the color scale of the surface which represents the PC detection algorithms.

3.7.   QAA development

To evaluate the need to re-parameterize a QAA for Funil Reservoir, we applied QAAv5 (LEE et al., 2009) and QAA for highly turbid waters (MISHRA et al., 2014) to Funil's dataset. IOPs estimations from these two QAAs were validated with errors estimators (Table 3.4) using measured absorptions coefficients. The evaluation was based not only on the values of the errors estimators, but also in

the shape and intensity of spectra (measure and estimated spectral absorption coefficient).

After analyzing the results from these two QAAs we noticed the QAA steps which should be re-parameterized and a modified QAA method was proposed. The proposed QAA (pQAA) was also validated with errors estimators calculate between measured and estimated absorptions coefficients.

3.8. PC estimation

To estimate PC from the derived IOPs it was used the relation proposed by Mishra et al. (2013) where the $a_{phy}(\lambda)$ is used to retrieve PC absorption at 620 nm. Since $a_{phy}(\lambda)$ provides information about the absorption by all intracellular phytoplankton pigments, at 620 nm the value of $a_{phy}(620)$ should be equal to the sum of chl-*a* and PC contributions (SIMIS et al., 2005). Thus, the authors also considered that at 665 nm $a_{phy}(\lambda)$ is dominated by chl-*a* and develop the following relation:

$$a_{PC}(620) = \frac{\psi_1 a_{ph}(620) - a_{ph}(665)}{\psi_1 - \psi_2}$$ (3.7)

where: ψ_1 and ψ_2 corresponds to $a_{chl}(665)/a_{chl}(620)$ and $a_{PC}(665)/a_{PC}(620)$, respectively.

To calculate the values of ψ_1 and ψ_2 we used the empirical relationship proposed by Mishra et al. (2013) which compared ψ_1 measured in vitro and the band ratio $r_{rs}(560)/r_{rs}(665)$; and the ψ_2 measured in vitro and another band ratio $r_{rs}(620)/r_{rs}(665)$.

We also use the calibrations, proposed by the authors, which were described in equations 3.8 and 3.9.

$$\psi_1 = 2.867 \ln\left(\frac{r_{rs}(560)}{r_{rs}(665)}\right) + 2.214$$ (3.8)

$$\psi_2 = 0.254 \left(\frac{r_{rs}(620)}{r_{rs}(665)}\right)^{2.219} \tag{3.9}$$

Therefore PC concentration was estimated as described on section 2.3.3. For this we considered $a_{PC}^*(620)$ as a constant value equals to 0.0019.

3.9. OLCI/Sentinel 3 simulation

To apply the pQAA to a synthetic dataset of R_{rs} of OLCI sensor, it was used the hyperspectral R_{rs} measurements from proximal remote sensing which were integrated using OLCI' spectral response function, shown on Figure 3.5

The pQAA was adapted to OLCI spectral bands and IOPs were estimated from the synthetic dataset. Errors estimators were calculated using estimated IOPs and measured IOPs also integrated using OLCI' spectral response function. Thus, PC concentration was also estimated for the synthetic OLCI dataset following the methods described on section 3.8.
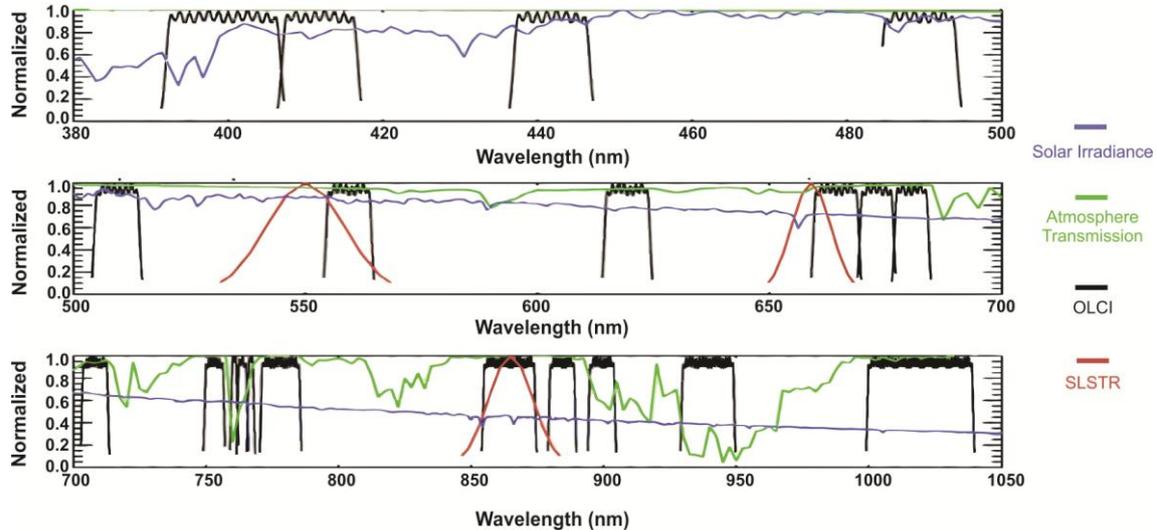
Figure 3.5 - Spectral response function for OLCI and Sea and Land Surface Temperature Radiometer (SLSTR)

Source: Adapted from IOCCG (2010).

3.10. Summary

A summary of the methodology used in this study is shown on Figure 3.6. It starts with the datasets used (from Funil and Catfish ponds) and all the products derived from them.
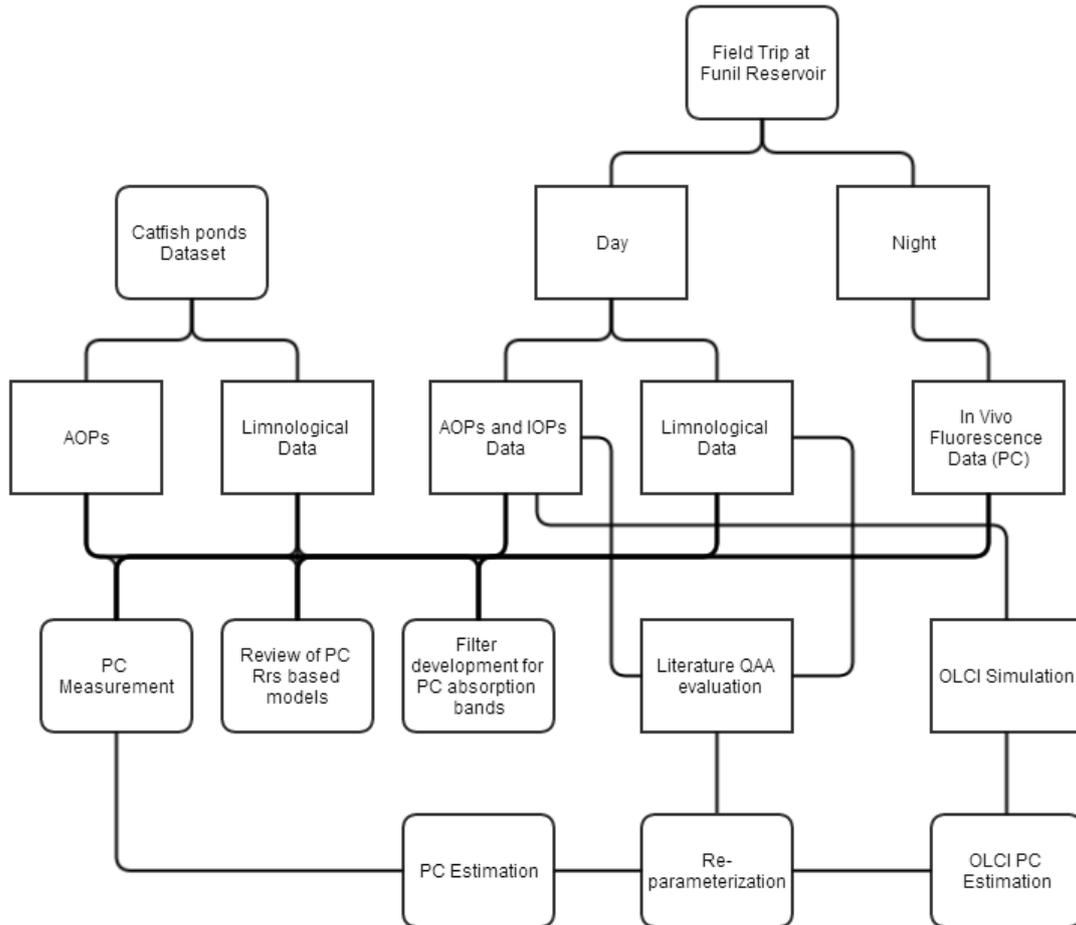
Figure 3.6 - Flowchart of the methodology used in this study

4 RESULTS AND DISCUSSION

4.1. PC measurement (fluorometry)

As described on section 3.5, Simis et al. (2005) and Mishra et al. (2009) band ratios for PC estimation (see Table 3.2) were used to evaluate the accuracy of fluorimetric estimation of PC using the two fluorometers mentioned on section 3.2 (Fluoroprobe and 10-AU). To validate the use of fluorometers, it was used the PC concentration estimation used in Mishra et al. (2013, 2014) which was based on Sarada et al. (1999) sonicator method and Bennett and Bogorad (1973) equation.

Therefore, if the PC concentration from both methods were similar, the values of band ratios against the PC concentration should follow a similar trend. Figure 4.1 shows a scatter plot in which it is possible to observe the relation between PC and SI05 band ratio values through the mixed dataset used by Ogashawara et al. 2013. This dataset was composed of field data collected at two study sites: the first study site was Funil Reservoir located in Itatiaia, RJ, Brazil during 2–5 April 2013, and the second dataset was collected from catfish aquaculture ponds located at the Thad Cochran National Warmwater Aquaculture Center, Stoneville, MS, USA during 13–16 July 2010 and 28–29 April 2011 (OGASHAWARA et al., 2013).

Table 4.1 shows the regression analysis between SI05 and PC concentration from the mixed dataset. It was tested 4 regressions: Linear, Exponential, Logarithmic and Geometric. Regression analysis showed that geometric regression for the mixed dataset got a R^2 of 0.9437, and for exponential regression a R^2 of 0.9291. Therefore it seems that there is an exponential trend between the SI05 values and PC concentrations calculated from both methods. Thus, the use of fluorometers to calculate PC concentration was well validated by PC concentration estimated by Sarada et al. (1999) method.
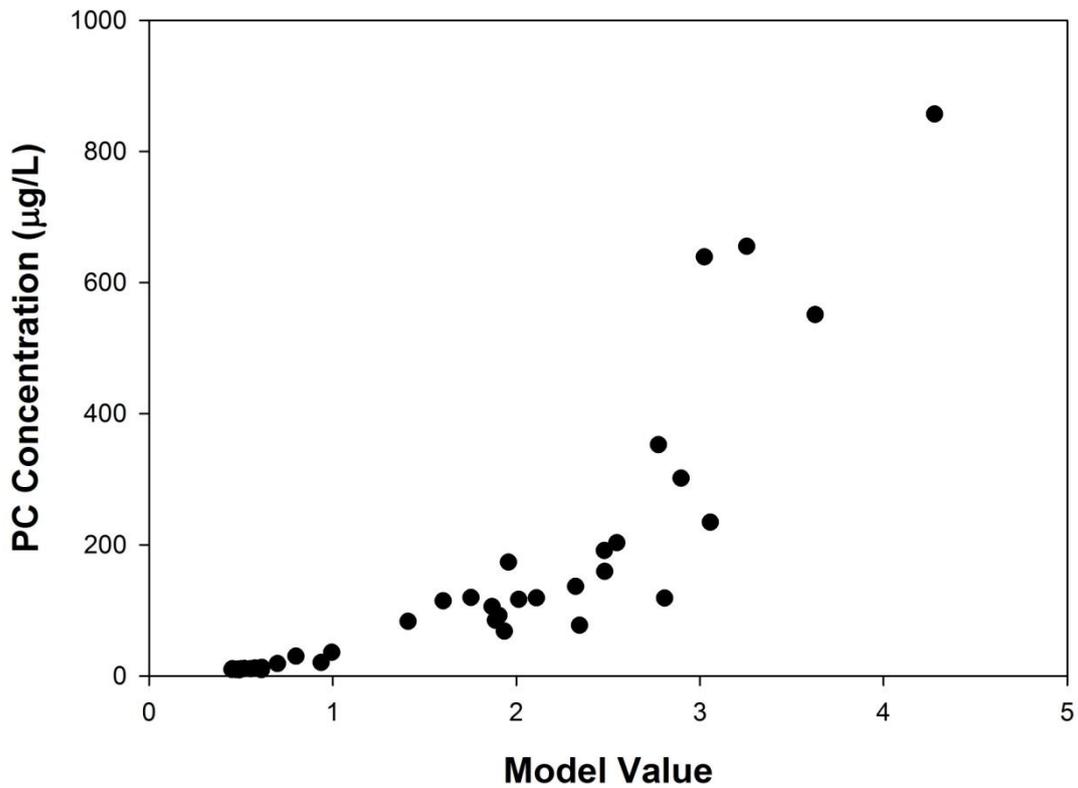
Figure 4.1 - Scatter plot of SI05 band ratio and PC concentration from datasets

Table 4.1 - Regression values of SI05 and PC concentration from both methods

Regression	Linear	Exponential	Logarithmic	Geometric
n	39	39	39	39
a	-120.9312	6.74	93.1013	35.7998
b	159.2299	1.3038	194.108	1.8797
R^2	70.44%	92.91%	51.16%	94.37%
Equation	Y' = a + bX	Y' = a * e^(bX)	Y' = a + b * ln(X)	Y' = a * X^b
p-value	p <0.00001	p <0.00001	p <0.00001	0.0001

Figure 4.2 shows a scatter plot in which it is possible to observe the relation between PC and MI09 band ratio values through the mixed dataset. The scatter plot also shows a unique trend which could be quantified at Table 4.2.
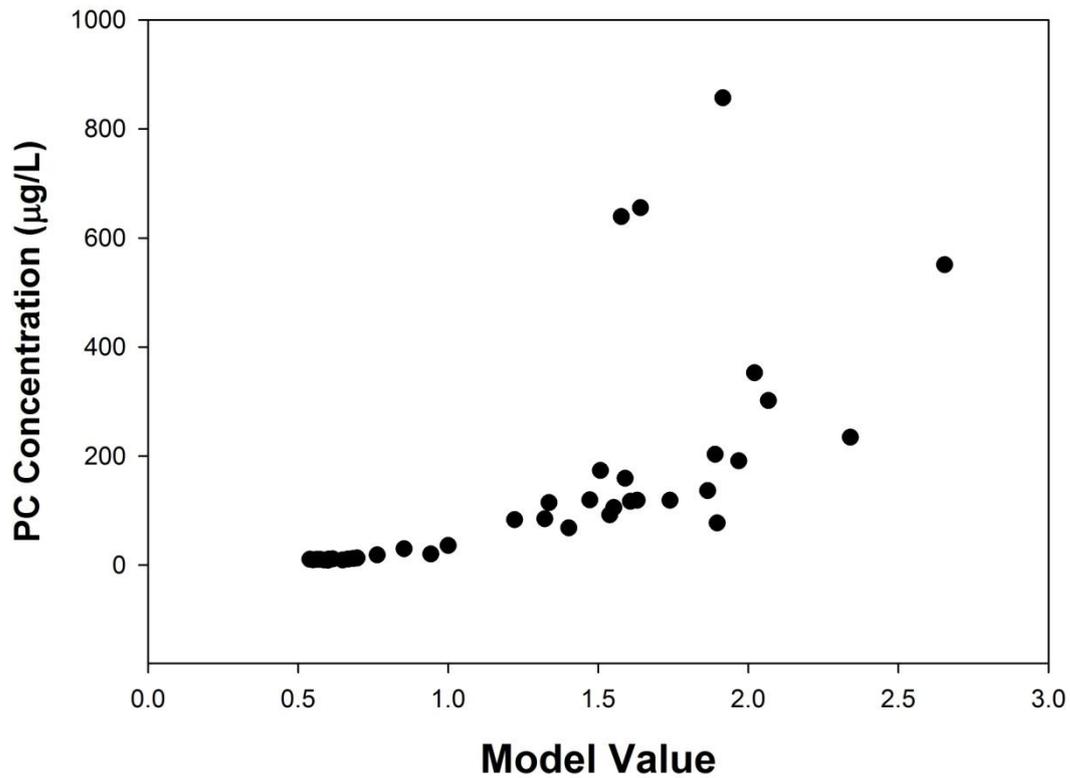
Figure 4.2 - Scatter plot of MI09 band ratio and PC concentration from datasets

Table 4.2 shows the regression analysis between MI09 and PC concentration from the mixed dataset. The regression analysis showed that geometric regression was also better for MI09 which got a R^2 of 0.9546, and for exponential regression a R^2 of 0.9235. However, MI09 got better R^2 values for linear and logarithmic regressions if compared to SI05. The more correlated performance between PC concentration and MI09 values was also described by Mishra et al. (2009) and Ogashawara et al. (2013). Both studies considered that the use of 600 nm as the PC absorption feature on MI09, is the key to improve the accuracy of the model, since the influence of chl-*a* at 600 nm is lower than in 620 nm (MISHRA et al, 2009). Therefore, according to MI09, the use of fluorometers to estimate PC concentration was also comparable to estimation through the sonicator method (SARADA et al., 1999). It was observed three outliers with concentrations over 600 µg/L of PC. They were considered outliers because of their position on the plot and also because of their very high

concentrations, which is not common. Therefore, R^2 could be enhanced by the elimination of them.

Table 4.2 - Regression values of MI09 and PC concentration from both methods

Regression	Linear	Exponential	Logarithmic	Geometric
n	36	36	36	36
a	-113.3599	3.5457	79.8781	37.3615
b	169.5896	2.0912	183.8216	2.5098
R^2	75.90%	92.35%	63.99%	95.46%
Equation	Y' = a + bX	Y' = a * e^(bX)	Y' = a + b * ln(X)	Y' = a * X^b
(p)	p <0.00001	p <0.00001	p <0.00001	0.0002

4.2. Overview of the dataset

4.2.1. Limnological dataset

Data of microsystins (MC) concentration (μg/L), PC concentration (μg/L), Total Nitrogen (TN) concentration (μg/L), Total Phosphorus (TP) concentration (μg/L), chl-*a* concentration (μg/L), and cyanobacteria cell count (BG) (cell/mL) datasets are shown on Figure 4.3 which shows the box plots of each limnological variable. Phytoplankton classification showed that the primary specie in the Funil Reservoir is the *Microcystis aeruginosa* which is a cyanobacteria that can produce microcystins. A studied conducted by the World Health Organization (WHO, 2003) has established a provisional guideline of 1 μg/L for microcystin-LR for waters of human exposure. Therefore, Figure 4.3 also shows that Funil Reservoir's waters are for some sampling points over WHO's MC concentration limits for human health.

Hunter et al. (2010) found that the relationship between the cell counts of cyanobacterial and MCs concentration was weak and marginally non-significant (R^2=0.251;p=0.057). The same relationship was found in the Funil Reservoir dataset with a R^2 of 0.13 and p-value of 0.003. These low relationships founded

in both datasets can be partly explained by the fact that MC production is not only related to the presence of cyanobacteria, but also influenced by nutrient supply and environmental conditions (HUNTER et al., 2010).
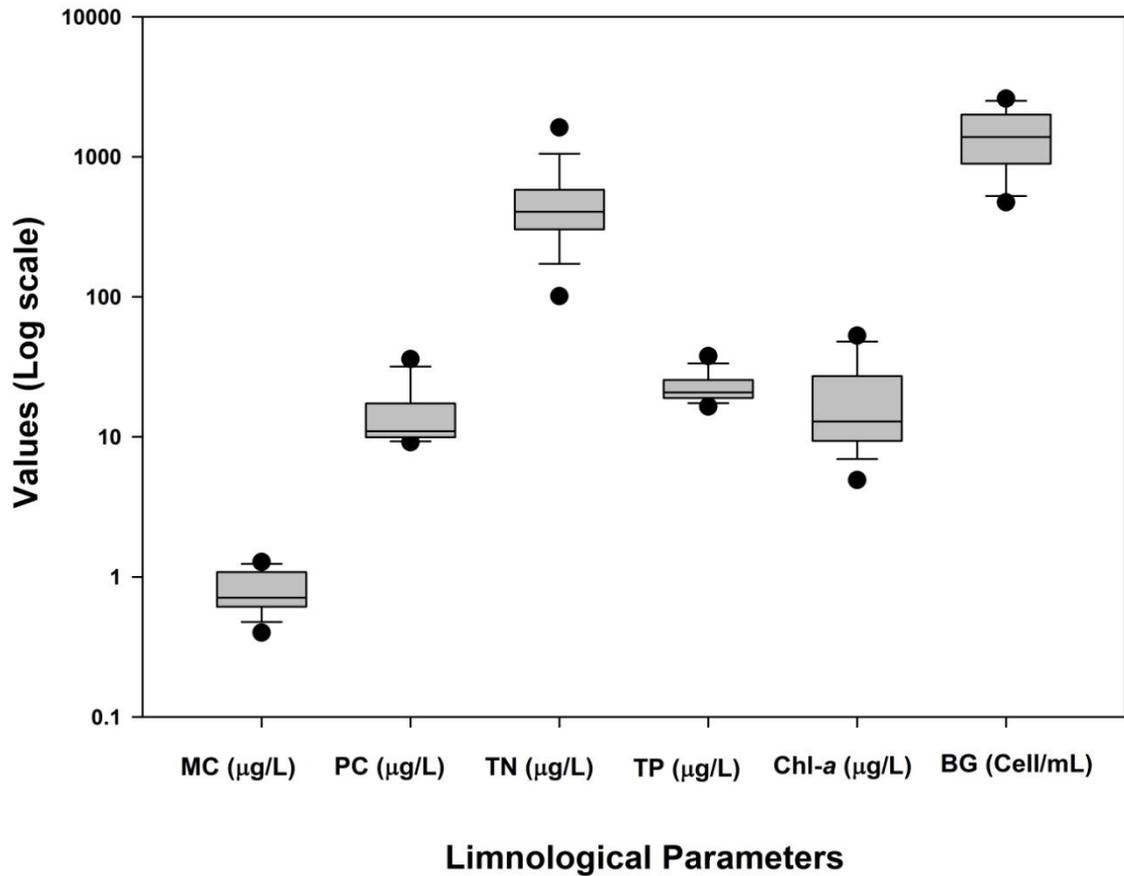
Figure 4.3 - Box plots of limnological parameters collected at Funil Reservoir

Although the weak relationship between MC and cyanobacteria cell count, Hunter et al. (2010) stated that the accessory phycobiliproteins and MCs respond in similar ways to variations in resource supply. Following that statement, they were able to produce very strongly correlation between MC and PC (R^2=0.896; p=<0.001). Figure 4.4a shows the relationship between cyanobacteria cell count and an expression using the TN and TP ratio and chl-*a;* while Figure 4.4b shows the relation between PC and MC. The first

relationship produced a linear R^2 of 0.71 and p-value of <0.001; while the second produced a R^2 of 0.62 and a p-value of <0.001. As well as observed by Hunter et al, (2010) the relations using chl-*a* concentrations were less strongly correlated with MC concentrations (R^2=0.30; p=0.026). Thus, the estimation of PC in inland water is important because of its existence on cyanobacteria cells which might provide a crude measure of MC content.
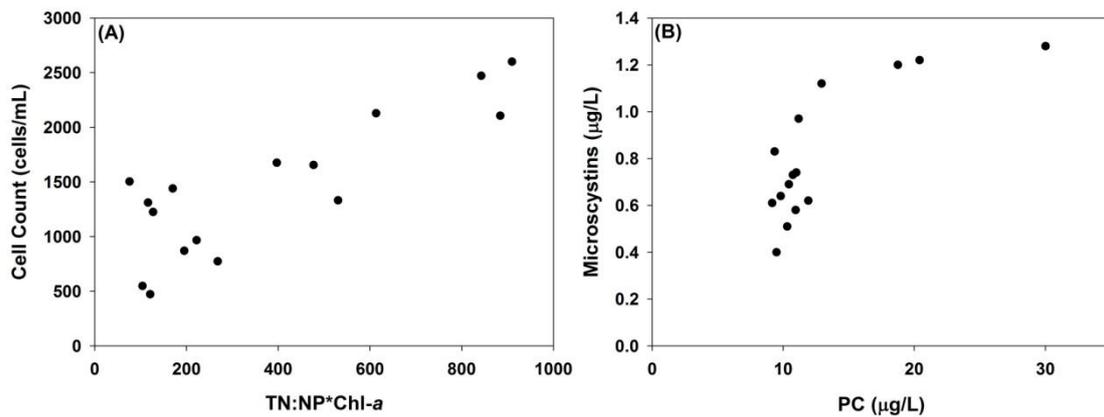
Figure 4.4 - Relationships between limnological parameters; a) Cell count x N:P*Chl-*a*; b) MC x PC

4.2.2. IOPs and AOPs dataset

R_{rs} calculated from equation 3.1 is shown on Figure 4.5a and from the spectra it is clearly visible two absorption features: one around 620 nm and the second around 665 nm. It is also easy to identify the shoulder around 650 nm, which have been described as PC fluorescence which is enhanced by the two absorptions troughs already described. The same explanation could be use for the reflectance peak around 700 nm, not only it is the reflectance of chl-a but it is also enhanced by two absorptions troughs (chl-*a* at 665 nm and water in the NIR region). Figure 4.5b shows the a_{CDOM} spectra for the Funil Reservoir. The spectra seemed similar to other a_{CDOM} spectra from literature, following the typical shape with high absorption coefficients in the blue and green spectral channels and a decay in the large wavelengths. Figure 4.5c shows the spectral

$a_\text{phy;}$ in which it was observed not only a high absorption peak around 665 nm but also a short peak around 620 nm because of PC absorption range. Figure 4.5d shows the a_NAP spectra for Funil Reservoir in the range from 400 to 800 nm. As described in the literature the a_NAP spectra follows the same shape of a_CDOM enhancing the idea that blue and green spectral regions are influenced by these two components.
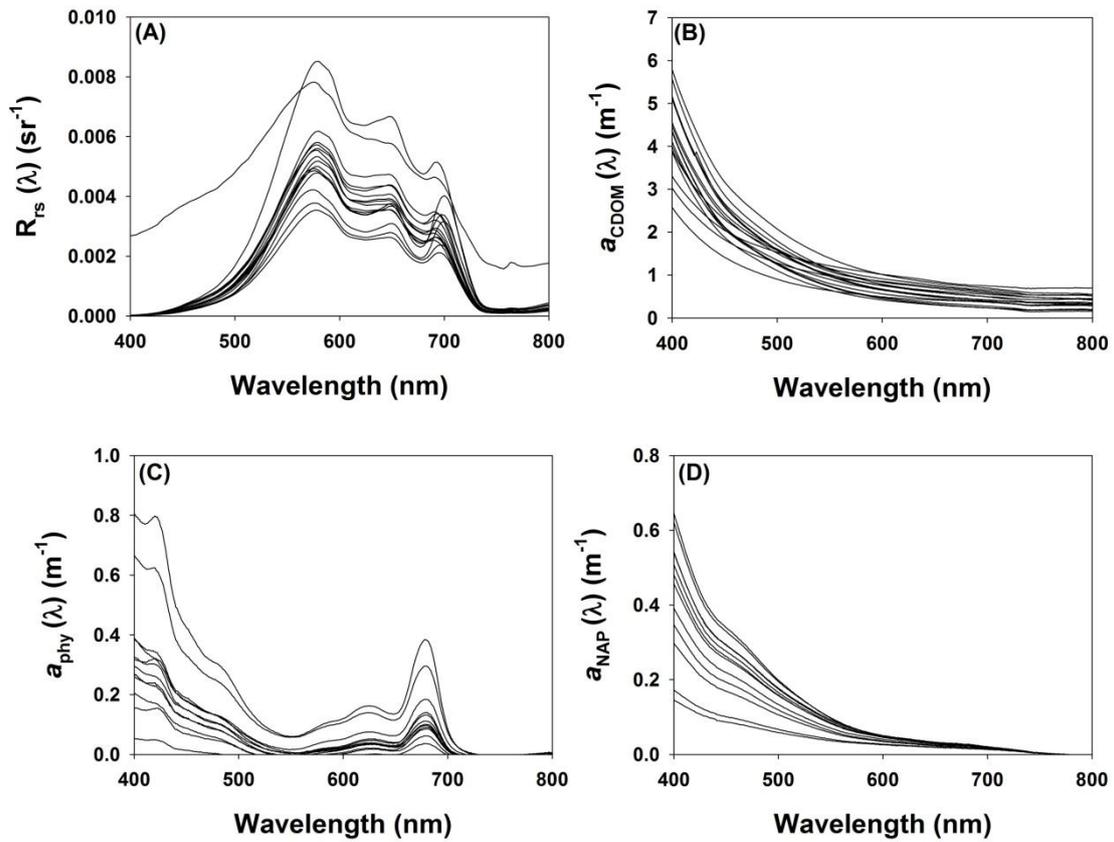
Figure 4.5 - AOP and IOPs for Funil dataset; a) $R_{rs}(\lambda)$; b) $a_{CDOM}(\lambda)$; c) $a_{phy}(\lambda)$; d) $a_{NAP}(\lambda)$

4.3. Semi-empirical bio-optical models comparison

4.3.1. Bio-optical comparison

To analyze the relationship between PC concentrations and several bio-optical models (see Table 3.2), we used three datasets to calibrate the models. We used a modification of MI09 proposed by Mishra (2012) referred to as SM12.

SM12 targeted PC absorption at 600 nm and used the reflectance peak at 709 nm. We also proposed a modification of MI09 using the reflectance peak at 724 nm which is referred to as MM09. Models were calculated from the R_{rs} spectra from both study sites (Figure 3.4). All seven models were calibrated using a linear trend between model values and measured PC concentrations. Funil dataset calibration showed the best result with SM12 (R^2= 0.909). For catfish ponds dataset, the best R^2 was found with SI05 (R^2= 0.748). The mixed dataset showed the lowest R^2 among all during model calibrations and its best result was found with SI05 (R^2= 0.684) (Table 4.3). These models presented similar results for the Adjusted R^2 confirming consistency in their performance. Calibration analysis also showed the slope (X1) and p-value for each model. DE93 and SC00 showed the highest values for slope in all the datasets. Although HU10 showed low values for its slope in the three datasets, it showed high p-values for Funil (0.179) and Catfish ponds (0.261) datasets. One of the reasons behind the poor calibration results observed for DE93 and HU10 could be the specular reflection from water under wavy condition that generally get suppressed in a band ratio algorithm did not get cancelled out due to the band architecture of these two algorithms (VINCENT, et al., 2004). The specular reflection occurs mainly due to the wind which generates waves controlling the brightness of most water pixels. Funil Reservoir is more vulnerable to wind compared to catfish ponds and the combinations of single bands used in DE93 and HU10 were not able to suppress the brightness variations due to wave disturbances. Another reason could be the choice of spectral bands used in both algorithms, since DE93 have more influence from the 648nm band which is contaminated by chl-*a* (MISHRA et al., 2009) and HU10 is mainly influenced by 724nm band which is a chl-*a* reflectance peak. For accuracy assessment, models were validated by applying the linear regression equations to the other datasets (Figures 4.6a and b, 4.7a and b, and 4.8a and b). The scatter plots show the estimated PC versus the measured PC concentration. Although some models produced very high R^2 during the calibration with one dataset, they did not perform well on other datasets. For example, SM12 which produced the

highest R^2 (0.909) during calibration, showed that it is not good estimator for PC concentration during validation. The poor validation results could be due to the difference in the range of PC concentration at two study sites. However, the use of the mixed dataset calibration improved the validation for Funil and catfish datasets (Figure 4.7a,b and 4.8a,b).

Table 4.3 Correlation estimators derived from model calibrations using the three datasets for all seven models

Model	R^2	Adj. R^2	X1	p-value
		Funil Dataset		
DE93	0.088	0.023	-664.535	0.2654
SC00	0.745	0.727	181.122	> 0.0001
SI05	0.793	0.779	41.196	> 0.0001
MI09	0.807	0.794	50.836	> 0.0001
SM12	0.909	0.902	35.638	> 0.0001
MM09	0.414	0.372	62.656	0.0072
HU10	0.125	0.062	-3.841	0.1798
		Catfish Ponds Dataset		
DE93	0.617	0.599	1381.323	> 0.0001
SC00	0.338	0.306	1622.554	0.0036
SI05	0.748	0.736	274.873	> 0.0001
MI09	0.170	0.131	268.015	0.0504
SM12	0.591	0.572	344.990	> 0.0001
MM09	0.731	0.718	270.868	> 0.0001
HU10	0.060	0.015	-12.285	0.2611
		Mixed Dataset		
DE93	0.051	0.006	5966.595	0.3016
SC00	0.518	0.495	1303.031	0.0001
SI05	0.684	0.669	132.365	> 0.0001
MI09	0.547	0.525	198.107	0.0001
SM12	0.640	0.623	155.970	> 0.0001
MM09	0.673	0.658	136.692	> 0.0001
HU10	0.466	0.441	-13.919	0.0003
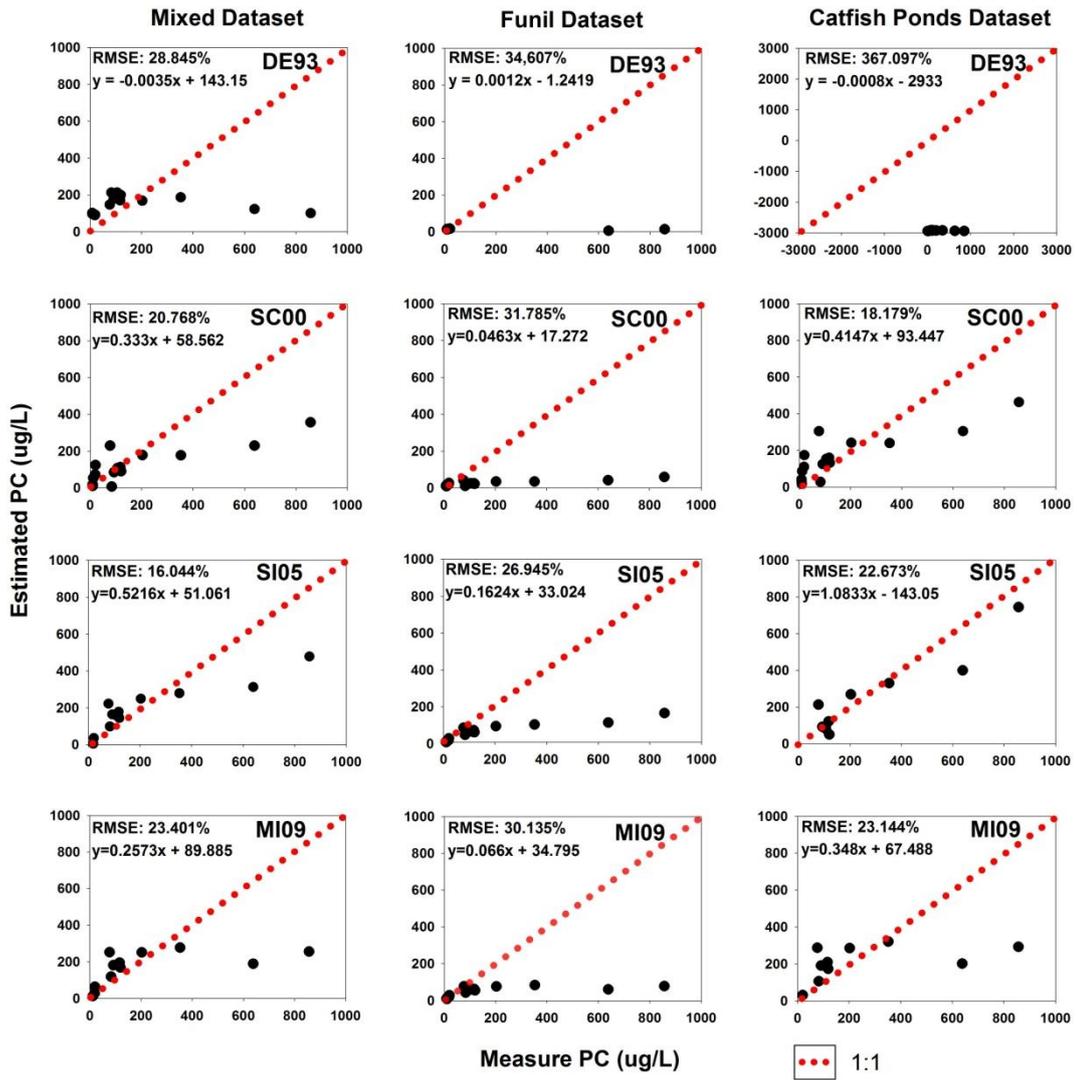
Figure 4.6a - Validation of the models (DE03, SC00, SI05 and MI09) in the mixed dataset using calibrations from (1) Mixed dataset, (2) Funil Reservoir dataset, and (3) Catfish Ponds dataset

58
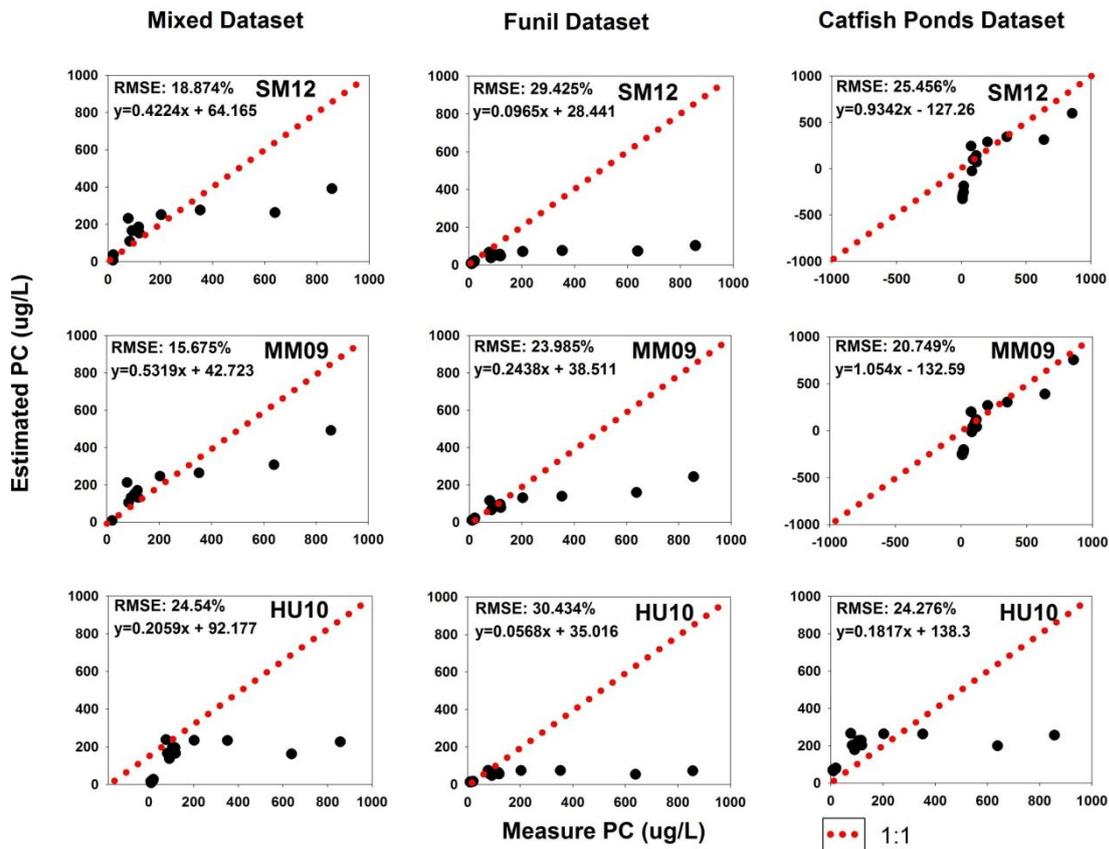
Figure 4.6b - Validation of the models (SM12, MM09, and HU10) in the mixed dataset using calibrations from (1) Mixed dataset, (2) Funil Reservoir dataset, and (3) Catfish Ponds dataset

Validations for Funil Reservoir dataset used two calibrations: the Mixed and catfish ponds calibrations (Figure 4.7a and b). The mixed dataset calibration showed a poor accuracy for all the models tested. The catfish ponds calibrations also performed very poorly on Funil's dataset; however, HU10 produced the lowest value for the slope and showed a linear behavior. The poor performance of the bio optical models is due to the fact that linear models were chosen for the individual calibrations with Funil and catfish ponds data instead of the best-fit models, which are clearly non-linear mainly at high PC concentrations.
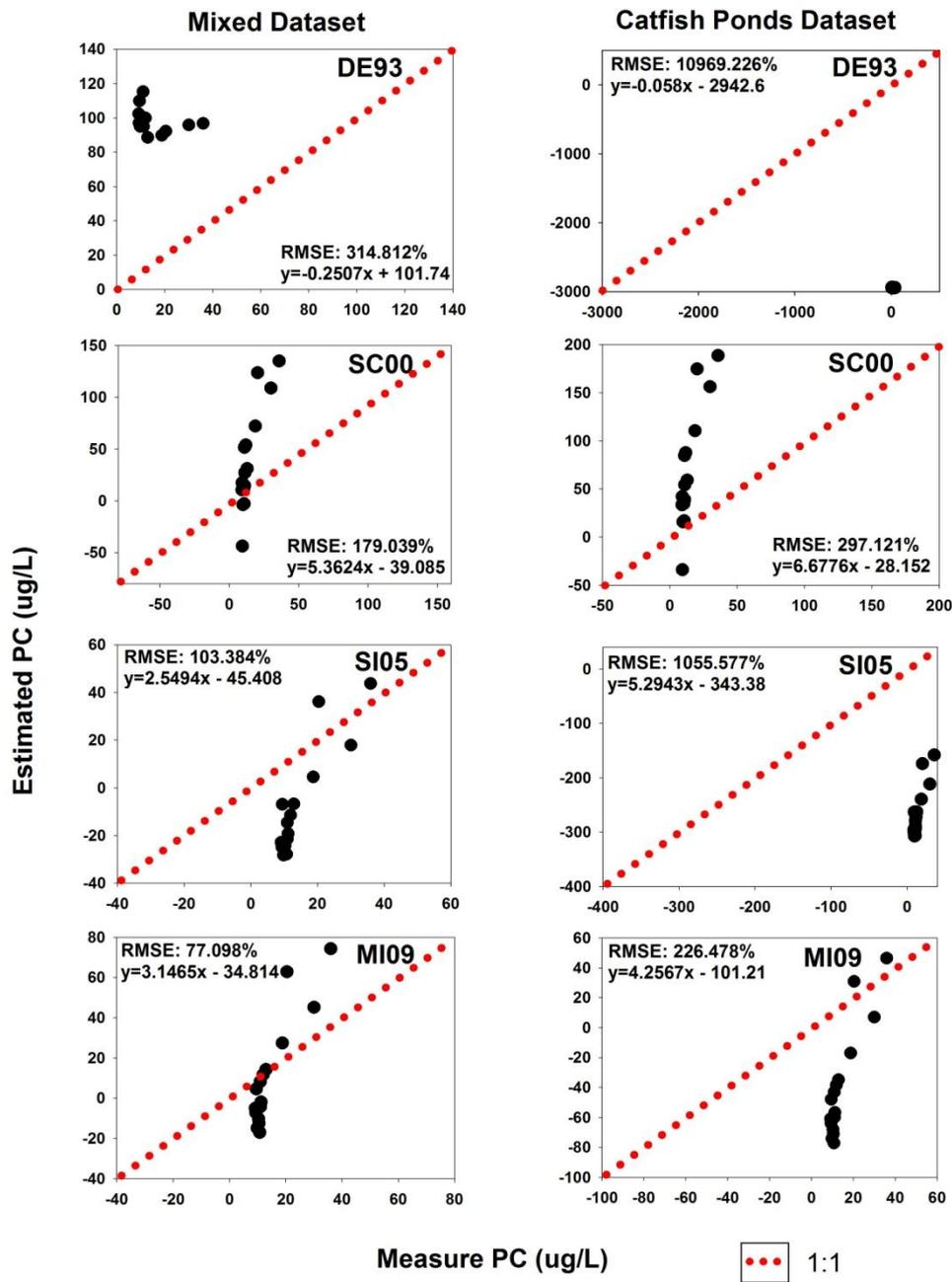
Figure 4.7a - Validation for DE03, SC00, SI05 and MI09 to Funil Reservoir dataset using calibrations from (1) Mixed dataset and (2) Catfish Ponds dataset
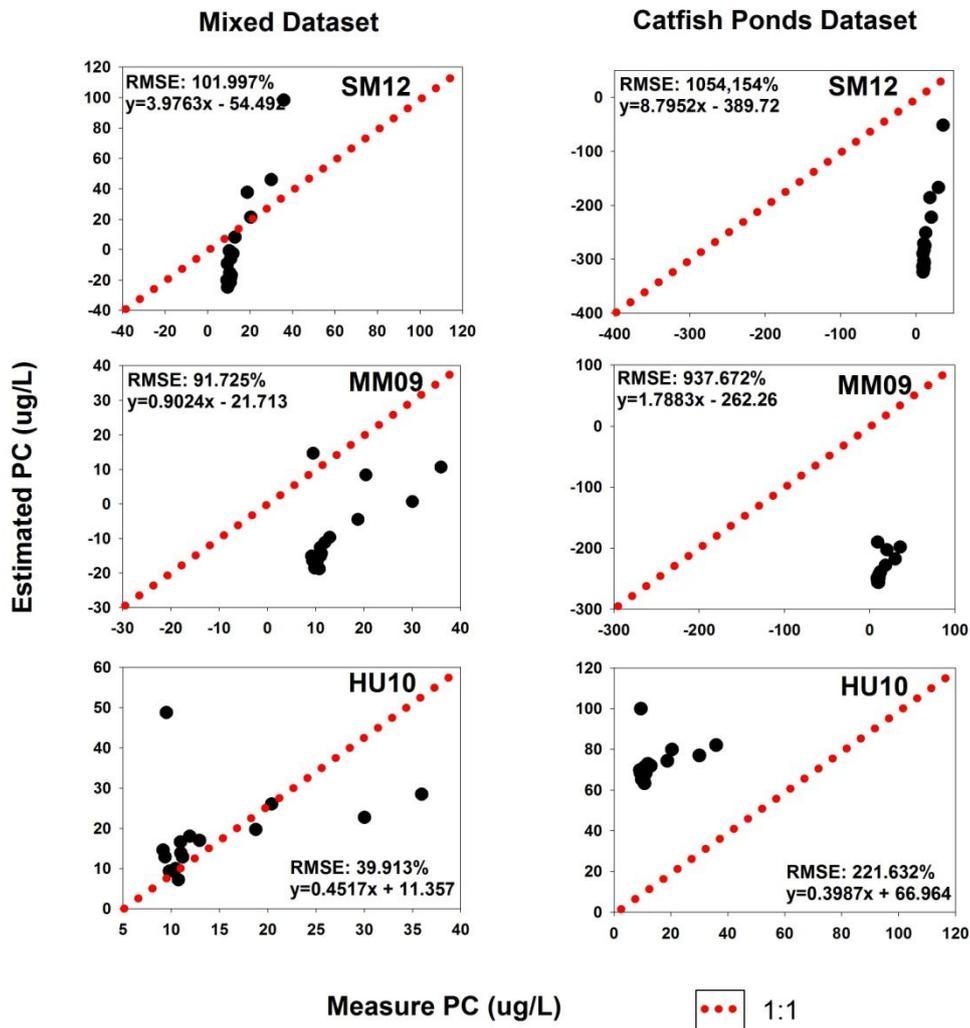
Figure 4.7b - Validation for SM12, MM09, and HU10 to Funil Reservoir dataset using calibrations from (1) Mixed dataset and (2) Catfish Ponds dataset

Validation plots for catfish ponds dataset used Funil and Mixed datasets calibrations (Figure 4.8a and b). Validations showed to be very poor at PC concentrations higher than 500 µg/L in all cases. The best validations were found using MM09 for the Funil calibration, and MM09 and SI05 for the mixed dataset calibration.
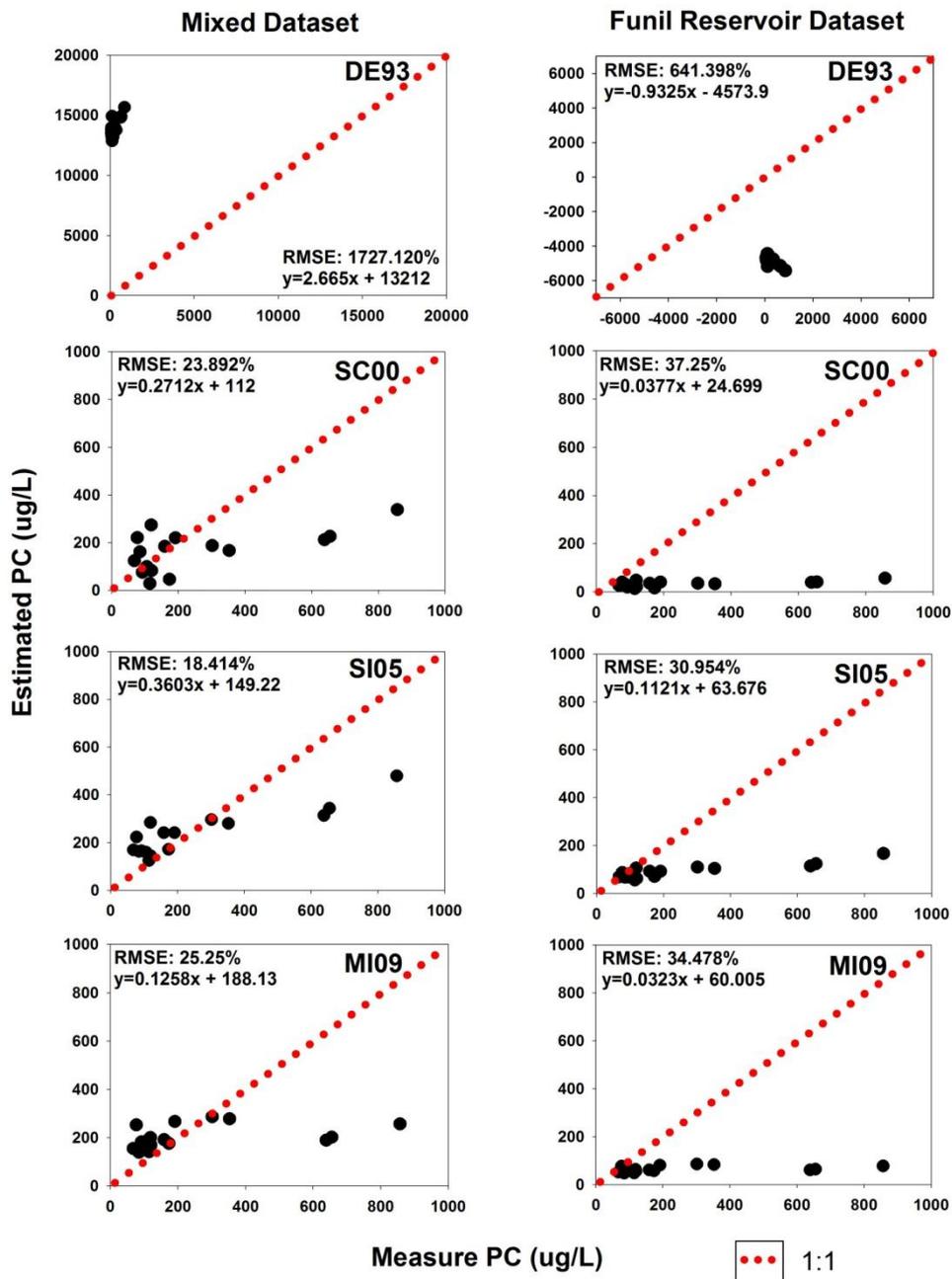
Figure 4.8a - Validation for DE03, SC00, SI05 and MI09 to Catfish Pond dataset using calibrations from (1) Mixed dataset and (2) Funil Reservoir dataset
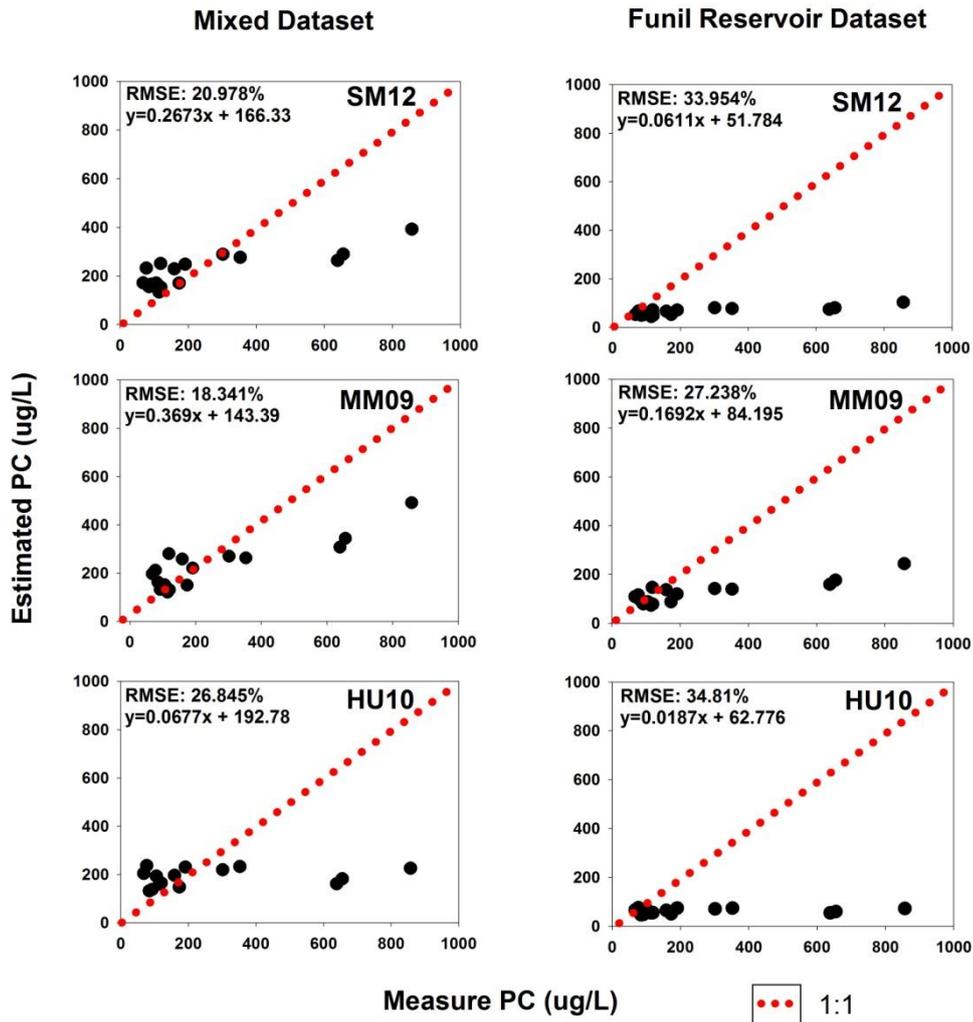
Figure 4.8b - Validation for SM12, MM09, and HU10 to Catfish Pond dataset using calibrations from (1) Mixed dataset and (2) Funil Reservoir dataset

The use of three different datasets showing low, high and mixed range of PC concentrations allowed us to analyze which calibration is more accurate for different environments. For a low PC concentration environment, the calibration using HU10 and the mix dataset (wide range) produced the best validation result. For a high PC concentration environment, mix dataset calibrations also produced some of the best results with SI05 and MM09 models due to its wide range. Mixed dataset calibration also showed the best validation plots for the rest of the 40% of the mixed data using MM09.

However, if we observe the validation plots for the catfish ponds dataset in Figure 4.8, it is possible to notice a cloud of points in the region of low PC concentration. This cloud of points does not have a linearity which also contributes to the poor validation results. The reason for this non-linear behavior of the scatter plot could be attributed to the dominant species of cyanobacteria in the catfish ponds, *Planktothrix agardhii*. Post et al. et al. (1985) described that this species can significantly increase the content of chl-*a* thus varying the irradiance. At sampling points with low PC in the catfish ponds, the PC to chl-*a* ratio (Table 4.4) were also lower due to high values of chl-*a*. Thus, the high chl-*a* concentration for the points with low PC concentration, due to this specific characteristic of *Planktothrix agardhii*, could have been the reason for the cloud of points and interfered in the PC estimation.

Table 4.4 PC and Chl-a ratio for the Catfish Ponds Dataset

PC	Chl-*a*	PC:Chl-*a*
68.13	228.26	0.30
77.19	229.25	0.33
83.19	59.79	1.39
84.88	205.60	0.41
92.24	117.40	0.78
105.75	131.05	0.80
114.50	94.03	1.22
116.82	109.26	1.07
118.79	360.01	0.33
119.02	152.50	0.78
119.61	130.43	0.91
136.44	101.40	1.34
159.31	332.38	0.48
173.54	117.42	1.48
191.12	198.50	0.96
203.17	164.30	1.23
234.32	149.61	1.56
301.60	210.83	1.43
352.66	155.54	2.26
550.96	168.22	3.27
639.02	539.73	1.18
655.33	507.70	1.29
857.08	831.35	1.03

Table 4.5 shows the error analysis for all models and for the three validation datasets. For the mixed dataset, the best results were obtained by using MM09 in the Mixed and Funil's calibrations, with an RMSE of 15.675% and 23.985% respectively. The best catfish ponds calibration for the mixed dataset used SC00 algorithm and had a RMSE of 18.179%. The lowest errors in Funil dataset were found using HU10 model with a RMSE of 221.63% and 40.92% for catfish ponds and mixed calibrations respectively. It showed that the errors decreased by the use of mixed calibration, enhancing the importance of using a large range of PC concentrations for the calibration of these models. These results also showed that the catfish ponds calibration mostly overestimates the PC prediction values. On the other hand, for the catfish ponds dataset, it was observed that the models which were calibrated with low PC range perform better when compared to the opposite (predicting low PC concentration from calibrations with high PC concentration). This could be due to the fact that mostly the non-linearity or signs of saturation during calibration were observed at high PC concentrations. Overall, results showed that the MM09 was the best model for the Funil and Mixed datasets with a RMSE of 23.985% and 15.675% respectively. These results also confirmed that it is possible to improve the accuracy of these models since the validation results (Figures 4.3, 4.4 and 4.5) showed that there is still some residual interference at the PC absorption region. The interference was observed for data points where the PC concentration was zero but the bio-optical models produced a significant value. Interference from CDOM absorption is not an issue for the spectral range used in these models; therefore, the residual scattering from algal pigments and TSS are the potential interference factors at these wavelengths.

Table 4.5 - Error analysis for the linear calibrations for each model and dataset (shaded areas represent the lowest errors)

	Mixed Dataset						
	Mixed Calibration						
Estimator	**D93**	**SC00**	**S05**	**M09**	**SM12**	**MM09**	**H10**
Bias	27.884	55.119	30.472	36.709	34.287	36.062	43.176
MAE	156.034	100.247	84.726	111.710	95.558	79.642	111.087
MSE	59821.765	31009.467	18507.809	39371.406	25612.029	17665.301	43296.194
RMSE	244.585	176.095	136.043	198.422	160.038	132.911	208.077
NRMSE(%)	28.845	20.768	16.044	23.401	18.874	15.675	24.540
	Funil Reservoir Calibration						
Bias	171.474	145.279	109.744	124.394	125.551	90.375	125.742
MAE	173.428	147.109	112.190	125.891	125.922	96.090	127.198
MSE	86109.276	72634.933	52200.685	65289.794	62249.894	41362.024	66594.099
RMSE	293.444	269.509	228.475	255.519	249.499	203.377	258.058
NRMSE(%)	34.607	31.785	26.945	30.135	29.425	23.985	30.434
	Catfish Ponds Calibration						
Bias	3103.557	6.313	128.852	43.635	138.474	123.386	1.175
MAE	3103.557	105.260	154.526	125.628	174.409	147.100	140.362
MSE	9688859.449	23761.486	36958.560	38411.144	46590.750	30953.637	42369.837
RMSE	3112.693	154.148	192.246	195.988	215.849	175.936	205.839
NRMSE(%)	367.097	18.179	22.673	23.114	25.456	20.749	24.276
	Funil Reservoir Dataset						
	Catfish Ponds Calibration						
Bias	2939.150	-57.184	279.993	52.170	275.038	250.650	-58.610
MAE	2939.150	62.948	279.993	55.642	275.038	250.650	58.610

MSE	8638835.017	6338.247	79998.696	3682.608	79783.183	63125.493	3526.687
RMSE	2939.190	79.613	282.840	60.684	282.459	251.248	59.386
NRMSE(%)	10969.226	297.121	1055.577	226.478	1054.154	937.672	221.632

<center>Mixed Calibration</center>

Bias	-83.570	-24.276	22.903	3.636	11.262	23.130	-3.393
MAE	83.570	34.342	25.841	16.831	23.490	23.768	5.927
MSE	7115.514	2301.443	767.377	426.762	746.925	604.059	114.377
RMSE	84.354	47.973	27.702	20.658	27.330	24.578	10.695
NRMSE(%)	314.812	179.039	103.384	77.098	101.997	91.725	39.913

<center>**Catfish Ponds Dataset**</center>

<center>Funil Reservoir Calibration</center>

Bias	5040.604	207.704	150.849	173.707	174.972	116.461	174.222
MAE	5040.604	207.704	151.761	173.707	174.972	126.505	174.222
MSE	25606599.392	86365.614	59637.746	73992.014	71760.882	46177.712	75424.552
RMSE	5060.296	293.880	244.208	272.015	267.882	214.890	274.635
NRMSE(%)	641.398	37.250	30.954	34.478	33.954	27.238	34.810

<center>Mixed Calibration</center>

Bias	-13613.808	64.019	5.273	22.999	10.620	8.999	32.391
MAE	13613.808	128.858	104.186	128.950	115.237	104.689	140.536
MSE	185669971.223	35529.975	21105.169	39685.667	27393.270	20938.331	44856.741
RMSE	13626.077	188.494	145.276	199.213	165.509	144.701	211.794
NRMSE(%)	1727.120	23.892	18.414	25.250	20.978	18.341	26.845

4.3.2. Sensitivity analysis

Sensitivity analyses were performed using the mixed dataset due to its overall strong performance and wide PC concentration range. Some of the best performing models including SC00, SI05, MI09 and MM09 were used to analyze their sensitivity to chl-*a* (Figure 4.6). The color scale is based on individual model outputs. Figure 4.6A showed that SC00 was insensitive to both chl-a and PC, and therefore, is not suitable to retrieve PC accurately although it was nearly insensitive to chl-*a*. SI05 on the other hand showed (Figure 4.6B) to be a good estimator for PC concentration because of its high sensitivity to PC. However, it also showed a high sensitivity to chl-*a* (Figure 4.6B). In contrast, MI09 showed high sensitivity to PC and low sensitivity to chl-a corroborating to the fact that chl-*a* effect on MI09 band ratio is comparatively less than other models as previously shown in Mishra et al. (2009) (Figure 4.6C). MI09 was developed to avoid the residual chl-*a* absorption at the widely used PC absorption maxima, i.e., at 620 nm. This was accomplished by moving the PC sensitive band to 600 nm instead of using 620 nm in the band ratio model. MM09, a modified MI09, showed high sensitivity to both PC and chl-*a* similar to SIO5 (Figure 4.6D).
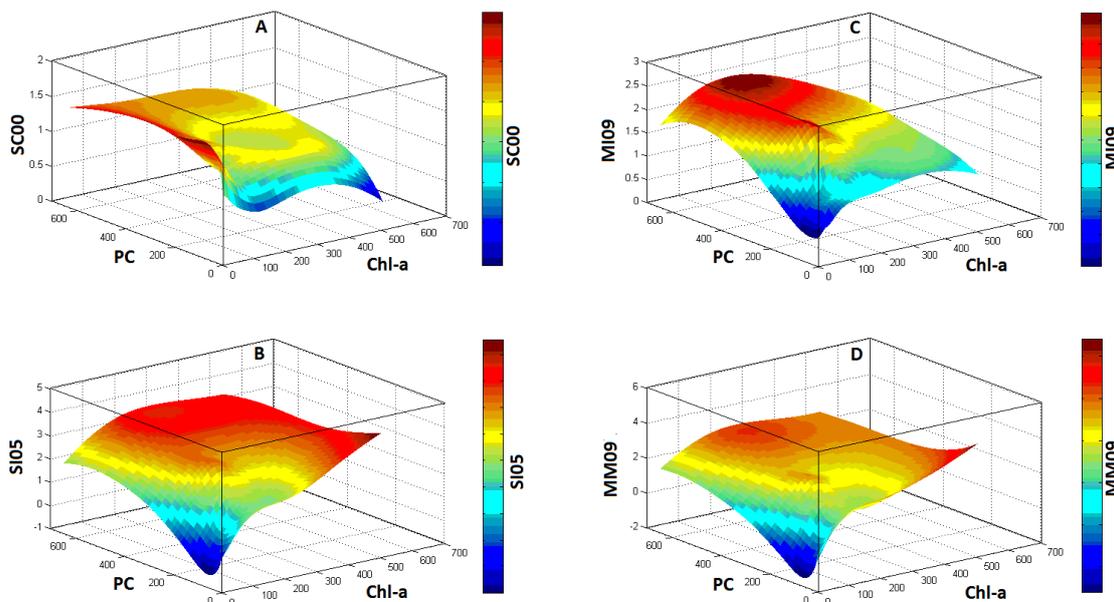
Figure 4.6 - (a) Sensitivity analysis showing the interference of chl-*a* on the performance of (A) SC00, (B) SI05, (C) MI09, and (D) MM09

These results showed that, overall, MI09 has the least interference from chl-*a* and can be used to accurately monitor blue-green algal in widely varying water bodies. Although MI09 was developed using a dataset collected from a series of controlled laboratory experiments with two cyanobacteria species (*Synechocystis* sp. and *Anabaena* sp.) (MISHRA et al., 2009), our review shows that it still serves as the most accurate algorithm to be used in natural environments. To confirm the results of the sensitivity analysis, a linear regression between these models and chl-*a* concentration was conducted. The results of the regression showed that SC00 and MI09 were the models without a significant dependency on chl-*a* concentration with R^2 of 0.42 and 0.38 respectively. On the other hand contrary, SI05 and MM09 showed a significant dependency on chl-*a* with a R^2 of 0.65 and 0.66 respectively. This analysis also revealed that MI09 can be used in semi-analytical algorithms to solve for PC absorption at 600 nm which can be safely assigned to PC without chl-*a* interference.

4.4.   Improvement for semi-empirical bio-optical models

Based on the findings presented at section Ogashawara et al. (2013), it was possible to observe that there is an influence of chl-*a* and TSS on the R_{rs} spectra at PC absorption region. To confirm this we ran a series of two dimensional color correlograms of R_{rs} spectra from Funil Hydroeletric Reservoir. Each correlogram correlates 292681 band ratios values from the R_{rs} spectra to each limnological concentration (Figure 4.7).
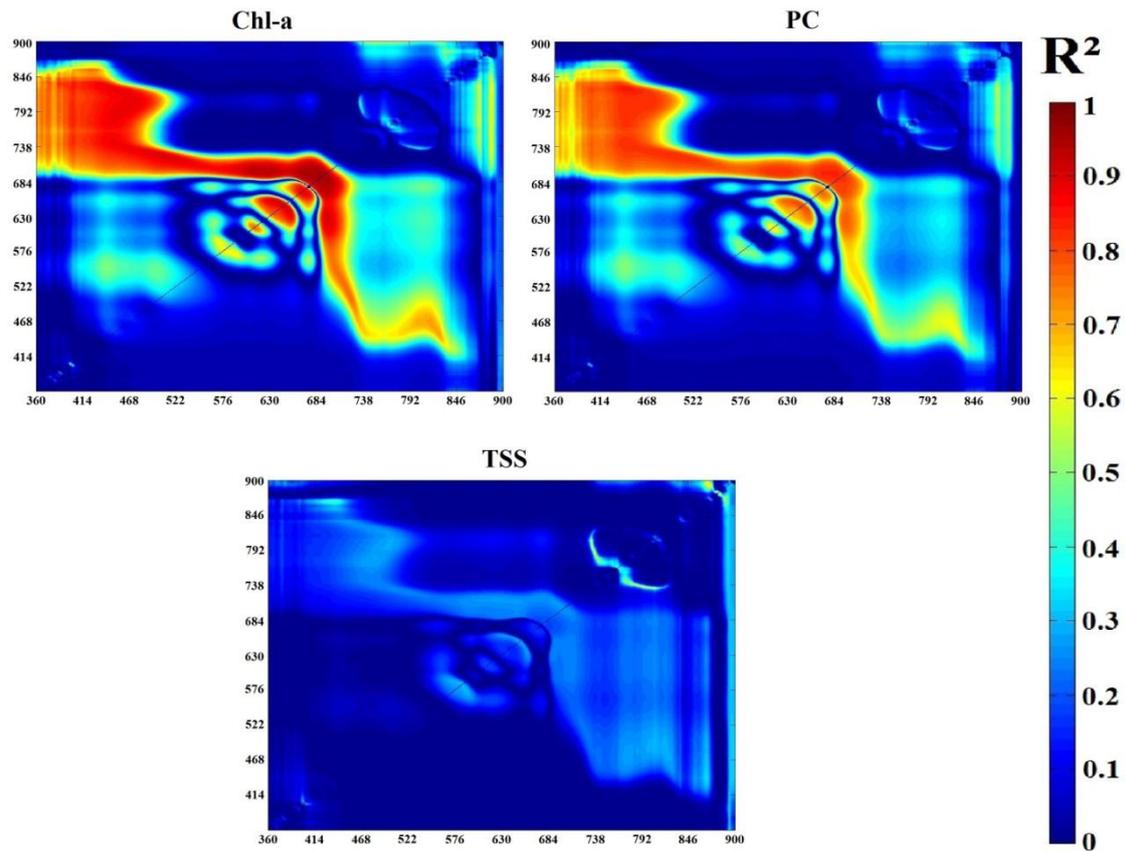
Figure 4.7 - Two dimensional color correlograms of R_{rs} band ratios and concentration of chl-*a*, PC and TSS.

From the results of the color correlogram showed on Figure 4.7, we generate a 3D surface plot from the R^2 values of each color correlogram. The surface plot (Figure 4.8) shows the R^2 values of the three OACs: PC on the x axis; TSS on the y axis; and chl-*a* on the z axis. It shows that the high R^2 between band ratios and PC (around 0.9) were also high for chl-*a* (around 0.8) and around 0.4 for TSS. Thus, it shows that band ratios which were correlated to PC were also correlated to chl-*a* and TSS.
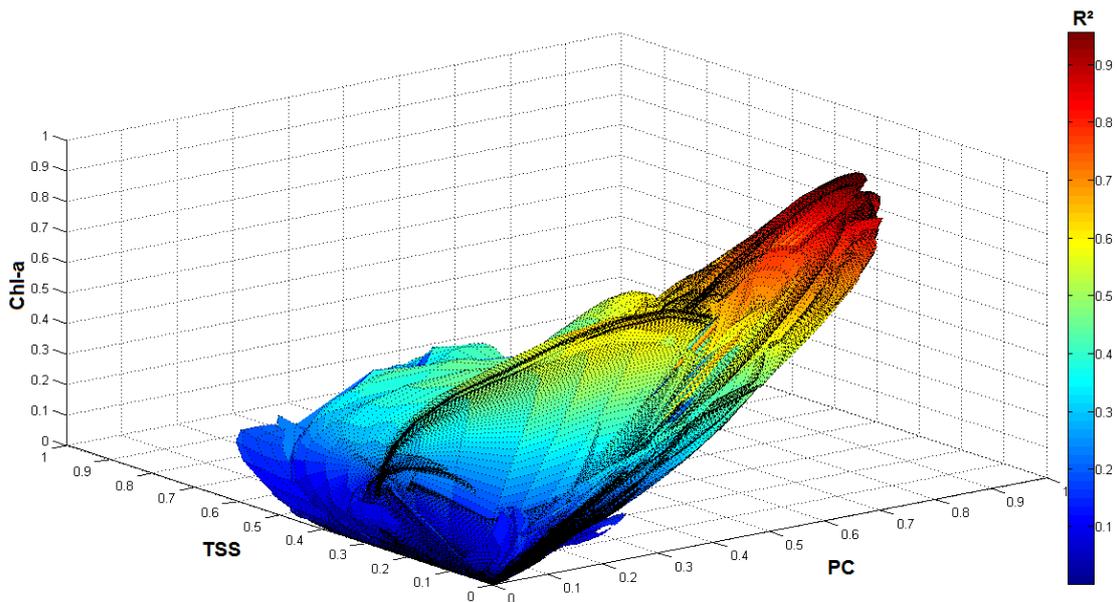
Figure 4.8 - 3D surface plot from the two dimensional color correlograms

Applying the PC band ratio algorithms such as SC00, SI05 and MI09, it also showed the interference of these OACs. A high R^2 value (0.93) was found between chl-*a* concentrations and MI09, while for SC00 and SI05 a R^2 of 0.88 and 0.90 were found, respectively. It shows that PC algorithms are very sensitive to chl-a. For PC concentrations prediction, SC00 and SI05 produced a R^2 of 0.77 and 0.78 respectively, while MI09 showed a R^2 of 0.82; proving that MI09 is the most sensitive to PC. However, all algorithms showed more sensitivity to chl-a than PC. For the TSS correlogram, SC00 produced a R^2 of 0.18 (p= 0.41), while SI05 and MI09 showed a R^2 of 0.26 (p= <0.001) and 0.24 (p= 0.019) respectively, indicating some influence of TSS at the PC absorption feature.

In order to reduce the influence of these constituents at the PC absorption spectral region, we developed a filter using the inverse R_{rs} values. The R_{rs} values were used due to the fact that it could act as a proxy to spectral absorption. These values were used to isolate the PC absorption signal at 600, 620, and 625 nm from the composite absorption signal at those spectral regions due to the influence of OACs the absorption of non PC constituents. R_{rs}^{-1} at 575 nm was used in this PC absorption isolation procedure with an assumption that inverse reflectance at 575 nm could be related to the absorption of chl-*a* and

reflectance of TSS. R_{rs}^{-1} (575 nm) value was subtracted from the reflectance value at 600, 620, and 625 nm and then inverted again (Eq. 4.1). The filtered value of R_{rs} was then used in the band ratios.

$$R_{rs}(\lambda_0) = \left[R_{rs}^{-1}(\lambda_0) - R_{rs}^{-1}(575)\right]^{-1} \tag{4.1}$$

where: λ_0 is the target wavelength.

To analyze the improvement of the use of this filter, we applied it to the PC band ratios (SC00, SI05 and MI09) using the Mixed Dataset described on section 3.6. Table 4.6 shows the results of calibration using 40% of the mixed dataset. Estimators include R^2, adjusted R^2, slope (X_1) and p-value. After the application of the filter, the R^2 increased in all cases when compared to the Raw algorithm.

Table 4.6 - Calibration Parameters from Mixed Dataset

Model	Filter	R^2	Adj. R^2	X_1	p-value
SC00	Raw	0.499	0.476	-1614.55	0.000166
SC00	Filtered	0.705	0.691	1320.626	p < 0.0001
SI05	Raw	0.684	0.67	132.365	p < 0.0001
SI05	Filtered	0.784	0.774	327.53	p < 0.0001
MI09	Raw	0.546	0.525	198.107	p < 0.0001
MI09	Filtered	0.7	0.685	728.147	p < 0.0001

To evaluate the improvement of each approach we calculated (Table 4.7) the NRMSE (%) between the estimated and measured PC concentration, after the application of the calibration described in Table 1. This analysis shows that for the mixed dataset, the filtered procedure produced the lowest errors for all three algorithms with a NRMSE(%) of 12.69, 9.67, and 18.49 for SC00, SI05, and MI09 respectively; while using the raw values the NRMSE(%) were 56.42, 16.04, and 23.40% for SC00, SI05, and MI09 respectively. For Funil Reservoir dataset, the lowest NRMSE(%) was found in the filtered version of MI09, with an NRMSE (%) of 75.28, however, the filtered application of SC00 algorithm showed the most significant improvement among all models. In the catfish ponds datasets, the use of our filter was the most successful because of the significantly higher PC concentrations in that water body. It is important to note that, MI09 did not show a significant improvement in all three datasets before

and after the filter procedure, proving once again that it is least sensitive to chl-a and TSS and most sensitive to PC.

Table 4.7 - Error Analysis

Model	Filter	NRMSE (%)	Model	Filter	NRMSE (%)	Model	Filter	NRMSE (%)
Mixed dataset			Funil dataset			Catfish Ponds dataset		
SC00	Raw	56.42	SC00	Raw	410.147	SC00	Raw	73.73
SC00	Filtered	12.694	SC00	Filtered	170.516	SC00	Filtered	22.382
SI05	Raw	16.044	SI05	Raw	102.798	SI05	Raw	18.414
SI05	Filtered	9.67	SI05	Filtered	88.12	SI05	Filtered	12.873
MI09	Raw	23.401	MI09	Raw	79.804	MI09	Raw	25.25
MI09	Filtered	18.493	MI09	Filtered	75.282	MI09	Filtered	20.197

Our results also show that it is possible to enhance the accuracy of PC bio-optical models up to 77% in some cases. This improvement is important not only for semi-empirical algorithms but also for semi-analytical ones which typically use band ratio as an estimator of PC. These improved models can be applied to the upcoming satellite multispectral sensors such as the Ocean and Land Color Instrument (OLCI) from European Space Agency, which will have a spectral band centered at 620 nm.

4.5. QAA development

4.5.1. QAA from the literature

To test the need of a re-parameterization of a QAA for a tropical reservoir, we tested two QAA from the literature: QAAv5 (LEE et al., 2009) and QAA for turbid productive waters (MISHRA et al, 2014). We used the R_{rs} (eq. 3.1) acquired by RAMSES spectroradiometers from Funil Reservoir, Rio de Janeiro, Brazil.

4.5.1.1.   QAAv5

QAA in the native form is able to retrieve $a(\lambda)$ and $a_{phy}(\lambda)$ successfully in waters where $a(443)$ is less than 0.5 m^{-1} (MISHRA et al., 2014). In order to check it's applicability in tropical waters we evaluate its performance using NRMSE(%). For $a(\lambda)$ estimation, QAAv5 got an average NRMSE of 511%; while for $a_{CDM}(\lambda)$ and $a_{phy}(\lambda)$ it got an average NRMSE of 885 and 9401%. Although the results

of NRMSE were accurate for $a(\lambda)$ and $a_{CDM}(\lambda)$, their spectra did not agree with the accuracy.

Figure 4.9 shows the estimated and measured $a(\lambda)$ spectra. Figure 4.9A shows the spectra for the best NRMSE (25%) while Figure 4.9B shows the spectra for the worst NRMSE (875%). Although the use of QAAv5 has low NRMSE for the estimation of $a(\lambda)$, such variations on the estimated spectra increases the errors for the others estimations.
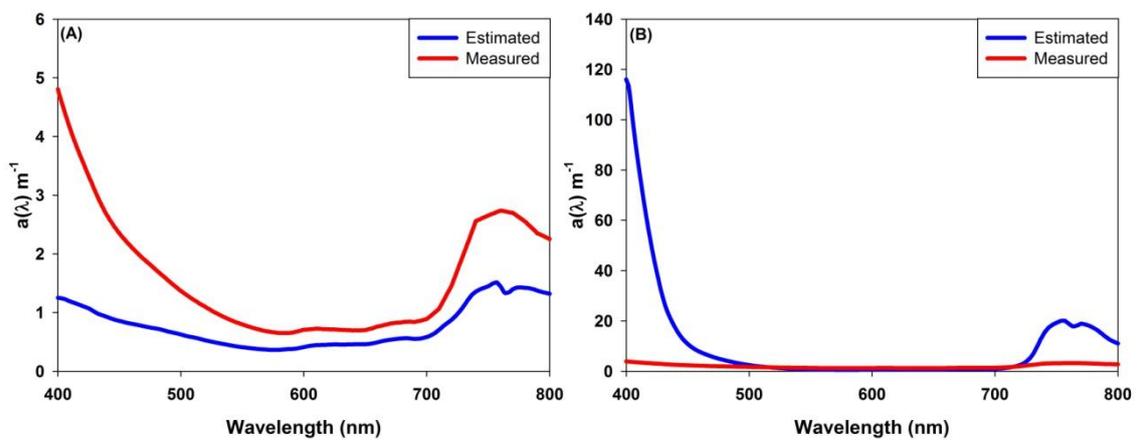
Figure 4.9 - Estimated and measured $a(\lambda)$; a) the best NRMSE of 25%, and b) the worst NRMSE of 875%.

Figure 4.10 shows the estimated and measured $a_{CDM}(\lambda)$ spectra. Figure 4.10A shows the spectra for the best NRMSE (25%) while Figure 4.10B shows the spectra for the worst NRMSE (1636%). Once again, although the use of QAAv5 has low NRMSE for the estimation of $a_{CDM}(\lambda)$, such variations on the estimated spectra (almost 40 times the measured spectrum) increases the errors for the others estimations.
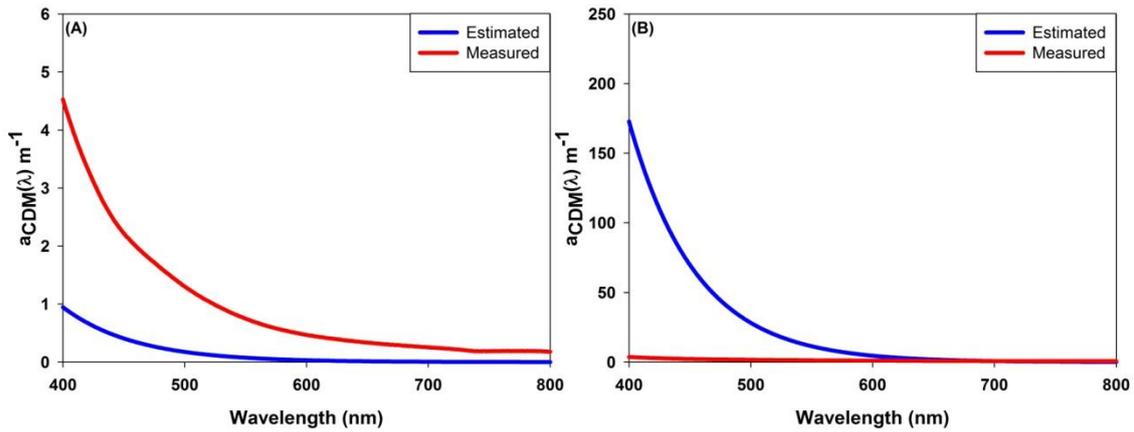
Figure 4.10 - Estimated and measured $a_{CDM}(\lambda)$; a) the best NRMSE of 25%, and b) the worst NRMSE of 1536%.

Figure 4.11 shows the estimated and measured $a_{phy}(\lambda)$ spectra. Figure 4.11A shows the spectra for the best NRMSE (153%) while Figure 4.11B shows the spectra for the worst NRMSE (33748%). In the estimation of $a_{phy}(\lambda)$ for both cases (the best and worst sample point estimation) the spectra of $a_{phy}(\lambda)$ were inaccurate. Even the sample point with the lowest NRMSE, the estimation of $a_{phy}(\lambda)$ was overestimating in the blue and green spectral channel and underestimating in the red and NIR spectral channel. For the sample point with the highest NRMSE, it was underestimating in the blue and green spectral channel and overestimating in the NIR.
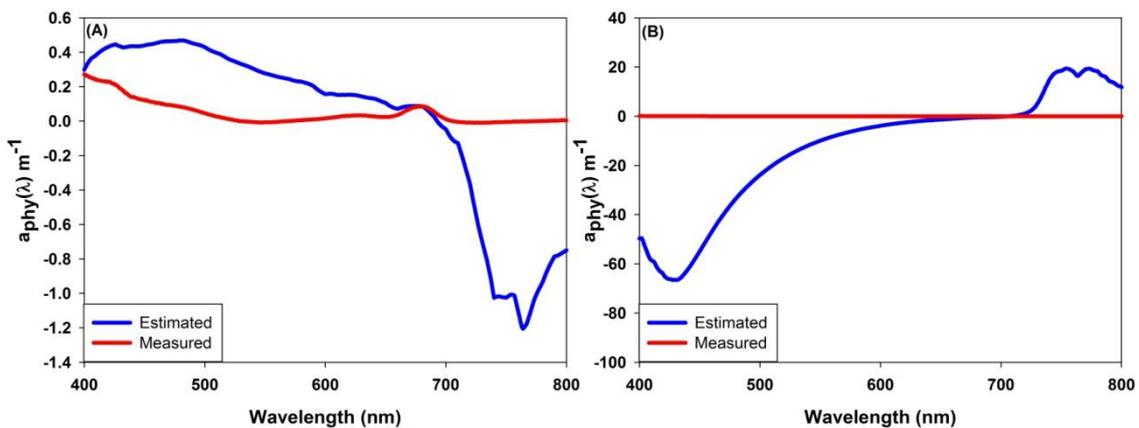
Figure 4.11 - Estimated and measured $a_{phy}(\lambda)$; a) the best NRMSE of 153%, and b) the worst NRMSE of 33748%.

Overall results showed that the main problem in the estimation of QAA_v5 in its native form is occurs in the step of $a(\lambda)$ estimation, which have been overestimated in the majority of the sample points. Thus, the estimation of

$a_{CDM}(\lambda)$ is compromised since its estimation is derived from the $a(\lambda)$ estimation, affecting all the estimations.

4.5.1.2.   QAA for turbid productive waters

Mishra et al. (2014) re-parameterize the QAA proposed by LEE et al. (2002) to make it suitable to work particularly in highly absorbing waters and algal bloom scenarios in inland ponds, lakes, and coastal and estuarine environments, where, chl-a concentration reaches as high as 1000 mg m^{-3} (MISHRA et al., 2014). The authors tried to solve the problem of $a(\lambda)$ estimation since an under or overestimation of it causes inaccurate estimation of $b_{bp}(\lambda_0)$ and propagates the error to others steps of the QAA.

Using Mishra et al. (2014) QAA for turbid productive waters the average NRMSE(%) for $a(\lambda)$ estimation was lower if compared to QAAv5. A NRMSE(%) of 3.99% was found, however as observed in the QAAv5, the spectra showed a lot of variation. Figure 4.12 shows the estimated and measured $a(\lambda)$ spectra. In Figure 4.12A it shows the spectra for the best NRMSE (21%) while in Figure 4.12B it shows the spectra for the worst NRMSE (1015%). Although the authors tried to correct the $a(\lambda)$ estimation, the use of QAA for turbid productive waters continued to overestimate the $a(\lambda)$.
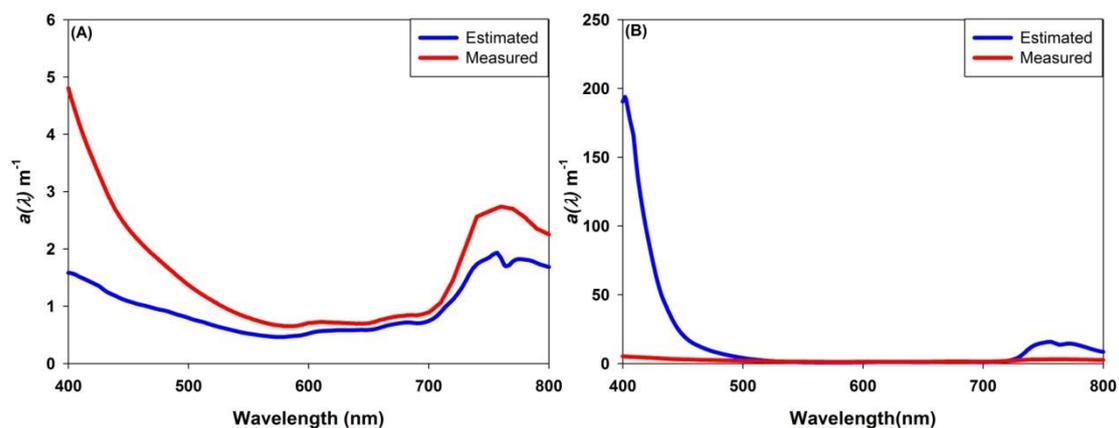

Figure 4.12 - Estimated and measured a(λ); a) the best NRMSE of 21%, and b) the worst NRMSE of 1015%.

Figure 4.13 shows the estimated and measured $a_{CDM}(\lambda)$ spectra, average *NRMSE(%)* of $a_{CDM}(\lambda)$ estimation was 726% which was also lower than the

NRMSE for the QAAv5. Figure 4.13A shows the spectra for the best NRMSE (23%) while Figure 4.13B shows the spectra for the worst NRMSE (2166%).
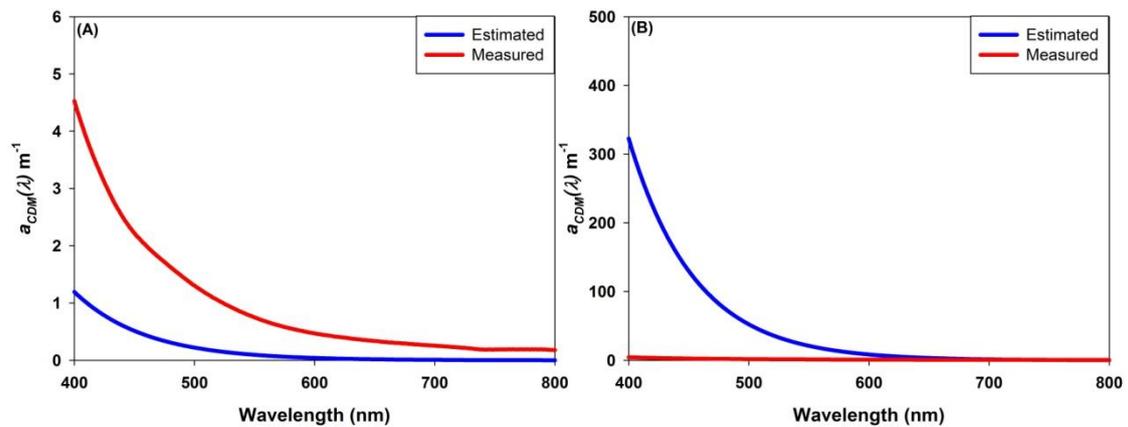
Figure 4.13 - Estimated and measured $a_{CDM}(\lambda)$; a) the best NRMSE of 23%, and b) the worst NRMSE of 2166%.

Average NRMSE(%) for $a_{phy}(\lambda)$ estimation was lower than in the QAAv5 with an NRMSE of 6911%. Figure 4.14 shows the estimated and measured $a_{phy}(\lambda)$ spectra. Figure 4.14A shows the spectra for the best NRMSE (129%) while Figure 4.14B shows the spectra for the worst NRMSE (20386%).

Although the use of QAA for turbid productive waters reduced the NRMSE for all the estimations, the $a(\lambda)$ estimations still overestimating in the values on the blue and green spectral regions. Therefore, $a_{CDM}(\lambda)$ and $a_{phy}(\lambda)$ estimations were compromised. In the $a_{phy}(\lambda)$ case, even the best sample point estimation got an inaccurate $a_{phy}(\lambda)$ spectrum.
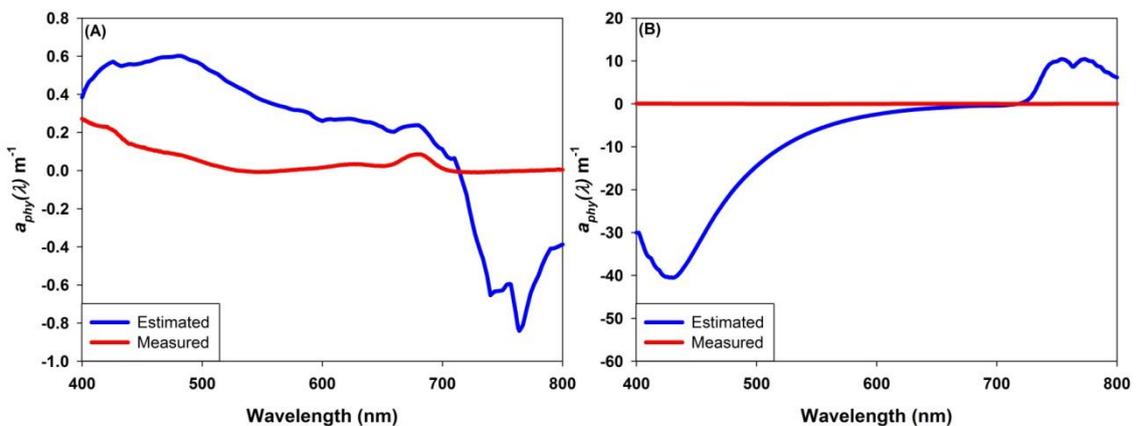
Figure 4.14 - Estimated and measured $a_{phy}(\lambda)$; a) the best NRMSE of 129%, and b) the worst NRMSE of 20386%.

Therefore, an empirical scheme to retrieve the *a(λ)* needs to be re-parameterized for successful retrieval of $a_{CDM}(λ)$ *and* $a_{phy}(λ)$ in a tropical reservoir.

4.5.2. Algorithm development

As noticed by applying QAAv5 and QAA for turbid productive waters, the main source of error was in the *a(λ)* estimation. Due to this reason we followed Mishra et al. (2014) steps 0 to 5 using the R_{rs} from Funil Reservoir.

The first step is based on the transformation of R_{rs} to r_{rs} (Equation 4.2):

$$r_{rs}(\lambda) = \frac{R_{rs}(\lambda)}{\left(0.52 + 1.7R_{rs}(\lambda)\right)}$$

(4.2)

The second step is the estimation of *u* which is calculated following Equation 4.3.

$$u = \frac{b_b(\lambda)}{\left(a(\lambda) + b_b(\lambda)\right)} = \frac{-0.0895 + \sqrt{(g_0)^2 + 4g_1 \cdot r_{rs}(\lambda)}}{2g_1}$$

(4.3)

Where: g_0 = 0.089 and g_1 = 0.125

The third step is the estimation of total absorption at a reference wavelength (708 nm)which shown on Equation 4.4.

$$a(708) = a_w(708) + 10^{-a-b\chi-c\chi^2}$$

(4.4)

Where *a* = 0.7153; *b* = 2.054; *c* = 1.047 and χ is calculated from equation 4.5.

$$\chi = \log_{10}\left(\frac{0.01 \cdot r_{rs}(443) + r_{rs}(620)}{r_{rs}(708) + 0.005 \cdot \frac{r_{rs}(620)}{r_{rs}(443)} \cdot r_{rs}(620)}\right)$$

(4.5)

The fourth step is the estimation of b_{bp} at the reference wavelength (708 nm).

$$b_{bp}(708) = \frac{u(708)a(708)}{1 - u(708)} - b_{bw}(708)$$

(4.6)

The fifth step is the estimation of $b_{bp}(λ)$.

$$b_b(\lambda) = b_{b,w}(\lambda) + b_{b,p}(708)\left(\frac{708}{\lambda}\right)^{\eta}$$

(4.7)

Where η is calculated from equation 4.8.

$$\eta = 2\left(1 - 1.2exp\left(-0.9\frac{r_{rs}(443)}{r_{rs}(555)}\right)\right) \tag{4.8}$$

The sixth step is the estimation of *a(λ)* which was overestimated on the QAAv5 and QAA for turbid productive waters. To solve this problem we change the factor 1 in the first subtraction to 0.1, as shown on Equation 4.9.

$$a(\lambda) = \frac{(0.1 - u(\lambda))\left(b_{b,w}(\lambda) + b_{b,p}(\lambda)\right)}{u(\lambda)} \tag{4.9}$$

From the total absorption spectrum, QAA was further decomposed into $a_{CDM}(λ)$ which is the combined absorption by CDOM and NAP. $a_{CDM}(λ)$ can be calculated by using the power spectral slope as in Equation 4.10.

$$a_{CDM}(\lambda) = a_{CDM}(443)e^{-S(\lambda-443)} \tag{4.10}$$

where, *S* was calculated using Equation 4.11 and $a_{CDM}(443)$ was calculated using Equation 4.12 as:

$$S = 0.015 + \frac{0.002}{0.6 + r_{rs}(443)/r_{rs}(560)} \tag{4.11}$$

$$a_{CDM}(443) = \frac{\left(a(411) - \zeta a(443)\right) - \left(a_w(411) - \zeta a_w(443)\right)}{\xi - \zeta} \tag{4.12}$$

where,

$$\zeta = 0.74 + \frac{0.2}{0.8 + r_{rs}(443)/r_{rs}(\lambda_0)} \tag{4.13}$$

$$\xi = e^{S(443-411)} \tag{4.14}$$

$a_{phy}(λ)$ in this work was calculated based on Lee et al. (2010) which uses a normalized phytoplankton absorption coefficient to provide the spectral shape of $a_{phy}(λ)$.

$$a_{phy}(\lambda) = a_{phy}(432)a_{phy}^+(\lambda) \tag{4.15}$$

where, $a_{phy}(432)$ can be calculated from Equation 4.16; and $a^+_{phy}(λ)$ was obtained from Roesler et al. (1989).

$$a_{phy}(432) = \frac{\left(\xi a(432) - a(411)\right) - \left(\xi a_w(432) - a_w(411)\right)}{\xi - \zeta}$$ (4.16)

4.5.3. Algorithm validation

To validate the proposed QAA (pQAA), we followed the same method used to analyze the QAAv5 and QAA for turbid productive waters. Therefore, the average NRMSE(%) for *a(λ)* estimation was 36%. If compared to QAAv5 (511%) and QAA for turbid productive waters (399%) the error estimation for the pQAA was very low. Not only the NRMSE was improved from the other two QAAs but also the spectra comparison was improved. Figure 4.15A shows the spectra for the best NRMSE (23%) while Figure 4.15B shows the spectra for the worst NRMSE (77%). It shows that the pQAA improved spectra even for the worst NRMSE sample point, which is more overestimated in the blue spectral region.
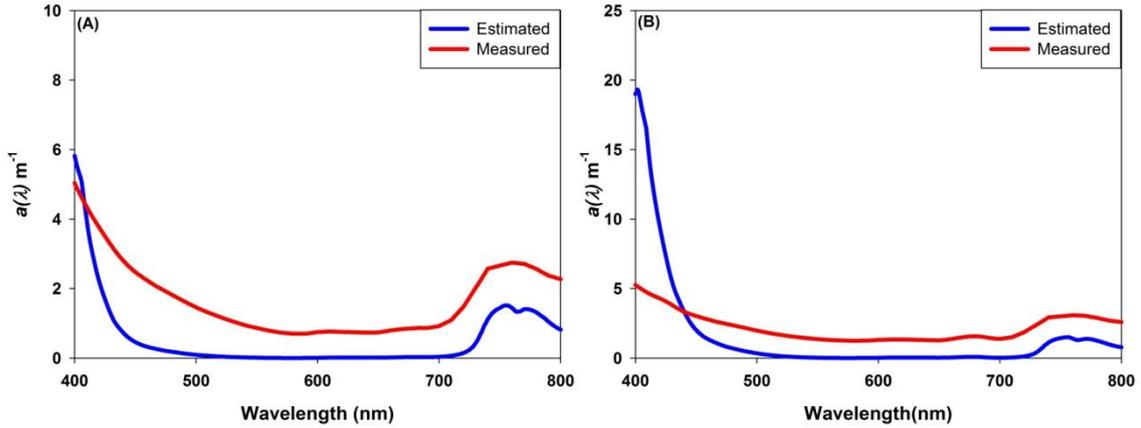
Figure 4.15 - Estimated and measured a*(λ)*; a) the best NRMSE of 23%, and b) the worst NRMSE of 77%.

For the average NRMSE of $a_{CDM}(λ)$ estimation was also lower if compared to the others QAAs. While the pQAA got an average NRMSE of 49%, QAAv5 and QAA for turbid productive waters got a NRMSE of 885% and 726% respectively. Figure 4.16 shows the estimated and measured $a_{CDM}(λ)$ spectra. Figure 4.16A shows the spectra for the best NRMSE (9%) while Figure 4.16B shows the spectra for the worst NRMSE (185%). Once again, application of pQAA for Funil Reservoir dataset showed a better accuracy in the spectra shapes for the estimated $a_{CDM}(λ)$.
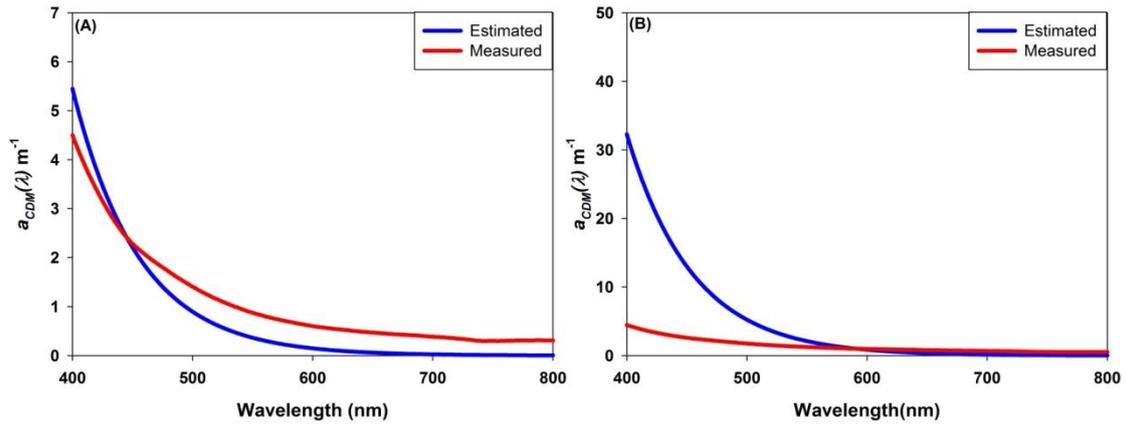
Figure 4.16 - Estimated and measured $a_{CDM}(\lambda)$; a) the best NRMSE of 9%, and b) the worst NRMSE of 185%.

For the average NRMSE of $a_{phy}(\lambda)$ estimation for pQAA got an average NRMSE of 74%, while for the QAAv5 and QAA for turbid productive waters got a NRMSE of 9401% and 6911% respectively. Figure 4.17 shows the estimated and measured $a_{phy}(\lambda)$ spectra. Figure 4.17A shows the spectra for the best NRMSE (16%) while Figure 4.17B shows the spectra for the worst NRMSE (180%). The most important achievement of the pQAA was the improvement of the spectral shape of estimated $a_{phy}(\lambda)$. The $a_{phy}(\lambda)$ estimation is important since it used in the estimation of PC concentration as described on section 3.8.
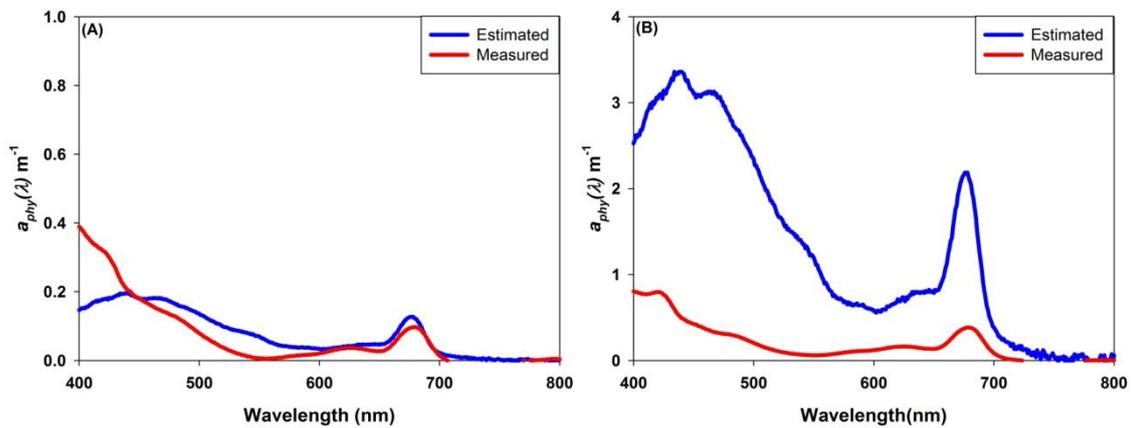
Figure 4.17 - Estimated and measured $a_{phy}(\lambda)$; a) the best NRMSE of 16%, and b) the worst NRMSE of 180%.

Overall results showed that the pQAA is more accurate due to the empirical re-parameterizations proposed in this study. More accurate results were estimated skipping the first step and using the measured r_{rs}. However, for the application

to orbital sensors the use of R_{rs} with an accurate atmospheric correction is required. Results for all studied points are shown on Appendix B.

4.6. PC estimation

PC concentration estimation from pQAA was calculated as described on section 3.8 following Mishra et al (2013) procedures. We use their empirical relationship to estimate ψ_1 and ψ_2 the results and we also used a fixed $a_{PC}^*(620)$ at 0.0019, based on Dekker (1993) measurements at two shallow hyper eutrophic lakes: Lake Naardermeer Wijde Blik and Lake Hollands Ankeveen which had a measured $a_{PC}^*(620)$ of 0.0022 and 0.0014 respectively.

Although the use of parameters estimated from remote sensing and calibrated from literature reviews, it was found a NRMSE of 24.94% with a R^2 of 0.98 (p-value < 0.0001) for the estimation of PC concentration. Figure 4.18 shows a scatter plot of estimated and measured PC concentration, as it could be observed, for all points there were an underestimation of PC concentration. However, for overall results, considering all the modeling behind this estimation, the PC concentration estimation was considered accurate enough for our state of art of bio-optical modeling.
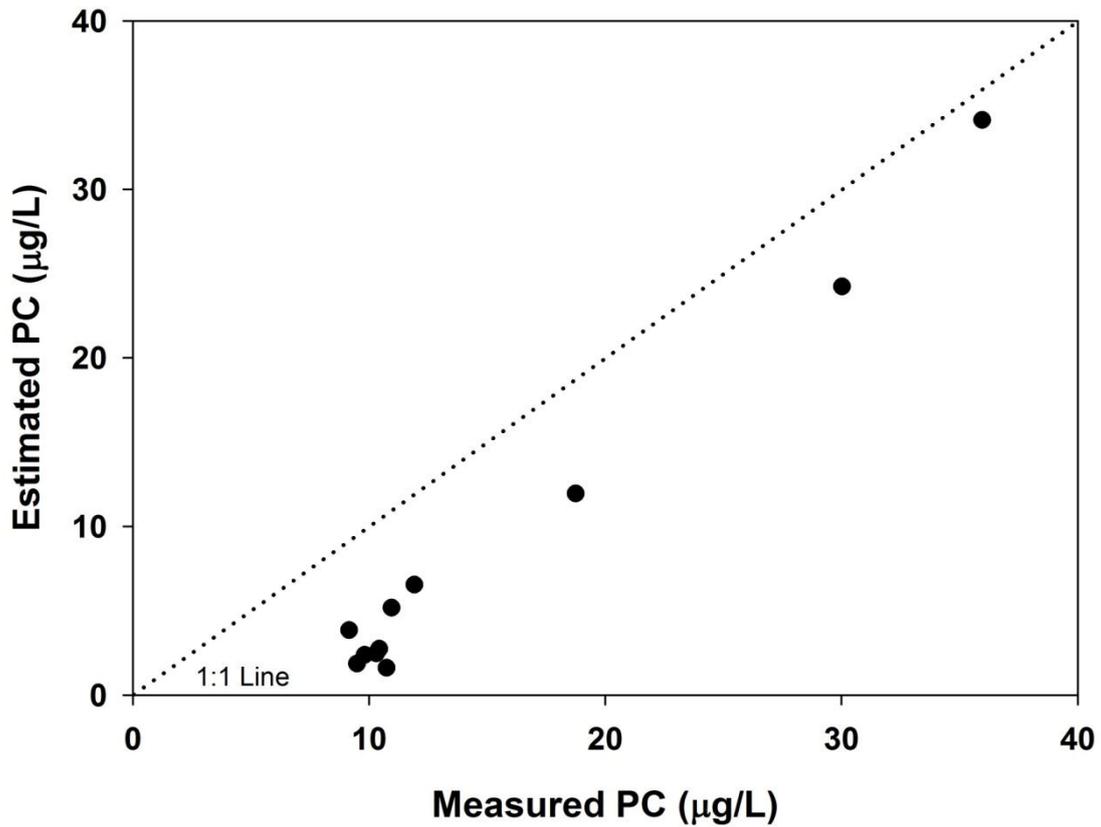
Figure 4.18 - Estimated and measured PC concentration

4.7. OLCI simulation

Firstly it was created a synthetic dataset of OLCI spectral bands following its spectral response function showed on section 3.9. A comparison between hyperspectral and the synthetic datasets is shown on Figure 4.19 which shows in A the hyperspectral R_{rs} data from proximal remote sensing and in B the synthetic OLCI R_{rs} data.
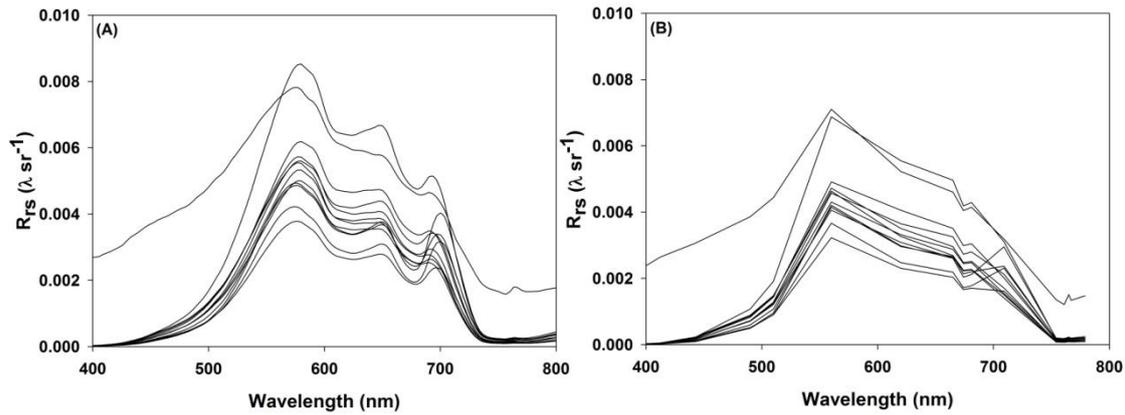
Figure 4.19 - R_{rs} a) for the proximal remote sensing; b) for the synthetic OLCI data.

The synthetic dataset of the 16 spectral bands of OLCI could estimate well the data hypespectral data, and could retrieve well some important features on the R_{rs} spectra. The absorption feature of chl-a at 665 nm was well described in the synthetic dataset and also the absorption of PC at 620 nm could be noticed due to OLCI's spectral band centered at 620 nm.

4.7.1. Application of pQAA

It was applied the pQAA for the OLCI synthetic dataset, following the same steps described on section 4.4.2 just using the nearest wavelengths of OLCI. Average NRMSE for $a(\lambda)$, $a_{CDM}(\lambda)$ and $a_{phy}(\lambda)$ estimations were low around 43%, 105% and 478% respectively.

Figure 4.20 shows the estimated and measured $a(\lambda)$ spectra. Figure 4.20A shows the spectra for the best NRMSE (25%) while Figure 4.20B shows the spectra for the worst NRMSE (98%).
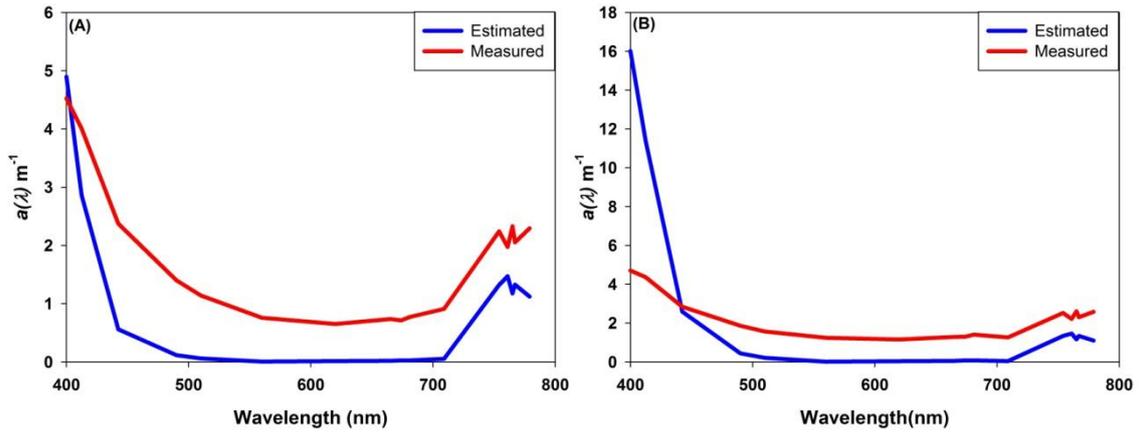
Figure 4.20 - Estimated and measured a*(λ)*; a) the best NRMSE of 25%, and b) the worst NRMSE of 98%.

Although the use of different wavelengths in the pQAA, the application of pQAA for OLCI synthetic dataset showed very similar results in the *a(λ)* spectra comparison between measured and estimated.

Figure 4.21 shows the estimated and measured $a_{CDM}(λ)$ spectra. Figure 4.21A shows the spectra for the best NRMSE (58%) while Figure 4.21B shows the spectra for the worst NRMSE (306%).
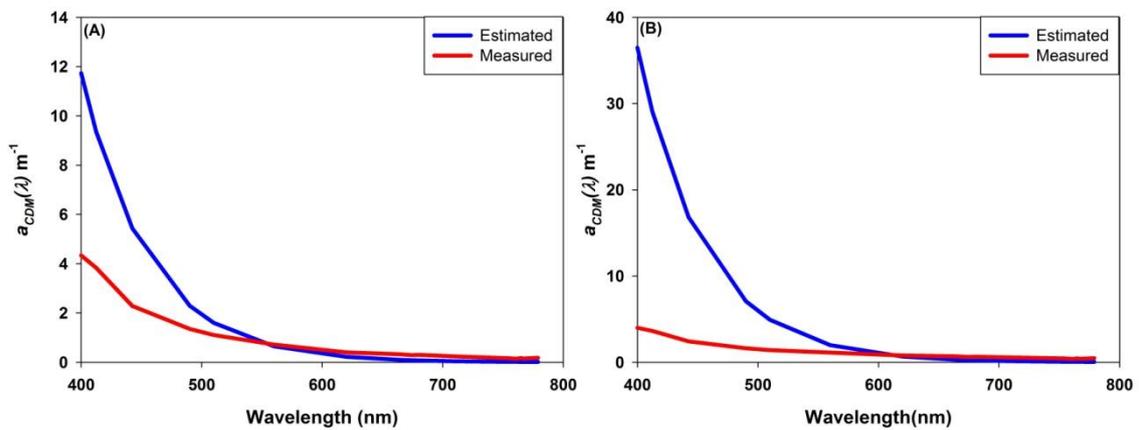
Figure 4.21 - Estimated and measured a$_{CDM}$*(λ)*; a) the best NRMSE of 58%, and b) the worst NRMSE of 306%.

Once again, application of pQAA for OLCI synthetic dataset showed very similar results to the hyperspectral dataset. Although the NRMSE results were low, the difference on the estimations at the blue spectral channel is high.

Figure 4.22A shows the spectra for the best NRMSE (52%) while Figure 4.22B shows the spectra for the worst NRMSE (1065%). The estimation of $a_{phy}(\lambda)$ is one of the most important goals of this thesis, since with the use of this estimation is possible to calculate the concentration of biological activity such as chl-a and PC.
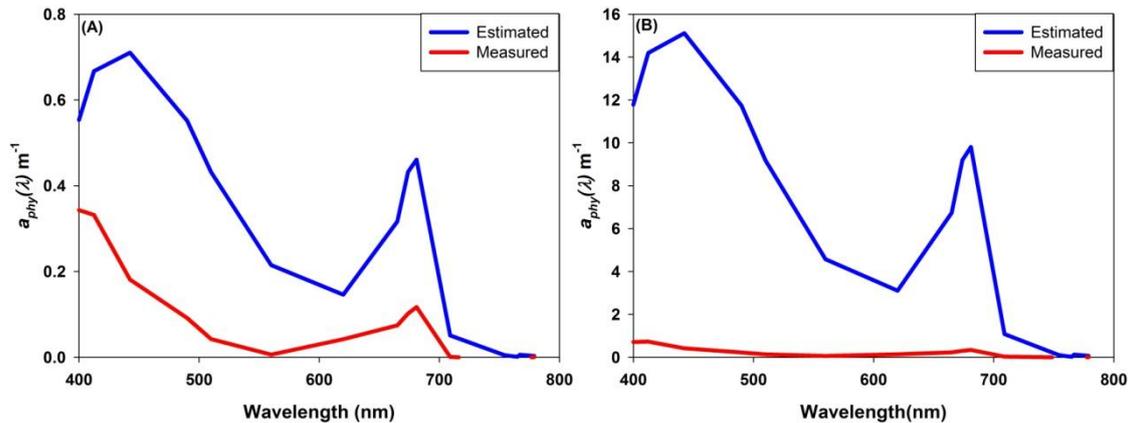
Figure 4.22 - Estimated and measured $a_{phy}(\lambda)$; a) the best NRMSE of 52%, and b) the worst NRMSE of 1065%.

Overall results using the synthetic OLCI dataset showed that the application pQAA in the future satellite Sentinel-3 can enhance the estimation of IOPs in tropical inland waters using the OLCI sensor. With the constellation proposal for the Sentinel Satellites Series, the monitoring of tropical inland aquatic systems can be also improved by the application of remote sensing technique such as the bio-optical modeling.

However, the use of remote sensing technologies for inland waters is limited by its spectral resolution. Usually, the remote sensing of inland water quality requires high spectral and spatial sensitivity from space-borne imaging spectroradiometers. The spatial resolution is needed because of the size of inland aquatic systems, however, it would be most welcome, current and planned satellite sensors to have spectral sensitivities in excess of what is needed for most water column OAC. Thus, from the perspective of water quality, upcoming hyperspectral satellite sensors such as Environmental Mapping and Analysis Program (EnMAP), Hyperspectral Infrared Imager (HyspIRI) and PRecursore IperSpettrale della Missione Applicativa (PRISMA)

as well as aquatic multispectral sensors such as OLCI and SABIA-MAR present exciting opportunities for generating inland and coastal water quality products.

4.7.2. Estimating PC concentration

The estimation of PC concentration from OLCI synthetic dataset was not accurate if compared to the hyperspectral dataset PC concentration estimation. The high NRMSE of 112.49% and a R^2 of 0.55 (p-value of 0.013) showed that improvements on the $a_{PC}^*(620)$ estimation should be developed for multispectral sensor, such as OLCI. As it was used Mishra et al. (2013) calibration which was settled with hyperspectral measures to estimate $a_{PC}^*(620)$, this low accuracy is probably derived from the use of a calibration for hyperspectral measures instead of using one for multispectral ones. Figure 4.23 shows the scatter plot of estimated and measured PC concentration, after removing few outliers with negative concentration.
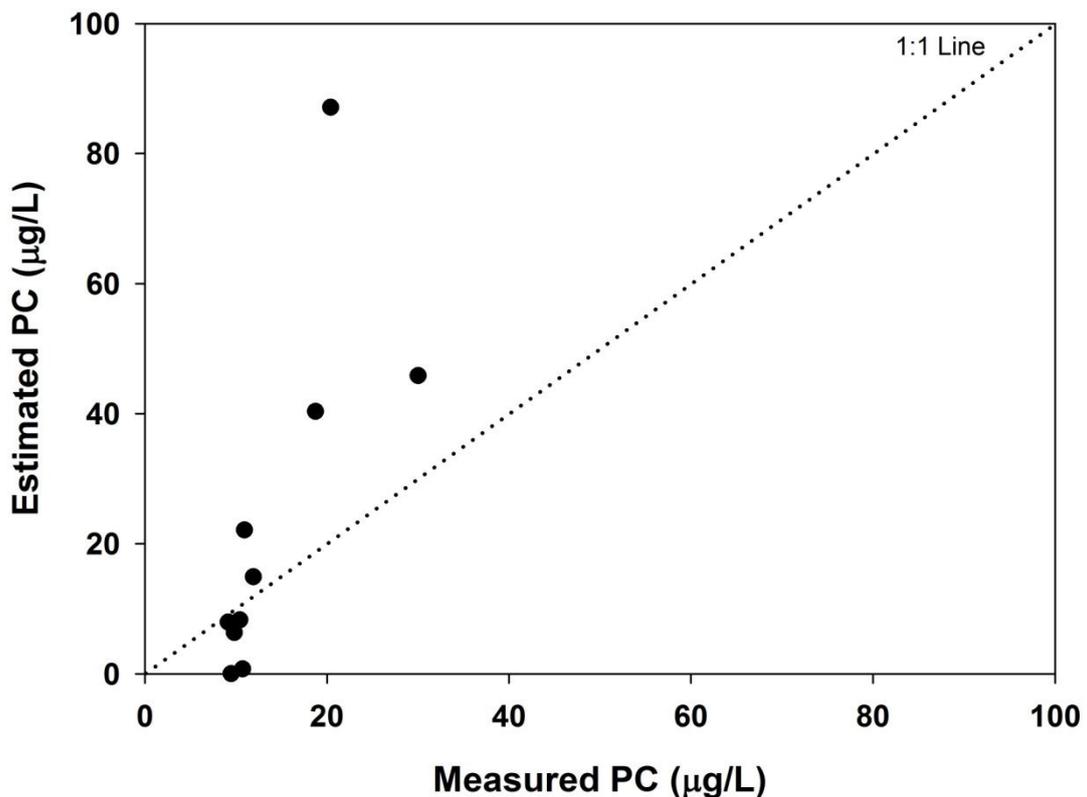
Figure 4.23 - Estimated and measured PC concentration

It was observed that PC concentration estimation from OLCI synthetic dataset underestimated the low concentrations (<10 μg/L) and overestimated the high concentrations (>10 μg/L) as it could be observed, for all points there were an underestimation of PC concentration.

4.8. Uncertainties

The use of QAA for retrieving IOPs showed to be very accurate considering the NRMSE(%) values. However for the purpose of estimating the biological activity the intensity and shape of the estimated IOPs spectra should be similar to the measured ones. Although the modifications for the pQAA, there are few uncertainties on the estimation in the blue spectral channel, which should be explored on the first steps on the estimation of $a(\lambda)$.

However the biggest uncertainties were found on PC concentration estimation due to the lack of $a_{PC}(\lambda)$ measurements. Due to that it was not possible to calculate and calibrate the ψ_1 and ψ_2. Therefore, the error of the algorithm was increased due to the use of a calibration developed for the catfish ponds in the U.S. Therefore, without $a_{PC}(\lambda)$ it was also impossible to calculate the $a_{PC}^{*}(620)$ which was substituted for 0.0019, based on literature reviews. Although these approaches to substitute the $a_{PC}(\lambda)$ and $a_{PC}^{*}(620)$ values got for the hyperspectral dataset an NRMSE of 24.94%, this accuracy could be improved by the use of *in situ* measurements of then.

Besides all these errors from based on the performance of the algorithm, errors from the measured dataset should be also considered on these errors estimators.

Thus considering all sources of errors in the bio-optical modeling, and error of proximally 25% on PC concentration can be considered a good result for the first QAA approach for PC quantification in a tropical inland waters.

5 FINAL CONSIDERATIONS

In this master thesis, a QAA was re-parameterized to retrieve IOPs from a tropical hydroelectric reservoir. It was presented one of the first bio-optical models to retrieve IOPs developed in a Brazilian tropical hydroelectric reservoir. It was also shown an application of a model to retrieve the absorption of PC at 620 nm as well as its application to estimate the concentration of PC in a water column. Although all these procedures were conducted using proximal remote sensing, it was also simulated the application of these techniques to a synthetic dataset of OLCI spectral bands.

Results of this master thesis also include the evaluation of the use of *in vivo* fluorimetry for the quantification of PC concentration comparing the results to the PC concentration estimated from the sonicator method (SARADA et al, 1999), as well as a comparison among PC R_{rs}-based algorithms using 3 datasets and analyzing their sensitivity to chl-*a*. The comparison among R_{rs}-based algorithms showed the influence of not only chl-*a* but also TSS on the R_{rs} at PC absorption range. To minimize these interference on the PC absorption range R_{rs} spectra, it was proposed a filter to decrease the interference of other OACs on this spectral range.

A summary of the results show that the use of *in vivo* fluorimetry for the quantification of PC concentration was compatible for the measured PC concentration using the sonicator method with an R^2 of 0.94. Comparison analysis suggested that although MI09 seemed to be the most sensitive to PC, SI05 got the best validation plots, due to the interference of other OACs at 600 nm. The evaluation of our filter to decrease this interference was satisfactory, showing that for the three algorithms tested in three different datasets the NRMSE was reduced.

The application of QAAv5 and QAA for turbid productive waters to Funil Reservoir dataset was not satisfactory, although they presented a lower NRMSE on the estimation of $a(\lambda)$ and $a_{CDM}(\lambda)$. The estimations of $a_{phy}(\lambda)$ were inaccurate for both methods. Thus the need for a re-parameterization was confirmed and pQAA was developed based on Lee et al. (2009), Lee et al.

(2010) and Mishra et al. (2014). Predicted $a(\lambda)$ from pQAA got an average NRMSE of 36%, while QAAv5 got a NRMSE of 511%, and QAA for turbid productive waters, a NRMSE of 399%. However, not only the NRMSE was lower, but also the spectral shape of the estimated $a(\lambda)$ was closer to the measured one. Predicted $a_{CDM}(\lambda)$ got an average NRMSE of 49%, while QAAv5 and QAA for turbid productive waters got NRMSEs of 885% and 726%, respectively. However, the most impressive result was on the estimation of $a_{phy}(\lambda)$, which got an average NRMSE of 74%, while the NRMSEs for QAAv5 and QAA for turbid productive waters was 9401% and 6911%, respectively.

From the results of the pQAA, we applied the model to estimate $a_{PC}(620)$ developed by Mishra et al. (2013) in order to assess the PC concentration dividing it by its specific absorption. It was applied the same calibration proposed in the work of Mishra et al. (2013), since it was not possible to get *in situ* measures of $a_{PC}(\lambda)$ at Funil Reservoir. Although this lack of *in situ* data, the estimation of PC got an NRMSE of 24.94%. Thus with empirical calibrations of the algorithm, this error tends to be lower.

An important task accomplished in this thesis was the simulation of OLCI spectral bands for the application of the pQAA. Using the Spectral Response Function of OLCI, it was simulated spectral bands 1 to 16 in the range of 400 nm to 800 nm. From this synthetic dataset of OLCI sensor we applied the pQAA. Average NRMSE for $a(\lambda)$, $a_{CDM}(\lambda)$ and $a_{phy}(\lambda)$ estimations were a little higher if compared to the pQAAs applied on the hyperspectral data, with values around 43%, 105% and 478%, respectively. However, the application of Mishra et al. (2013) calibration for the estimation of $a_{PC}(\lambda)$ and further PC concentration were not useful for OLCI synthetic dataset. The NRMSE for PC estimations was 112.49%, enhancing the need to develop a calibration of Mishra et al. (2013) PC's model for OLCI spectral bands.

Future challenges for the QAA modeling in inland waters is the substitution of the spectral bands in the blue range for other ranges (i.e., red and NIR). As described in this Master Thesis, is usually used for atmospheric correction and it has very high spectral response from CDOM and TSS. Therefore the future sensors for water color studies such as OLCI and SABIA-MAR can be

applicable for QAA modeling, since they will have a fine spectral resolution. Moreover, future studies should concentrate not only in the development of algorithms for remotely estimation of biogeochemical components, but also in the response of biological activities according to their life cycles and differences. One good example of an application of this understanding of the life cycles in the cyanobacteria remote sensing is the detection of a signal which allows the identification of cyanobacteria population growth in its early stages. If there is a difference on the spectral response of cyanobacteria in their early life, it will be possible to establish an early warning system for water quality. Nevertheless, more studies should be developed aiming the understanding of IOPs' behavior in tropical inland aquatic systems, mainly in the ones near urban centers, which are essential for the water supply of big cities.

To conclude, I hope this master thesis is merely the first of many to explore the re-parameterization of semi and quasi-analytical models for the accurate estimation of IOPs and biological activity on tropical inland waters. Although it is a new and still in development area of knowledge, it is important to develop remote sensing studies of water quality due to the significant number of Lakes and Reservoirs in Brazil. Its importance is not restricted to the scientific community, but includes policy makers and environmental managers, who would be given a trustful tool for improving water governance.

BIBLIOGRAPHIC REFERENCES

ARAÚJO, J.R.S.; MOURA, W.O.R.; NUNAN, G.W. **Avaliação ambiental do rio Paraíba do Sul** - Trecho Funil - Santa Cecília. Rio de Janeiro: Instituto Estadual do Ambiente (INEA), 2010. (Technical Report in Portuguese).

AUSTIN, R.W.; HALIKAS, G. **The index of refraction of seawater**. La Jolla, CA, USA: Visibility Laboratory - Scripps Institute of Oceanography, 1976.

AUSTIN, R.W. Gulf of Mexico, ocean-color surface-truth measurements. **Boundary-Layer Meteorology**, v. 18, n. 3, p. 269-285, 1980.

AZEVEDO, S.M.F.O.; CARMICHAEL, W.W.; JOCHIMSEN, E.M.; RINEHART, K.L.; LAU, S.; SHAW, G.R.; EAGLESHAM, G.K. Human intoxication by microcystins during renal dialysis treatment in Caruaru - Brazil. **Toxicology**, n. 181-182, p. 441 - 446, 2002.

BENNETT, A.; BOGORAD, L. Complementary chromatic adaptation in a filamentous blue-green alga. **Journal of Cell Biology**, v. 58, p. 419-435, 1973.

BEUTLER, M.; WILTSHIRE, K.H.; MEYER, B.; MOLDAENKE, C.; LÜRING, C.; MEYERHÖFER, M.; HANSEN, U.-P.; DAU, H. A fluorometric method for the differentiation of algal populations in vivo and in situ. **Photosynthesis Research**, v. 72, p. 39–53, 2002.

BRANCO, C.W.C.; ROCHA, M.I.A; PINTO, G.F.S.; GÔMARA, G.A.; FILIPPO, R. Limnological features of Funil Reservoir (R.J., Brazil) and indicator properties of rotifers and cladocerans of the zooplankton community. **Lakes & Reservoirs: Research and Management**, v. 7, p. 87 - 92, 2002.

BUKATA, R.P.; JEROME, J.H.; BRUTON, J.E.; JAIN, S.C. Determination of inherent optical properties of Lake Ontario coastal waters. **Applied Optics**, v. 18, n. 23, p. 3926 - 3932, 1979.

BUKATA, R.P.; JEROME, J.H.; BRUTON, J.E.; JAIN, S.C.; ZWICK, H. H. Optical water quality model of Lake Ontario. 1: determination of the optical

cross sections of organic and inorganic particulates in Lake Ontario. **Applied Optics**, v. 20, n. 09, p. 1696 - 1703, 1981a.

BUKATA, R.P.; BRUTON, J.E.; JEROME, J.H.; JAIN, S.C.; ZWICK, H. H. Optical water quality model of Lake Ontario. 2: determination of chlorophyll a and suspended mineral concentrations of natural waters from submersible and low altitude optical sensors. **Applied Optics**, v. 20, n. 09, p. 1704 - 1714, 1981b.

BUKATA, R.P. **Satellite monitoring of Inland and coastal water quality:** retrospection, introspection, future directions. Boca Raton, FL: Taylor & Francis Group, 2005.

BUKATA, R.P. Retrospection and introspection on remote sensing of inland water quality: "Like Déjà Vu All Over Again". **Journal of Great Lakes Research,** v. 39, n. supplement, p. 2 - 5, 2013.

CARMICHAEL, W.W.; AZEVEDO, S.M.F.O.; AN, J.S.; MOLICA, R.J.R.; JOCHIMSEN, E.M.; LAU, S.; RINEHART, K.L.; SHAW, G.R.; EAGLESHAM, G.K. Human fatalities from cyanobacteria: chemical and biological evidence for cyanotoxins. **Environmental Health Perspectives**, v. 109, n. 7, p. 663 - 668, 2001.

CHAMON, M.A. **The SABIA-Mar Mission**. International Ocean Colour Coordinating Group (IOCCG), 2013. Available at: <http://www.ioccg.org/sensors/Chamon_SABIA_MAR.pdf>. Accessed at: 6th of November of 2013.

CLEVERS, J.G.P.W.; GITELSON, A.A. Remote estimation of crop and grass chlorophyll and nitrogen content using red-edge bands on Sentinel-2 and -3. **International Journal of Applied Earth Observation and Geoinformation**, v. 23, p. 344 - 351, 2013.

CODD, G. A.; CHORUS, I.; BURCH, M. D. Design of monitoring programmes. In: CHORUS, I.; BARTRAM, J. (Ed.). **Toxic cyanobacteria in water**: a guide to their public health consequences, monitoring and management. London: UNESCO/WHO/UNEP, 1999. Chapter 10, p.290-305.

COX, C.; MUNK, W. Measurement of the roughness of the sea surface from photographs of the sun's glitter. **Journal of the Optical Society of America**, v. 44, n. 11, p. 838 - 850, 1954.

DEKKER, A.G. **Detection of optical water quality parameters for eutrophic waters by high resolution remote sensing**. 1993. 222 p. PhD. Thesis. Vrije Universiteit, 1993.

DEKKER, A.G.; HESTIR, E.L. **Evaluating the feasibility of systematic inland water quality monitoring with satellite remote sensing**. Melbourne, Australia: CSIRO: Water for a Healthy Country National Research Flagship, 2012.

DONLON, C.; BERRUTI, B.; BUONGIORNO, A.; FERREIRA, M.H.; FEMENIAS, P.; FRERICK, J.; GORYL, P.; KLEIN, U.; LAUR, H.; MAVROCORDATOS, C.; NIEKE, J.; REDHAN, H.; SEITZ, B.; STROEDE, J.; SCIARRA, R. The Global Monitoring for Environment and Security (GMES) Sentinel-3 mission. **Remote Sensing of Environment**, v. 120, p. 37-57, 2012.

DOMÍNGUEZ-GÓMEZ, J.A.; ALONSO-ALONSO, C.; ALONSO-GARCÍA, A. Remote sensing as a tool for monitoring water quality parameters for Mediterranean Lakes of European Union water framework directive (WFD) and as a system of surveillance of cyanobacterial harmful algae blooms (SCyanoHABs). **Environment Monitoring and Assessment**, v. 181, p. 317 - 334, 2011.

ENVIRONMENTAL PROTECTION AGENCY (EPA). **Methods for chemical analysis of water and wastes.** Washington, DC: USEPA, 1983. 460 p.

EUROPEAN SPACE AGENCY (ESA). **Sentinel‑3:** ESA's Global Land and Ocean Mission for GMES Operational Services. Fletcher, K. (Ed.) Noordwijk, NL: ESA Communications, 2012.

FALCONER, I.R.; HUMPAGE, A.R. Cyanobacterial (blue-green algal) toxins in water supplies: Cylindrospermopsins. **Environmental Toxicology**, v. 21, n. 4, p. 299-304, 2006.

FERRÃO-FILHO, A.S.; SOARES, M.C.; ROCHA, M.I.A.; MAGALHÃES, V.F.; AZEVEDO, S.M.F.O. Florações de Cianobactérias tóxicas no Reservatório do Funil: dinâmica sazonal e consequências para o zooplâncton. **Oecologia Brasiliensis**, v. 13, n. 2, p.346 - 365, 2009.

FERREIRA, R.D.; BARBOSA, C.C.F.; NOVO, E.M.L.M. Assessment of in vivo fluorescence method for chlorophyll-a estimation in optically complex waters (Curuai floodplain, Pará – Brazil). **Acta Limnologica Brasilensia**, v. 24, n.4, p. 373-386, 2012.

FRANCIS, G. Poisonous Australian Lake. **Nature**, v. 18, p. 11-12, 1878.

GITELSON, A.A.; DALL'OLMO, G.; MOSES, W.; RUNDQUIST, D.C.; BARROW, T.; FISHER, T.R.; GURLIN, D.; HOLZ, J. A simple semi-analytical model for remote estimation of chlorophylla in turbid waters: validation. **Remote Sensing of Environment**, v. 112, p. 3582 - 3593, 2008.

GONS, H. J. Optical teledetection of chlorophyll a in turbid inland waters. **Environmental Science and Technology**, v. 33, p. 1127-1132, 1999.

GORDON, H.R.; BROWN, O.B.; JACOBS, M.M. Computed relationships between the inherent and apparent optical properties of a flat homogeneous ocean. **Applied Optics**, v. 14, n. 2, 1975.

GORDON, H.R.; BROWN, O.B.; EVANS, R.H.; BROWN, J.W.; SMITH, R.C.; BAKER, K.S.; CLARK, D.K. A Semianalytic radiance model of ocean color. **Journal of Geophysical Research**, v. 93, n. D9, p. 10909 - 10924, 1988.

GORDON, H.; MOREL, A. **Remote Assessment of Ocean Color for Interpretation of Satellite Visible Imagery: A Review.** New York: Springer Verlag, 1983. Lecture Notes on Coastal and Estuarine Studies, v. 4.

HOBI LABS. **HydroScat-6P backscattering sensor & fluorometer user's manual**. Revision J, Tucson, AZ, USA: Hydro-Optics, Biology, & Instrumentation Laboratories, 2010.

HOBI LABS. **HydroScat-6p backscattering Sensor - fluorometer**: overview. Tucson, AZ, USA: Hydro-Optics, Biology, & Instrumentation Laboratories, 1998-2012. Available at: <http://www.hobilabs.com/cms/index.cfm/37/152/1253/1266/index.html>. Accessed at: 6th of November of 2013.

HOULIEZ, E.; LIZON, F.; THYSSEN, M.; ARTIGAS, L.F.; SCHMITT, F.G. Spectral fluorometric characterization of Haptophyte dynamics using the FluoroProbe: an application in the eastern English Channel for monitoring Phaeocystis globosa. **Journal of Plankton Research**, v. 34, n.2, p. 136 - 151, 2012.

HUNTER, P.D.; TYLER, A.N.; PRÉSING, M.; KOVÁCS, A.W.; PRESTON, T. Spectral discrimination of phytoplankton colour groups: The effect of suspended particulate matter and sensor spectral resolution. **Remote Sensing of Environment**, v. 112, p. 1527 - 1544, 2008.

HUNTER, P.D.; TYLER, A.N.; GILVEAR, D.J.; WILLBY, N.J. Using remote sensing to aid the assessment of human health risks from blooms of potentially toxic cyanobacteria. **Environmental Science & Technology**, v. 43, p. 2627–2633, 2009.

HUNTER, P.D.; TYLER, A.N.; CARVALHO, L.; CODD, G.A.; MABERLY, S.C. Hyperspectral remote sensing of cyanobacterial pigments as indicators for cell populations and toxins in eutrophic lakes. **Remote Sensing of Environment**, v. 114, p. 2705–2718, 2010.

INTERNATIONAL OCEAN-COLOUR COORDINATING GROUP (IOCCG). **Sentinel 3 overview**, B3thesda, USA: IOCCG, 2010.

JENSEN, J.R. **Remote sensing of the environment**: an earth resource perspective. 2. ed. Upper Saddle River, NJ: Prentice Hall, 2007. 592 p.

JERLOV, N.G. **Optical oceanography**. Amsterdam: Elsevier, 1968. 194 p. Elsevier Oceanographic Series, v. 5.

JERLOV, N.G. **Marine optics**. Amsterdam: Elsevier, 1976. 231 p. Elsevier Oceanographic Series, v. 14.

KHORRAM, S.; CHESHIRE, H.; GERACI, A. L.; LA ROSA, G. Water quality mapping of Augusta Bay, Italy from Landsat-TM data. **International Journal of Remote Sensing,** v.12, p. 803-808, 1991.

KIRK, J.T.O. **Light & photosynthesis in aquatic ecosystems**. Melbourne: Cambridge University Press, 1994. 509 p.

KUTSER, T. Quantitative detection of chlorophyll in cyanobacterial blooms by satellite remote sensing. **Limnology and Oceanography**, v. 49, p. 2179–2189, 2004.

LABATE, D.; CECCHERINI, M.; CISBANI, A.; DE COSMO, V.; GALEAZZI, C.; GIUNTI, L.; MELOZZIM M.; PIERACCINI, S.; STAGI, M. The PRISMA payload optomechanical design, a high performance instrument for a new hyperspectral mission. **Acta Astronautica**, v. 65, p. 1429 - 1436, 2009.

LE, C.; LI, Y.; ZHA, Y.; SUN, D.; HUANG, C.; LU, H. A four-band semi-analytical model for estimating chlorophyll a in highly turbid lakes: the case of Taihu Lake, China. **Remote Sensing of Environment,** v. 113, p. 1175-1182, 2009.

LE, C.; LI, Y.; ZHA, Y.; WANG, Q.; ZHANG, H.; YIN, B. Remote sensing of phycocyanin pigment in highly turbid inland waters in Lake Taihu, China. **International Journal of Remote Sensing**, v.32, n. 23, p. 8253-8269, 2011.

LEE, Z.; CARDER, K.L.; ARNONE, R.A. Deriving inherent optical properties from water color: a multiband quasi-analytical algorithm for optically deep waters. **Applied Optics**, v. 41, n. 27, p. 5755-5772, 2002.

LEE, Z.; LUBAC, B.; WERDELL, J.; ARNONE, A. **An update of the Quasi-Analytical Algorithm (QAA_v5)**, IOCCG, 2009. Available at: http://www.ioccg.org/groups/Software_OCA/QAA_v5.pdf

LEE, Z.P.; ARNONE, R.; HU, C.; WERDELL, J.; LUBAC, B. Uncertainties of optical parameters and their propagations in an analytical ocean color inversion algorithm. **Applied Optics**, v. 49, p. 369 - 381, 2010.

LI, LINHAI; LI, LIN.; SHI, K.; LI, ZUCHUAN; SONG, K. A semi-analytical algorithm for remote estimation of phycocyanin in inland waters. **Science of the Total Environment**, v. 435-436, p. 141 – 150, 2012.

LI, LINHAI; LI, LIN; SONG, K.; LI, Y.; TEDESCO, L.P.; SHI, K.; LI, Z. An inversion model for deriving inherent optical properties of inland waters: Establishment, validation and application. **Remote Sensing of Environment**, v. 135, p. 150-166, 2013.

LORENZEN, C.J. Determination of chlorophyll and pheo-pigments: Spectrophotometric equations. **Limnology and Oceanography**, v. 12, 343 - 346, 1967.

LUND, J.W.G.; KIPLING, C.; LE CREN, E.D. The inverted microscope method of estimating algal numbers and the statistical basis of estimations by counting. **Hydrobiology**, v. 11, p. 143 - 170, 1958.

MAFFIONE, R.A.; DANA, D.R. Instruments and methods for measuring the backward-scattering coefficient of ocean waters. **Applied Optics**, v. 36, n. 24, p. 6057 - 6067, 1997.

MARITORENA, S.; SIEGEL, D.A.; PETERSON, A.R. Optimization of a semianalytical ocean color model for global-scale applications. **Applied Optics**, v. 41, n. 15, p. 2705-2714, 2002.

MARTIN, J. L.; McCUTCHEON, S. C. **Hydrodynamics and transport for water quality modeling**. Boca Raton, USA: Lewis Publishers, 1999.

METSAMAA, L.; KUTSER, T.; STROMBECK, N. Recognising cyanobacterial blooms based on their optical signature: a modelling study. **Boreal Environment Research**, v.11, p. 493-506, 2006.

MISHRA, D.R.; NARUMALANI, S.; RUNDQUIST, D.; LAWSON, M. Characterizing the vertical diffuse attenuation coefficient for downwelling irradiance in coastal waters: Implications for water penetration by high resolution satellite data. **ISPRS Journal of Photogrammetry & Remote Sensing**, v. 60, p. 48-64, 2005.

MISHRA, S. **Remote sensing of harmful algal bloom**. 2012. Ph.D. Thesis, Mississippi State University, Mississippi State, MS, USA, 2012.

MISHRA, S.; MISHRA, D. R.; SCHLUCHTER, W. M. A Novel algorithm for predicting phycocyanin concentrations in cyanobacteria: a proximal hyperspectral remote sensing approach. **Remote Sensing**, v.1, p. 758-775, 2009.

MISHRA, S.; MISHRA, D.R.; LEE, Z.; TUCKER, C.S. Quantifying cyanobacterial phycocyanin concentration in turbid productive waters: a quasi-analytical approach. **Remote Sensing of Environment**, v. 133, p. 141–151, 2013.

MISHRA, S.; MISHRA, D.R.; LEE, Z. Bio-optical inversion in highly turbid and cyanobacteria dominated waters. **IEEE Transactions in Geosciences and Remote Sensing**, v. 52, n.1, p. 375 - 388, 2014.

MOBLEY, C. D. Estimation of the remote-sensing reflectance from above-surface measurements. **Applied Optics**, v. 38, n. 36, p. 7442-7455, 1999.

MOBLEY, C. Radiative transfer in the ocean. In: STEELE, J.H. **Encyclopedia of ocean sciences**. London: Academic Press Elsevier, 2001. p. 2321-2330.

MOBLEY, C.D.; STRAMSKI, D.; BISSETT, W.P.; BOSS, E. Optical modeling of ocean waters: Is the Case 1 - Case 2 classification still useful? **Oceanography,** v. 17, n. 2, p. 60-67, 2004.

MOREL, A.; PRIEUR, L. Analysis of variation in ocean colour. **Limnology and Oceanography**, v. 22, p. 709-722, 1977.

MOREL, A.; GORDON, H.R. Report of the working group on water color. **Boundary-Layer Meteorology**, v. 18, n. 4, p. 343-355, 1980.

MOREL, A. Bio-optical models. In: STEELE, J.H. **Encyclopedia of ocean sciences**. London: Academic Press Elsevier, 2001. p.317-326.

MUELLER, J.L. In-water radiometric profile measurements and data analysis protocols. In: FARGION, G. S.; MUELLER, J. L.(eds.). **Ocean optics protocols for satellite ocean color sensor validation**. Greenbelt, Maryland: Goddard Space Flight Center, 2000. p. 87-97. NASA Tech. Memo. 2000209966/Rev2.

NATIONAL RESEARCH COUNCIL (NCR). **The drama of the commons**. Washington, DC: National Academy Press, 2002. ISBN 0-309-08250-1.

NATIONAL RESEARCH COUNCIL (NCR). **Earth science and applications from space:** national imperatives for the next decade. Washington, DC: National Academy Press. Division on Engineering and Physical Sciences, 2007. 456 p.

NUSH, E.A. Comparison of different methods for chlorophyll and phaeopigment determination. **Archiv für Hydrobiologie–Beiheft Ergebnisse der Limnologie**, v. 14, p. 14 - 36, 1980.

OHDE, T.; SIEGEL, H. Derivation of immersion factors for the hyperspectral TriOS radiance sensor. **Journal of Optics A: Pure and Applied Optics**, v. 5, p. L12–L14, 2003.

OGASHAWARA, I.; MISHRA, D.R.; MISHRA, S.; CURTARELLI, M.P.; STECH, J.L. A performance review of reflectance based algorithms for predicting phycocyanin concentrations in inland waters. **Remote Sensing**, v. 5, p . 4774 - 4798, 2013.

OGASHAWARA, I.; ZAVATTINI, J.A.; TUNDISI, J.G. The climatic rhythm and blooms of cyanobacteria in a tropical reservoir in São Paulo, Brazil. **Brazilian Journal of Biology**, v.1, 2014. (in press).

OSTROM, E.; STERN, P.C.; DIETZ, T. Water rights in the commons. **Water Resources IMPACT,** v. 5, n. 2, p. 9-12, 2003.

PETZOLD, T.J. **Volume scattering functions for selected ocean waters.** Ref. 72-28. San Diego: Scripps Institute of Oceanography, University of California, 1972. 79 p.

PLATT, T.; HOEPFFNER, N.; STUART, V.; BROWN, C. (eds.). **Ocean colour**? The societal benefits of ocean-colour technology. Dartmouth, Canada: IOCCG, 2008. Reports of the International Ocean-Colour Coordinating Group, No. 7.

POST, A.F.; WIT, R.; MUR, L.R. Interactions between temperature and light intensity on growth and photosynthesis of the cyanobacterium Oscillatoria agardhii. **Journal of Plankton Research**, 7, 487-495, 1985.

PREISENDORFER, R.W. **Hydrologic optics**, Vol. II: Foundations. Washington, D.C.: U.S. Dept. of Commerce, 1976.

PRIMO, A.R.R. **Avaliação da influência do reservatório de Funil na qualidade da água do rio Paraíba do Sul**. 2006. 109 p. Master Thesis (Mestrado em Química Analítica) - Universidade de São Paulo, São Paulo, 2006. (in Portuguese)

RANDOLPH, K.; WILSON, J.; TEDESCO, L.; LI, L.; PASCUAL, D.P.; SOYEUX, E. Hyperspectral remote sensing of cyanobacteria in turbid productive water using optically active pigments, chlorophyll a and phycocyanin. **Remote Sensing of Environment**, v. 112, p. 4009-4019, 2008.

REES, W.G. **Physical principles of remote sensing.** Cambridge, England: Cambridge University Press, 2001.

REINART, A.; KUTSER, T. Comparison of different satellite sensors in detecting cyanobacterial bloom events in the Baltic Sea. **Remote Sensing of Environment**, v. 102, p. 74 - 85, 2006.

REYNOLDS, C.S. **Ecology of phytoplankton**. Cambrigde: Cambrigde University Press, 2006. 535p.

ROBERTS, D.A.; QUATTROCHI, D.A.; HULLEY, G.C.; HOOK, S.J.; GREEN, R.O. Synergies between VSWIR and TIR data for the urban environment: An evaluation of the potential for the Hyperspectral Infrared Imager (HyspIRI) Decadal Survey mission. **Remote Sensing of Environment**, v. 117, p. 83 - 101, 2012.

ROCHA, M.I.A.; BRANCO, C.W.C.; SAMPAIO, G.F.; GÔMARA, G.A.; FILIPPO, R. Spatial and temporal variation of limnological features, Microcystis aeruginosa and zooplankton in a eutrophic reservoir (Funil Reservoir, Rio de Janeiro). **Acta Limnologica Brasilensia**, v. 14, p. 73 - 86, 2002.

ROESLER, C.S.; PERRY, M.J. In situ phytoplankton absorption, fluorescence emission, and particulate backscattering spectra determined from reflectance. **Journal of Geophysical Research**, v. 100, p. 13279-13294, 1995.

RUIZ-VERDÚ, A.; SIMIS, S.G.H.; HOYOS, C.; GONS, H.J.; PEÑA-MARTÍNEZ, R. An evaluation of algorithms for the remote sensing of cyanobacterial biomass. **Remote Sensing of Environment**, v. 112, p. 3996-4008, 2008.

SARADA, R.; PILLAI, M.G.; RAVISHANKER, G.A. Phycocyanin from Spirulina sp: Influence of processing of biomass on phycocyanin yield, analysis of efficacy of extraction methods and stability studies on phycocyanin. **Process Biochemistry**, v. 34, p. 795–801, 1999.

SCHALLES, J.F.; YACOBI, Y.Z. Remote detection and seasonal patterns of phycocyanin, carotenoid, and chlorophyll pigments in eutrophic waters. **Archives Hydrobiologica Special Issues on Advanced Limnology**, v. 55, p. 153-168, 2000.

SIMIS, S.G.H.; PETERS, S.W.M.; GONS, H.J. Remote sensing of the cyanobacterial pigment phycocyanin in turbid inland water. **Limnology and Oceanography**, v. 50, p. 237−245, 2005.

SIMIS, S.G.H.; RUIZ-VERDU, A.; DOMINGUEZ-GOMEZ, J.A.; PENA-MARTINEZ, R.; PETERS, S.W.M.; GONS, H.J. Influence of phytoplankton pigment composition on remote sensing of cyanobacterial biomass. **Remote Sensing of Environment**, v. 106, p. 414 – 427, 2007.

SIVONEN, K.; JONES, G. Cyanobacterial Toxins. In: CHORUS, I.; BARTRAM, J. (Ed.). **Toxic cyanobacteria in water:** a guide to their public health consequences, monitoring and management. London, England: UNESCO/WHO/UNEP, 1999, Chapter 3, p.55-124.

SMITH, R.C.; BAKER, K.S. **The bio-optical state if ocean waters and remote sensing**. La Jolla, Scripps Institution of Oceanography, 1977, p. 36.

SONG, K.; LI, L.; LI, S.; TEDESCO, L.; HALLA, B.; LI, Z. Hyperspectral retrieval of phycocyanin in potable water sources using genetic algorithm–partial least squares (GA–PLS) modeling. **International Journal of Applied Earth Observation and Geoinformation**, v. 18, p. 368 - 385, 2012.

SONG, K.; LI, L.; LI, Z.; TEDESCO, L.; HALL, B.; SHI, K. Remote detection of cyanobacteria through phycocyanin for water supply source using three-band model. **Ecological Informatics**, v. 15, p. 22 - 33, 2013a.

SONG, K.;LI, L.; TEDESCO, L.P.; LI, S.; DUAN, H.; LIU, D.; HALL, B.E.; DU, J.; LI, Z.; SHI, K.; ZHAO, Y. Remote estimation of chlorophyll-a in turbid inland waters: three-band model versus GA-PLS model. **Remote Sensing of Environment**, v. 136, p. 342 - 357, 2013.

STUFFLER, T.; FÖRSTER,K.; HOFER, S.; LEIPOLD, M.; SANG, B.; KAUFMANN, H.; PENNÉ, B.; MUELLER, A.; CHLEBEK, C. Hyperspectral imaging—An advanced instrument concept for the EnMAP mission (Environmental Mapping and Analysis Programme). **Acta Astronautica**, v. 65, n. 7 - 8, p.1107 - 1112, 2009.

SUN, D.; LI, Y.; WANG, Q.; GAO, J.; LE, C. ; HUANG, C.; GONG, S. Hyperspectral Remote Sensing of the Pigment C-Phycocyanin in Turbid Inland Waters, Based on Optical Classification. **IEEE Transactions on Geoscience and Remote Sensing,** v. 51, n. 7, p. 3871 - 3884, 2013.

TASSAN, S.; FERRARI, G. An alternative approach to absorption measurements of aquatic particles retained on filters. **Limnology and Oceanography**, v. 40, p. 1358 - 1368, 1995.

TRIOS. **TriOS - optical sensors - Ramses**. Oldenburg, Germany: TriOS GmbH, 2009-2013. Available at: <http http://www.trios.de/index.php?option=com_content&view=category&id=47&layout=trios&Itemid=76#item196_top>. Accessed at: 6th of Nov of 2013.

TUNDISI, J.G; MATSUMURA-TUNDISI, T; ARANTES JUNIOR, J.D; TUNDISI, J.E; MANZINI, N.F.; DUCROT, R. The response of Carlos Botelho (Lobo, Broa) reservoir to the passage of cold fronts as reflected by physical, chemical, and biological variables. **Brazilian Journal of Biology**, v. 64, n. 1, p. 177 - 186, 2004.

TUNDISI, J.G.; MATSUMURA-TUNDISI, T.; PEREIRA, K.C.; LUZIA, A.P.; PASSERINI, M.D.; CHIBA, W.A.C.; MORAIS, M.A.; SEBASTIEN, N.Y. Cold fronts and reservoir limnology: an integrated approach towards the ecological dynamics of freshwater ecosystems. **Brazilian Journal of Biology**, v. 70, n. 3, p. 815 - 824, 2010.

TURNER DESIGNS, **MODEL 10-AU-005-CE fluorometer user's manual.** Sunnyvale, California: Turner Designs Inc., 2009.

UNITED NATIONS ENVIRONMENTAL PROGRAM (UNEP). **Planning and Management of Lakes and reservoirs**: an integrated approach to eutrophication. Osaka/Shiga, Japan: International Environmental Technology Center, 1999, 375 p. Technical Publication Series 11.

VINCENT, R.K.; QIN, X.; McKAY, R.M.L.; MINER, J.; CZAJKOWSKI, K.; SAVINO, J.; BRIDGEMAN, T. Phycocyanin detection from LANDSAT TM data for mapping cyanobacterial blooms in Lake Erie. **Remote Sensing of Environment**, v. 89, p. 381 - 392, 2004.

WANG, L.; LIU, L.; ZHENG, B. Eutrophication development and its key regulating factors in a water-supply reservoir in North China. **Journal of Environmental Sciences**, v. 25, n. 5, p. 962 - 970, 2013.

WETZEL, R. G.; LIKINS, G. E. **Limnological analyses.** 2. ed. New York, USA: Springer, 1991.

WHEELER, S.M.; MORRISSEY, L.A.; LEVINE, S.N.; LIVINGSTON, G.P.; VINCENT, W.F. Mapping cyanobacterial blooms in Lake Champlain's Missisquoi Bay using QuickBird and MERIS satellite data. **Journal of Great Lakes Research**, v. 38, p. 68 - 75, 2012.

WORLD HEALTH ORGANIZATION (WHO). **Cyanobacterial toxins**: microcystin-LR in drinking water. Geneva, Switzerland: World Health Organization, 2003.

WILLEN, E. A simplified method of phytoplankton counting. British **Phycological Journal**, v. 11, p. 265 - 278, 1976.

WYNNE, T.T.; STUMPF, R.P.; TOMLINSON, M.C.; WARNER, R.A.; TESTER, P.A.; DYBLE, J.; FAHNENSTIEL, G.L. Relating spectral shape to cyanobacterial blooms in the Laurentian Great Lakes. **International Journal of Remote Sensing**, v. 29, n. 12, p. 3665 - 3672, 2008.

WYNNE, T.T.; STUMPF, R.P.; TOMLINSON, M.C.; DYBLE, J. Characterizing a cyanobacterial bloom in western Lake Erie using satellite imagery and meteorological data. **Limnology and Oceanography**, v. 55, n. 5, p. 2025 - 2036, 2010.

APPENDIX A

Model	Reference	Sensor	Algorithm
Empirical	Vincent (2004)	TM and ETM+	$PC = 47.7 - 9.21(TMR3/TMR1) + 29.7(TMR4/TMR1)$ $- 118(TMR4/TMR3) - 6.819.21(TMR5/TMR3)$ $+ 41.9(TMR7/TMR3) - 14.7(TMR7/TMR4)$
Empirical	Song, Kaishan et al. (2012)	AISA	GA-PLS of (713/647; 704/628; 694/638; FDR713; FDR713; R_{rs}628)
Empirical	Song, Kaishan et al. (2013)	ASD FieldSpec / Ocean Optics	$PC \propto [R_{rs}^{-1}(622) - R_{rs}^{-1}(691)] \cdot R_{rs}(740)$
Empirical	Sun et al. (2012)	FieldSpec spectroradiometer	Type 3 waters (765/268; 765/623; 804/628; 820/628; 765/609)
Semi-Empirical	Dekker (1993)	CAESAR / CASI	$PC \propto [R_{rs}(600) + R_{rs}(648)] - R_{rs}(624)$
Semi-Empirical	Schalles and Yacobi (2000)	Ocean Optics	$PC \propto R_{rs}(650)/R_{rs}(625)$
Semi-Empirical	Simis et al. (2005)	MERIS	$PC \propto \left\{ \left[\frac{R_{rs}(709)}{R_{rs}(620)} \times (a_w(709) + b_b) - b_b - a_w(620) \right] - 0.24 a_{ph}(665) \right\}$
Semi-Empirical	Wynne et al. (2008)	MERIS	$SS = nL_w(681) - nL_w(665) - \{nL_w(709) - nL_w(665)\} \frac{(681 - 665)}{(709 - 665)}$
Semi-Empirical	Hunter et al. (2008)	ASD FieldSpec	$PC \propto [R_{rs}^{-1}(630) - R_{rs}^{-1}(660)] \cdot R_{rs}(750)$
Semi-Empirical	Mishra et al. (2009)	Ocean Optics	$PC \propto R_{rs}(700)/R_{rs}(600)$
Semi-Empirical	Hunter et al. (2010)	AISA / CASI-2	$PC \propto [R_{rs}^{-1}(615) - R_{rs}^{-1}(600)] \cdot R_{rs}(725)$
Semi-Empirical	Le et al. (2011)	ASD FieldSpec	$PC \propto [R_{rs}^{-1}(630) - R_{rs}^{-1}(645)][R_{rs}^{-1}(730) - R_{rs}^{-1}(694)]^{-1}$
Semi-Empirical	Dash et al. (2011)	Ocean Color Monitor	$PC \propto OCMR_{rs}(556.4) - OCMR_{rs}(669)/[556.4 - 669]$
Semi-Empirical	Dominguez et al. (2011)	MERIS / CHRIS	$PC \propto (MB9 - MB7)/(MB9 + MB7)$
Semi-Empirical	Wheeler et al. (2012)	QuickBird	$PC \propto QBNIR/QBRed$
Semi-Analytical	Li, Linhai et al. (2012)	OceanOpticsUSB4000	$a_{pc}(624) = a_{ph}(624) - 0.5 \times [a_{ph}(600) + a_{ph}(648)]$
QAA	Mishra et al. (2013)	Ocean Optics	$a_{PC}(620) = \dfrac{\varphi_1 a_{ph}(620) - a_{ph}(665)}{\varphi_1 - \varphi_2}$

Where: TRM is Landsat TM Radiance; FDR is the first derivative; nL_w is the normalized water leaving radiance; $OCMR_{rs}$ is the R_{rs} from OCM sensor; MB is MERIS band; QBNIR is the Quickbird NIR channel and QBRed is the Quickbird red channel; φ_1 is the ratio between $a_{chl}(665)$ and $a_{chl}(620)$ and φ_2 is the ratio between $a_{PC}(665)$ and $a_{PC}(620)$.

APPENDIX B

Figure A.1 shows the estimated and measured $a(\lambda)$, $a_{CDM}(\lambda)$ and $a_{phy}(\lambda)$ spectra for point 1.
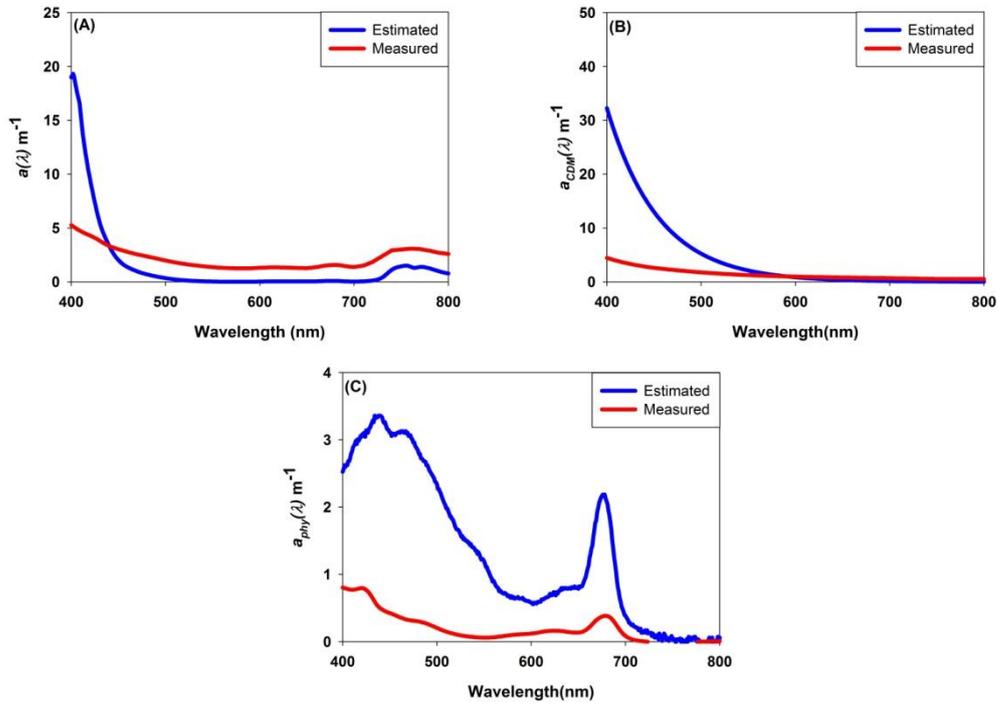

Figure A.1 - Estimated and measured absorption spectra; a) a(λ) with a NRMSE of 0.77%; b) $a_{CDM}(\lambda)$ with a NRMSE of 1.85%; and $a_{phy}(\lambda)$ with a NRMSE of 1.80%.

Figure A.2 shows the estimated and measured $a(\lambda)$, $a_{CDM}(\lambda)$ and $a_{phy}(\lambda)$ spectra for point 2.
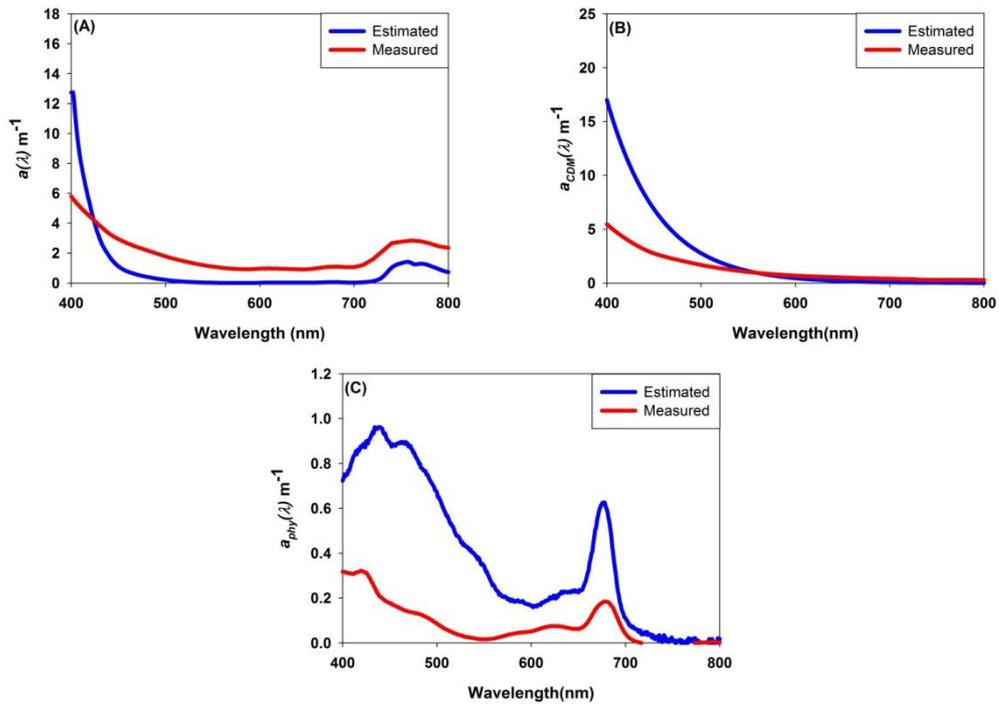

Figure A.2 - Estimated and measured absorption spectra; a) a(λ) with a NRMSE of 0.34%; b) $a_{CDM}(\lambda)$ with a NRMSE of 0.56%; and $a_{phy}(\lambda)$ with a NRMSE of 1.17%.

Figure A.3 shows the estimated and measured $a(\lambda)$, $a_{CDM}(\lambda)$ and $a_{phy}(\lambda)$ spectra for point 3.
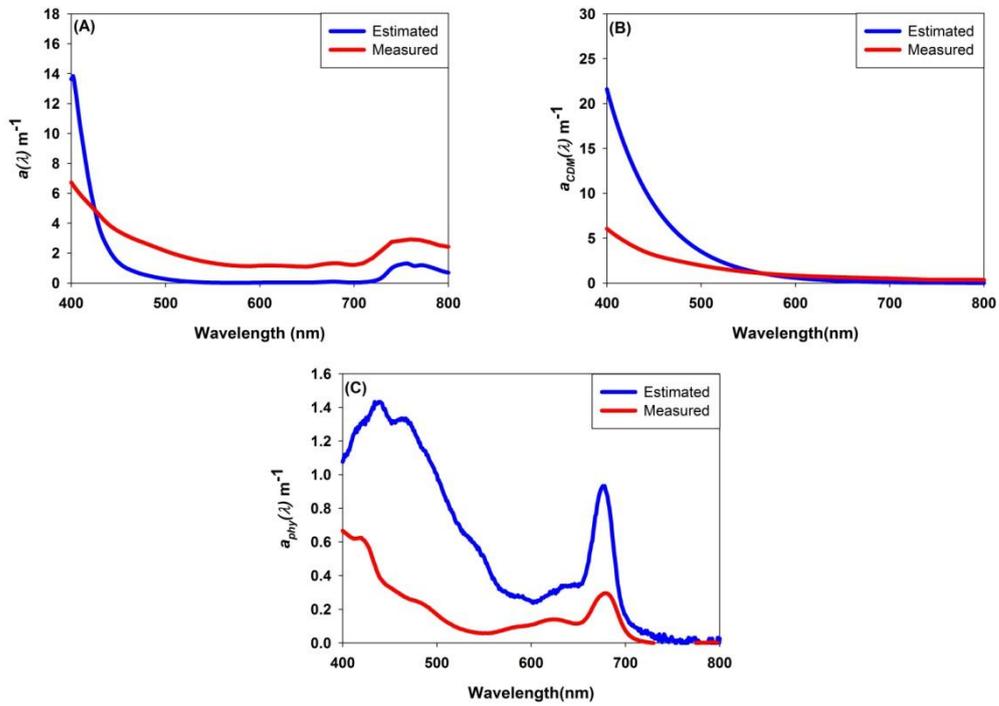

Figure A.3 - Estimated and measured absorption spectra; a) $a(\lambda)$ with a NRMSE of 0.32%; b) $a_{CDM}(\lambda)$ with a NRMSE of 0.70%; and $a_{phy}(\lambda)$ with a NRMSE of 0.77%.

Figure A.4 shows the estimated and measured $a(\lambda)$, $a_{CDM}(\lambda)$ and $a_{phy}(\lambda)$ spectra for point 4.
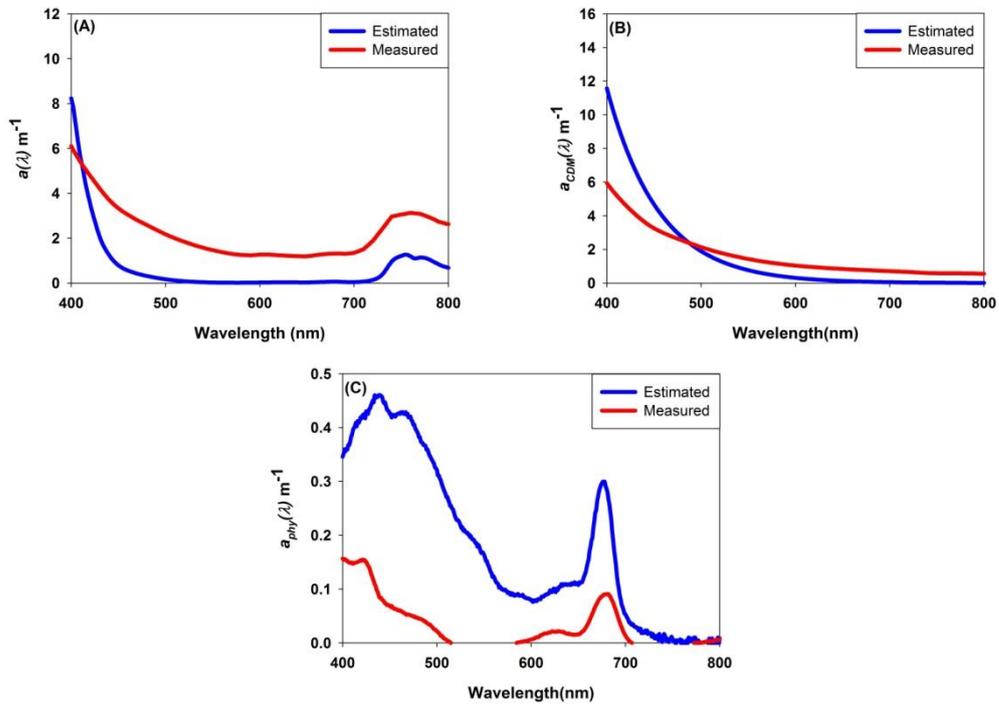

Figure A.4 - Estimated and measured absorption spectra; a) $a(\lambda)$ with a NRMSE of 0.30%; b) $a_{CDM}(\lambda)$ with a NRMSE of 0.26%; and $a_{phy}(\lambda)$ with a NRMSE of 1.11%.

Figure A.5 shows the estimated and measured $a(\lambda)$, $a_{CDM}(\lambda)$ and $a_{phy}(\lambda)$ spectra for point 6.
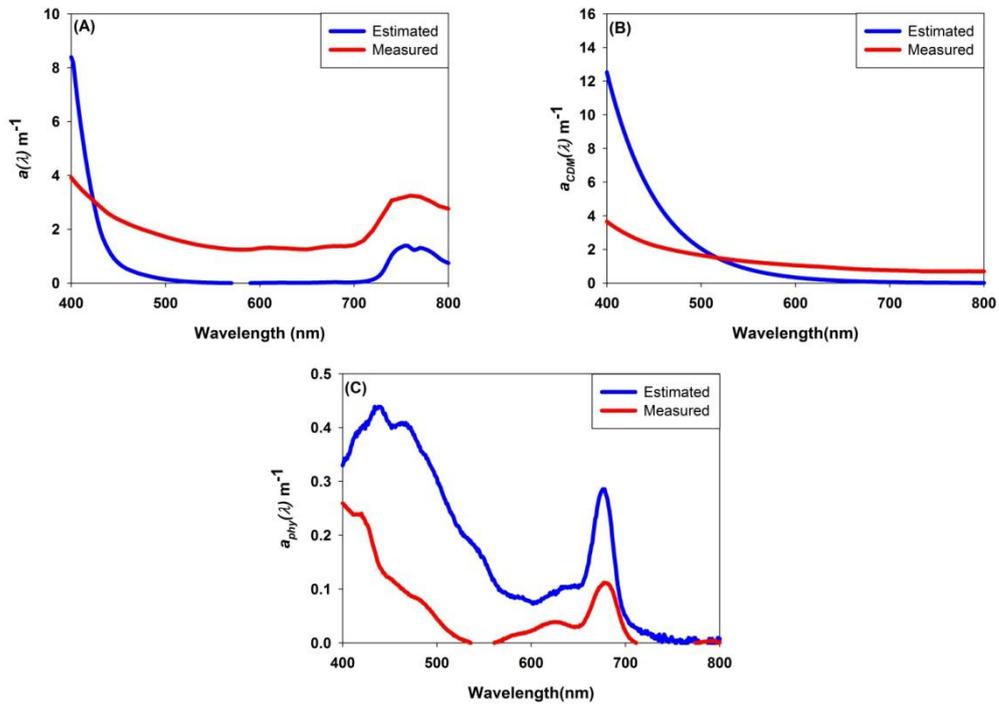
Figure A.5 - Estimated and measured absorption spectra; a) $a(\lambda)$ with a NRMSE of 0.55%; b) $a_{CDM}(\lambda)$ with a NRMSE of 0.77%; and $a_{phy}(\lambda)$ with a NRMSE of 0.58%.

Figure A.6 shows the estimated and measured $a(\lambda)$, $a_{CDM}(\lambda)$ and $a_{phy}(\lambda)$ spectra for point 7.
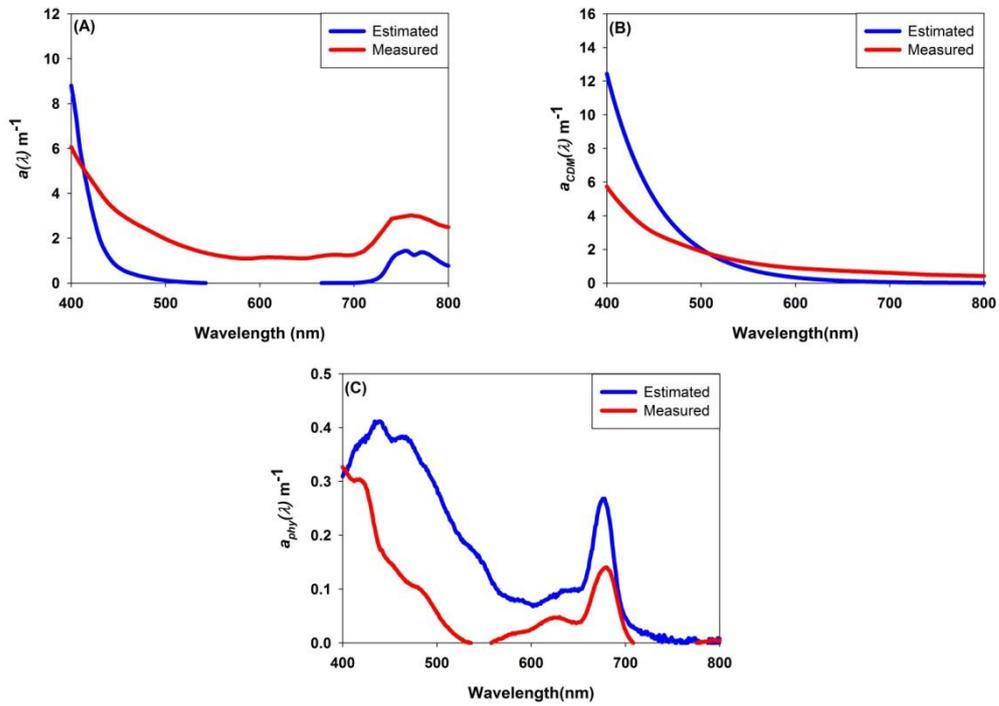

Figure A.6 - Estimated and measured absorption spectra; a) $a(\lambda)$ with a NRMSE of 0.28%; b) $a_{CDM}(\lambda)$ with a NRMSE of 0.32%; and $a_{phy}(\lambda)$ with a NRMSE of 0.36%.

Figure A.7 shows the estimated and measured $a(\lambda)$, $a_{CDM}(\lambda)$ and $a_{phy}(\lambda)$ spectra for point 9.
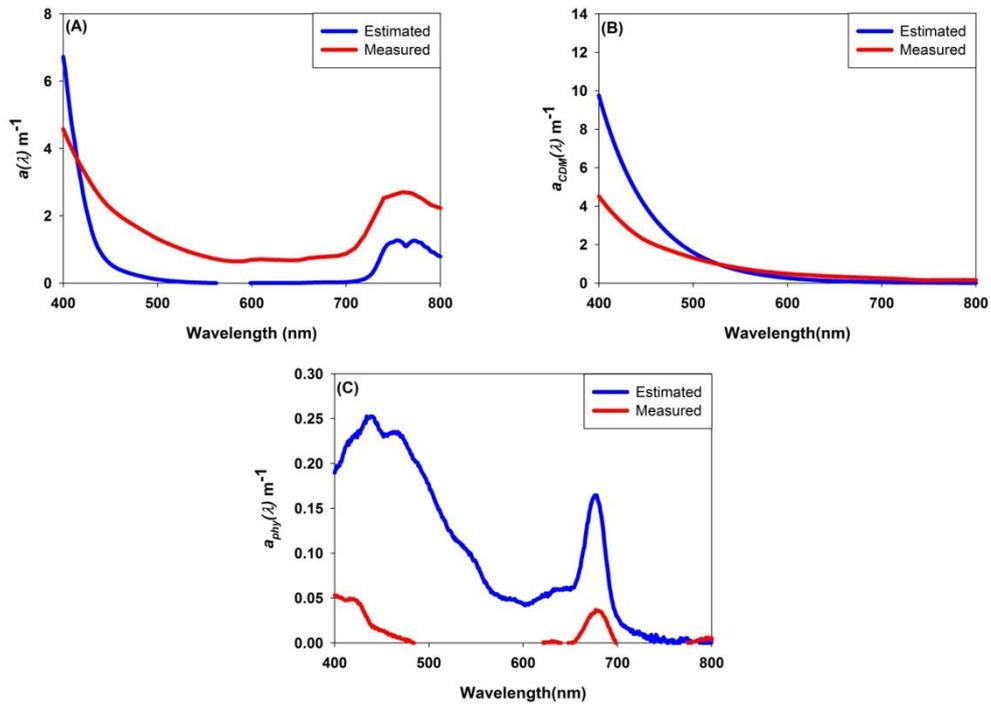
Figure A.7 - Estimated and measured absorption spectra; a) $a(\lambda)$ with a NRMSE of 0.24%; b) $a_{CDM}(\lambda)$ with a NRMSE of 0.30%; and $a_{phy}(\lambda)$ with a NRMSE of 1.43%.

Figure A.8 shows the estimated and measured $a(\lambda)$, $a_{CDM}(\lambda)$ and $a_{phy}(\lambda)$ spectra for point 12.
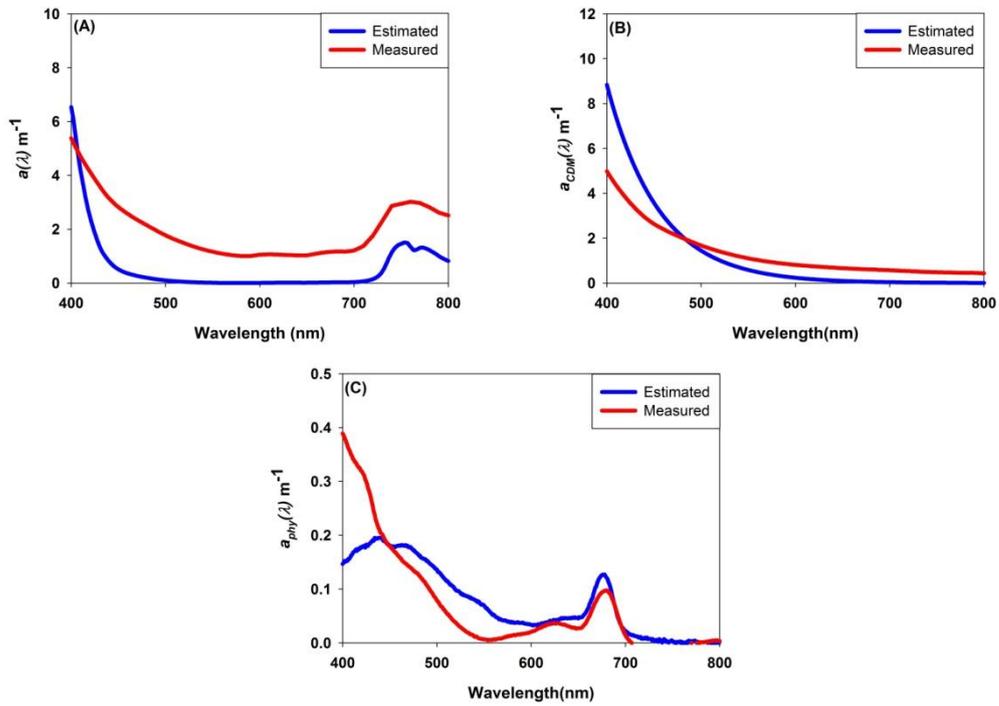

Figure A.8 - Estimated and measured absorption spectra; a) $a(\lambda)$ with a NRMSE of 0.29%; b) $a_{CDM}(\lambda)$ with a NRMSE of 0.22%; and $a_{phy}(\lambda)$ with a NRMSE of 0.16%.

Figure A.9 shows the estimated and measured $a(\lambda)$, $a_{CDM}(\lambda)$ and $a_{phy}(\lambda)$ spectra for point 13.
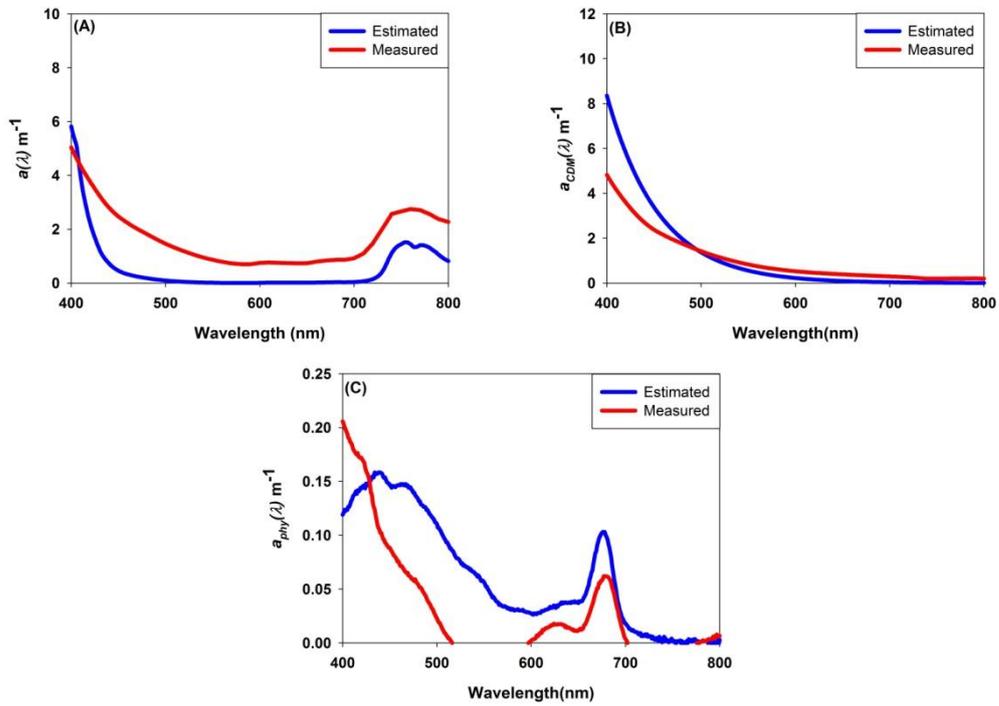

Figure A.9 - Estimated and measured absorption spectra; a) $a(\lambda)$ with a NRMSE of 0.23%; b) $a_{CDM}(\lambda)$ with a NRMSE of 0.19%; and $a_{phy}(\lambda)$ with a NRMSE of 0.20%.

Figure A.10 shows the estimated and measured $a(\lambda)$, $a_{CDM}(\lambda)$ and $a_{phy}(\lambda)$ spectra for point 17.
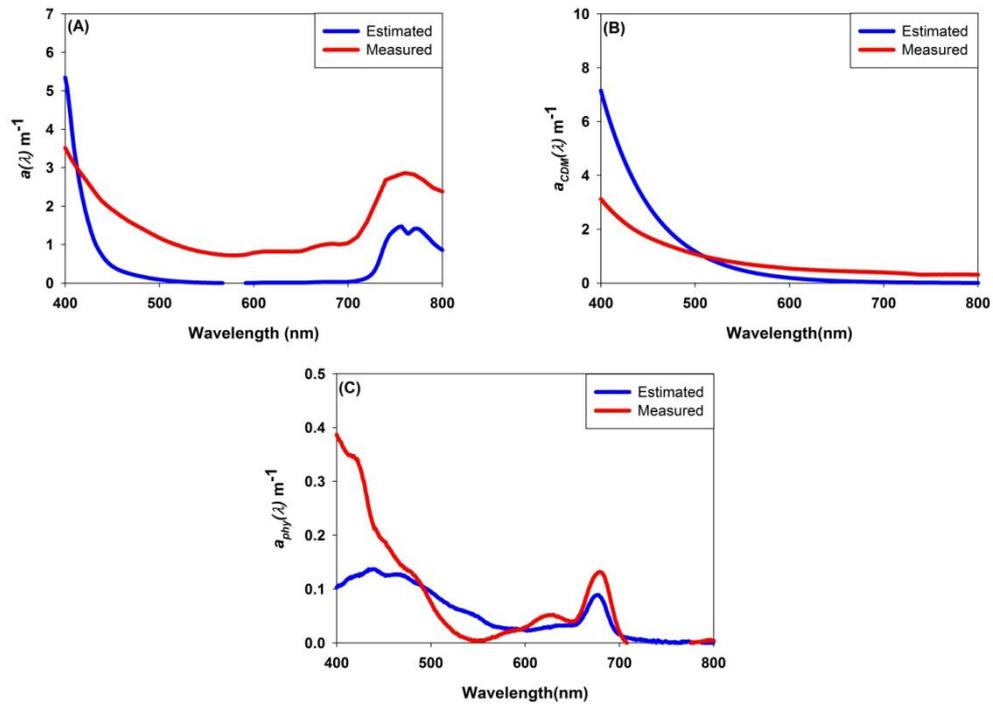

Figure A.10 - Estimated and measured absorption spectra; a) a(λ) with a NRMSE of 0.35%; b) $a_{CDM}(\lambda)$ with a NRMSE of 0.36%; and $a_{phy}(\lambda)$ with a NRMSE of 0.20%.

Figure A.11 shows the estimated and measured $a(\lambda)$, $a_{CDM}(\lambda)$ and $a_{phy}(\lambda)$ spectra for point 18.
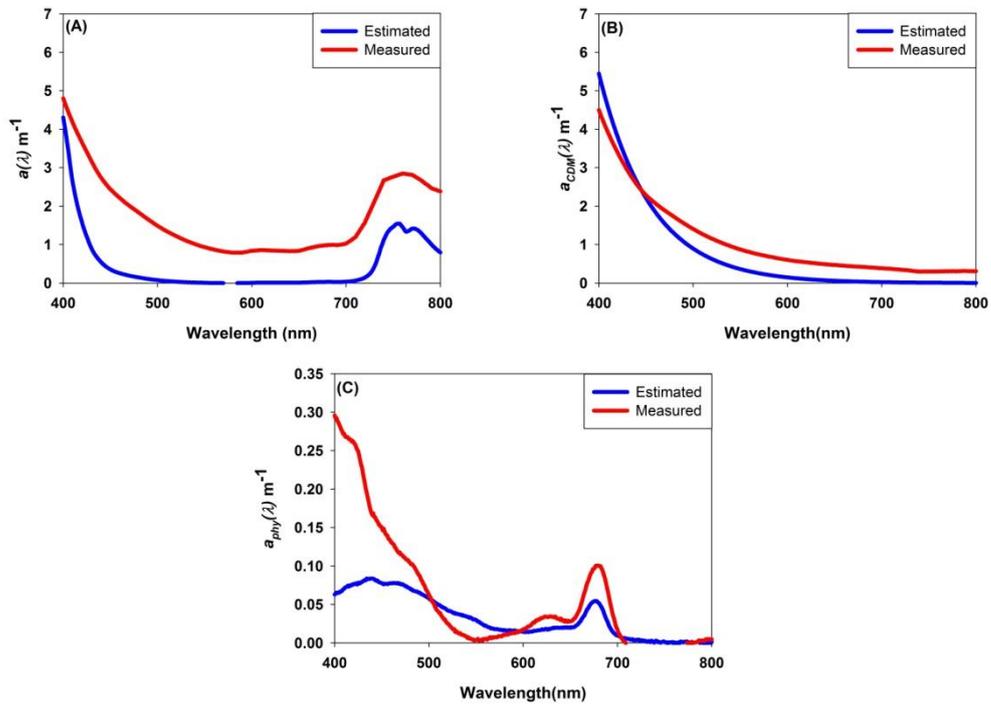

Figure A.11 - Estimated and measured absorption spectra; a) a(λ) with a NRMSE of 0.27%; b) $a_{CDM}(\lambda)$ with a NRMSE of 0.09%; and $a_{phy}(\lambda)$ with a NRMSE of 0.22%.

ANNEX A

Technical characteristics of the Sentinel-3 OLCI instrument

Swath	1440 km
SSI at SSP (km)	300 m
Calibration	MERIS type calibration arrangement with spectral calibration using a doped Erbium diffuser plate, PTFE diffuser plate and dark current plate viewed ~ every 2 weeks at the South Pole ecliptic. Spare diffuser plate viewed ~ periodically for calibration degradation monitoring.
Detectors	ENVISAT MERIS heritage back illuminated CCD55-20 frame-transfer imaging device (780 columns by 576 row array of 22.5 μm square active elements).
Optical scanning design	Push-broom sensor. 5 cameras recurrent from MERIS dedicated Scrambling Widow Assembly supporting 5 Video Acquisition Modules (VAM) for analogue to digital conversion.
Spectral resolution	1.25 nm (MERIS heritage), 21 bands.
Radiometric accuracy	< 2% with reference to the sun for the 400–900 nm waveband and < 5% with reference to the sun for wavebands > 900 nm 0.1% stability for radiometric accuracy over each orbit and 0.5% relative accuracy for the calibration diffuser BRDF.
Radiometric resolution	$< 0.03 \ \text{W m}^{-2} \text{sr}^{-1} \text{mm}^{-1}$
Mass	150 kg
Size	1.3 m^3
Design lifetime	7.5 years

Source: Donlon et al. 2012.